

https://dspace.org/

Quantum structured light in high dimensions

Nape, Isaac; Sephton, Bereneice; Ornelas, Pedro; Moodley, Chane; Forbes, Andrew

2023-05
American Institute of Physics
https://hdl.handle.net/10539/49461
Nape, I., et al. (2023). "Quantum structured light in high dimensions." APL Photonics, 8(5), 051101. DOI: 10.1063/5.0138224.

Downloaded from a DSpace repository. https://dspace.org/

APL Photonics

TUTORIAL | MAY 05 2023

Quantum structured light in high dimensions

Isaac Nape ; Bereneice Sephton ; Pedro Ornelas ; Chane Moodley ; Andrew Forbes

Check for updates

APL Photonics 8, 051101 (2023)
https://doi.org/10.1063/5.0138224

View Online
Export Citation

Articles You May Be Interested In

Quantum-classical path integral. II. Numerical methodology

J. Chem. Phys. (December 2012)

On the efficiency and accuracy of quantum and classical methods of calculating diatomic spectra

J. Chem. Phys. (June 1984)

Complex time dependent wave packet technique for thermal equilibrium systems: Electronic spectra

J. Chem. Phys. (November 1983)

11 June 2026 13:34:37

AIP Advances
Why Publish With Us?
21DAYS average time to 1st decision
OVER 4 MILLION views in the last year
INCLUSIVE scope
Learn More
AIP Publishing

AIP Publishing

Quantum structured light in high dimensions

Cite as: APL Photon. 8, 051101 (2023); doi: 10.1063/5.0138224
Submitted: 9 December 2022 • Accepted: 20 April 2023 •
Published Online: 5 May 2023

View Online Export Citation CrossMark

Isaac Nape,[a] Bereneice Sephton, Pedro Ornelas, Chane Moodley, and Andrew Forbes

AFFILIATIONS

School of Physics, University of the Witwatersrand, Private Bag 3, Wits 2050, South Africa

[a]Author to whom correspondence should be addressed: isaac.nape@wits.ac.za

ABSTRACT

Structured light has become topical of late, where controlling light in all its degrees of freedom has offered novel states of light long predicted, enhanced functionality in applications, and a modern toolbox for probing fundamental science. Structuring light as single photons and entangled states allows the spatial modes of light to be used to encode a large alphabet, accessing high dimensional Hilbert spaces for fundamental tests of quantum mechanics and improved quantum information processing tasks. In this tutorial, we outline the basic concepts of high dimensional quantum states expressed in a basis of spatial modes (structured light) and explain how to create, control, and detect such quantum states in the laboratory with a focus on transverse spatial modes such as the orbital angular momentum and pixel (position) modes. Finally, we highlight some example applications of such quantum structured light, from communications to imaging.

© 2023 Author(s). All article content, except where otherwise noted, is licensed under a Creative Commons Attribution (CC BY) license (http://creativecommons.org/licenses/by/4.0/). https://doi.org/10.1063/5.0138224

11 June 2026 13:34:37

I. INTRODUCTION

It has become topical of late to tailor light in all its degrees of freedom, looking beyond the intensity profile alone for so-called structured light.[1] Traditionally this has been performed with classical light, for example, amplitude, phase, and polarization control in space[2] and wavelength/frequency manipulation for temporal control.[3] Blending space and time together has given rise to exotic forms of spatiotemporal light, long been predicted but only recently observed,[4–6] fueling a movement toward high-dimensional forms of structured light.[7] Creation and detection tools are numerous,[8] including directly from lasers, for compact sources of structured light.[9] These tailored optical fields with complex structures have found a myriad of applications, which have been extensively reviewed to date.[10,11] Perhaps the most topical example is that of optical orbital angular momentum (OAM). The fact that light could carry OAM has been known since at least the days of atomic physics (accounting for the rare quadrupole transitions in atomic states), but it was only 30 years ago (in 1992) that OAM was directly connected to the spatial structure of light through an azimuthal phase of the form $\exp(i\ell\phi)$, winding the phase ℓ times around the azimuth (ϕ) for $\ell\hbar$ of OAM per photon.[12] The explosion of activity since has been captured in recent commemorative perspectives and reviews.[11,13]

The control of structured quantum states of light is far less developed, having appeared in the spatial domain with OAM just 20 years ago.[14] In this seminal work by Nobel Laureate Anton Zeilinger, the conservation of OAM was confirmed down to the single photon level and demonstrated as qubit entangled states in several OAM subspaces, the first demonstration of spatial mode entanglement. As there are an infinite number of spatial modes on any given basis, this form of quantum structured light has the potential to realize d dimensional states[15–17] for a large encoding alphabet that scales as $\log_2 d$ bits/photon and enhanced security with cloning fidelity that scales as $F = \frac{1}{2} + \frac{1}{(1+d)}$, making this approach attractive for quantum information processing. Although d can be increased by degrees of freedom such as path and time, here we will consider only spatially structured quantum light. One good reason for the interest in this avenue is that the classical properties of spatial modes often translate to benefits in the quantum realm, for instance, self-healing of Bessel structured quantum states[18] and enhanced control by mixing polarization and spatial modes for hybrid entanglement,[19–21] analogous to vectorial structured light.

For a long time, spatial mode entanglement remained at the qubit ($d = 2$) level, mimicking polarization states, although with multiple options for the two-dimensional subspaces through many combinations of orthogonal spatial modes. Indeed, this analogy allowed the easy transition of the quantum toolkit from polarization qubits to structured light qubits, for instance, quantum state tomography (QST)[22,23] and bell violation tests,[24] enabled by computer generated holograms. It is only in the last decade that the true high-dimensional nature of structured quantum light has come

© Author(s) 2023

to the fore, both as entangled states and as heralded single photons. Seminal contributions have demonstrated high-dimensional Bell tests,[25] high-dimensional QSTs,[26] fast and accurate entanglement tests[27] and witnesses,[28] high-dimensional quantum interference,[29] and sophisticated high-dimensional quantum state creation tools.[30–34] The application of structured quantum light in high-dimensional quantum information processing has seen quantum key distribution up to $d = 7$ in free space[35,36] and $d = 6$ in optical fibers,[37,38] quantum secret sharing up to $d = 11$ with Bessel photons,[39] entanglement swapping up to $d = 2$ with OAM,[40] and teleportation up to $d = 3$ with linear optics[41,42] and $d = 15$ with non-linear optics.[43]

In this tutorial, we start by briefly covering the formalism used in working with high-dimensional structured quantum light, concentrating on practical tools using OAM and pixel (position) modes as examples. We then outline some of the basics needed in order to get started, extending from the creation step in bulk crystals to aligning, manipulating, detecting, and characterizing the output state, along with some caveats needed for these considerations. Finally, we look at some example applications ranging from imaging to secure communications, where the advantages and challenges that come with harnessing high-dimensional states are outlined.

II. THEORETICAL CONCEPT

A. Structured light and its degrees of freedom

In this section, we introduce the reader to the concepts of internal degrees of freedom of photons and thereafter discuss ways to obtain high dimensional encoding in quantum structured light.

A single photon that is freely propagating through a vacuum is an excitation of the electromagnetic field that travels at a constant speed (c). A modern version of Thomas Young's experiments can readily show that such a photon has a wave-like nature and has a probability amplitude, or equivalently, its wavefunction, that is distributed through space and time. An illustration of our photon is shown in Fig. 1(a), where the photon is decomposed into its degrees of freedom, namely the (i) polarization, which is associated with the spin angular momentum of photons, the (ii) temporal envelope, and the (iii) spatial structure, which includes the transverse (x and y) and longitudinal components (z). Accordingly, the photon state can be expressed as

$$|\Psi\rangle = \iint \Phi_{spatial}(\mathbf{r})\Omega_{time}(t)|\varsigma_{pol}\rangle|\mathbf{r}\rangle|t\rangle dt\ d^3r, \tag{1}$$

using the continuous spatial $|\mathbf{r} = (x, y, z)\rangle$ and temporal $|t\rangle$ coordinate basis, with corresponding probability amplitudes, $\Phi_{spatial}(\mathbf{r})$ and $\Omega_{time}(t)$, that constitute the photon wavepacket, while $|\varsigma_{pol}\rangle$ denotes the polarization state of the photon. The temporal and frequency (ω) components are related by the Fourier transform, i.e., $\tilde{\Omega}(\omega) \propto \int \Omega(t)\exp(-i\omega t)dt$, therefore determining the spectral properties of the photon. Structured light refers to the tailoring of all these degrees of freedom.[1] Here, we aim to show how it can be harnessed for higher dimensional encoding using the internal degrees of freedom of photons.

The polarization degree of freedom was initially the best candidate for photon information processing due to its ease of control with conventional linear optical elements and was used to demonstrate numerous fundamental tests of quantum mechanics (Bell inequality violations[44] and quantum erasers[45]) and the initial demonstrations of quantum communication and cryptography (quantum key distribution,[46] teleportation,[47] and superdense coding[48]). However, the polarization states of a single photon are restricted to a two level system that can be composed of the canonical right $(|0\rangle \equiv |R\rangle)$ and left $(|1\rangle \equiv |L\rangle)$ circular polarization eigenstates as basis modes. Here, the states $|0(1)\rangle$ represent the logical (standard) basis.

The two level system can be visualized using the Bloch sphere, as shown in Fig. 1(b), where any two modes on the opposite ends of the sphere can be used to form a logical basis. For example, if we look at the equator of the sphere, the superposition states $|R\rangle \pm |L\rangle$, corresponding to the horizontal $|0\rangle \equiv |H\rangle$ and vertical $|1\rangle \equiv |V\rangle$ linear polarization states, form another logical basis for expressing polarization states, respectively. The same is true for the rectilinear basis states, $|R\rangle \pm i|L\rangle$, corresponding to the diagonal $|0\rangle \equiv |D\rangle$ and anti-diagonal $|1\rangle \equiv |A\rangle$ linear polarization states, respectively. Therefore, for polarization states, the encoding basis, $\mathcal{B}_d$, can only contain two orthogonal states, $|0\rangle$ and $|1\rangle$, at a time. For higher dimensional encoding, we require that the encoding basis $\mathcal{B}_d$ has $d > 2$ states, i.e., having the elements $|0\rangle, |1\rangle, \ldots, |d-1\rangle$.

In the section that follows, we explore how the remaining degrees of freedom (time and space) can be used to obtain higher dimensional states. In particular, we will focus on the spatial-momentum basis, although some of the techniques can be transferred to the temporal basis.

B. High dimensional ($d > 2$) structured photons

Our remaining degrees of freedom, the temporal, spectral, and spatial components, are continuous. For example, the spatial components span $\mathbb{R}^3$, which includes the transverse coordinates (x, y) and the longitudinal component z. Similarly, the conjugate basis for the spatial components, which corresponds to the momentum basis, can also be separated into its continuous transverse and longitudinal parts. Because we would like to obtain a discrete basis, it is pertinent to ask, how can we obtain discrete higher dimensional photon states given the continuous nature of the spatial basis?

First, we establish the following: our discrete basis states must contain $d > 2$ distinct states, i.e., being the set $\mathcal{B}_d = \{|j\rangle, i = 0, 1, \ldots, d-1\}$ and $\langle i|j\rangle = \delta_{ij}$, for all $|i\rangle, |j\rangle \in \mathcal{B}_d$ and must be complete, i.e., have a completeness relation $\sum_{j=0}^{d-1} |j\rangle\langle j| = \mathbb{I}_d$. Given such a basis, any high dimensional state can be written as the superposition,

$$|\psi\rangle = \sum_{j=0}^{d-1} a_j|j\rangle, \tag{2}$$

where a_j are complex coefficients that determine the state $|\psi\rangle$ up to a global phase. The normalization condition requires that the coefficients satisfy $\sum_j |a_j|^2 = 1$.

To satisfy the above, we can first attempt to partition our degrees of freedom in the continuous space into discrete and bounded intervals, $\mathbf{r} = (x, y) \rightarrow \mathbf{r}_k = (x_k, y_k)$, i.e., slicing the photon fields into N partitions or unit cells that can be addressed individually as *pixels*,[49] as illustrated in Fig. 1(c). The same can be performed in the temporal-spectral degrees of freedom,[50,51] where

11 June 2026 13:34:37

© Author(s) 2023

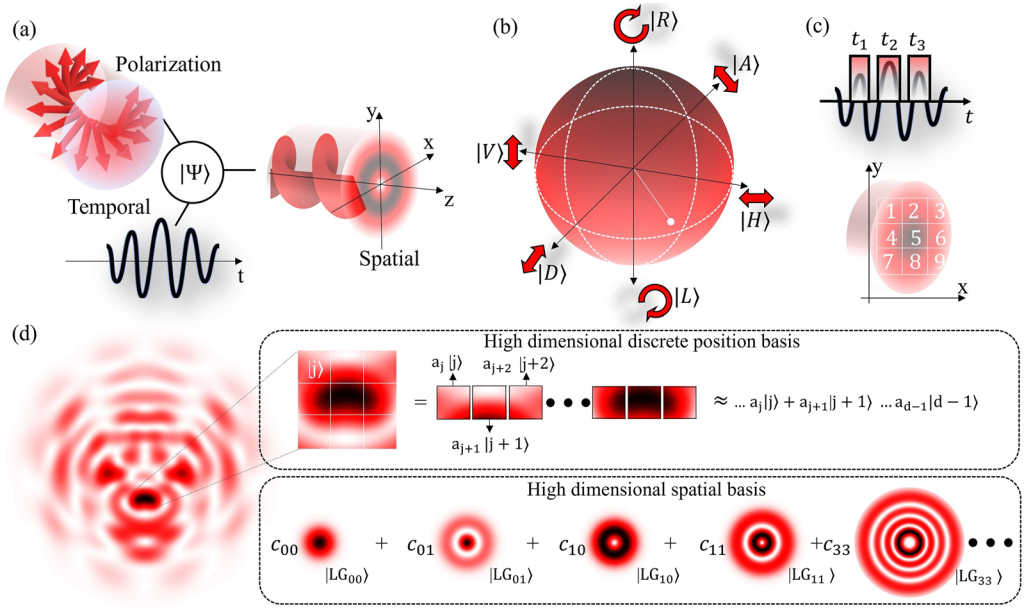


FIG. 1. High dimensional structured photons. (a) A photon field can be ascribed to a state that characterizes its polarization and spatial and temporal degrees of freedom. (b) By selecting one of the degrees of freedom, say polarization, a qubit space can be formed consisting of a two dimensional ($d = 2$) basis formed by the right $|R\rangle$ and left $|L\rangle$ circular polarization states. The two-dimensional space can be visualized geometrically using the Bloch sphere (equivalent to the Poincaré sphere for polarization). (c) The temporal and transverse spatial degree of freedom are higher dimensional since more than two states are required to describe each of them. This can be seen by partitioning each degree of freedom into discrete, non-overlapping cells, where each cell contains information about the state of the photon. These states are commonly referred to as the time-bin and pixel basis states for the temporal and spatial components, respectively. (d) Besides the decomposition of an arbitrary spatial profile using the discrete pixel basis modes (top panel), one can also use spatial structured modes, where the arbitrary field can now be expressed using a complete set of spatially structured patterns (bottom panel). These modes also constitute the modal basis for quantum structured light.

information is encoded into time bins. In the spatial domain, each discrete state is a "pixel" mode that is formed by a collection of points, $\mathbf{r}$, in the transverse plane that are contained in the area A_k. While they were initially used in the form of squares in early experiments, today they include various geometries and arrangements.[52] In Fig. 1(d), we illustrate an arbitrary segment of the photon field as a combination of pixel modes, each containing information about the field in $\mathbb{R}^2$. Each pixel is independent of its neighboring pixels. This can be seen as mapping the transverse spatial profile of our photon in Eq. (1), with the probability amplitude $\Phi(\mathbf{r})$ as

$$|\Phi\rangle = \int_{\mathbf{R}^2} \Phi(\mathbf{r})|\mathbf{r}\rangle d^2r \to \sum_{k=0}^{N-1} a_k|r_k\rangle, \tag{3}$$

where the discrete and continuous versions are equivalent when $N \to \infty$, meaning that the transverse plane is partitioned into an infinite number of pixels, which are now points in space. Furthermore, the coefficients, a_k, can be evaluated from the points, $\mathbf{r} \in \mathbf{A}_k$, for the kth partition according to $a_k = \int_{\mathbf{A}_k} \Phi(\mathbf{r})\ d^2r$.

While this approach works well, the pixel dimensionality can be limited by the performance of the optical system and must thus be chosen appropriately.[52] The choice of pixel sizes can, for example, affect the quality of quantum imaging experiments if not chosen in conjunction with the performance of the optical setup (angular resolution, point spread function), as well as taking into account the joint probability amplitude (correlation length) of the correlated photons.[52,53] Put simply, more pixel states do not imply higher resolution; the performance is highly dependent on the quality of the photon sources and optical elements. Furthermore, for encoding purposes, pixel modes are not stable on propagation due to diffraction and can present challenges in applications that require long propagation distances, especially if the pixels are encoded with arbitrary amplitudes and phases and the resulting fields are not modes of free space.

This brings us to the second approach, which makes use of spatial patterns of light, as illustrated in the bottom panel of Fig. 1(d), where our photon field is expressed using arbitrary propagation invariant modes. In particular, we consider spatial modes with a slowly varying transverse extent relative to the longitudinal component. Such modes are known to preserve their transverse spatial profiles upon propagation, unlike pixel states. These are called paraxial optical fields. A topical example is the family of photon fields that carry OAM and are characterized by the azimuthal phase dependent factor $\exp(i\ell\phi)$, where each photon has an OAM of $\ell\hbar$ per photon, with ℓ being the integer that is known as the topological charge.[12] Here ϕ is the azimuth coordinate. Optical modes with this characteristic are eigenstates of the OAM operator $\hat{L}_z = -i\hbar\frac{\partial}{\partial\phi}$. In cylindrical coordinates $\mathbf{r} = (r, \phi, z)$, these modes take the form

11 June 2026 13:34:37

© Author(s) 2023

$$\Phi(\mathbf{r}) = R(\mathbf{r}) \exp(i\ell\phi), \tag{4}$$

where $R(\mathbf{r})$ is an enveloping function that determines the radial amplitude profile of the photon. Bessel–Gaussian[54] and Ince–Gaussian[55] are examples of mode families that can possess the characteristic azimuthal profile of OAM modes and have been utilized in quantum experiments. Other mode families that are also propagation invariant at the single photon level include the Hermite–Gaussian modes,[56] which have Cartesian symmetry, and the Airy modes,[57] which show self-healing and free acceleration.

For this tutorial, we will focus on the OAM carrying Laguerre-Gaussian (LG) mode family because of its ubiquity in high dimensional quantum optics.[15,16] There is good reason for this: their detection can be performed in a phase-only fashion (good for efficiency), the size and radius of curvature of the detected mode do not affect the total OAM (so the detection is less sensitive to axial alignment), and the OAM modes form a natural Schmidt basis, which is highly convenient when expressing entangled states. On the negative side is the fact that any lateral displacement will alter the OAM detected (if $\mathbf{r}$ changes, then so does $\mathbf{r} \times \mathbf{p}$). High OAM implies high spatial frequencies, which may not be collected by the optical system, and OAM does not, in fact, form a complete orthonormal basis without the radial information (the p index in the case of the LG modes), so one finds "missing entanglement" without it.[58] A photon defined in the LG basis maps onto the state,

$$|\mathrm{LG}_{\ell p}\rangle = \int_{\mathbf{R}_2} \mathrm{LG}_{\ell p}(\mathbf{r})|\mathbf{r}\rangle d^2 r, \tag{5}$$

where ℓ is the topological charge, p is the radial mode order, and $\mathrm{LG}_{\ell p}(\mathbf{r})$ is the field profile (equivalently the wave-function) of the photon at any given location $\mathbf{r}$.

In cylindrical coordinates and for $z = 0$, the LG mode family has the form

$$\mathrm{LG}_{\ell p}(\mathbf{r}) = \frac{C_{\ell p}}{w} \exp\left(-\frac{r^2}{w^2}\right)\left[\sqrt{2}\frac{r}{w}\right]^{|\ell|} L_p^{\ell}\left(\frac{2r^2}{w^2}\right) \exp(i\ell\phi), \tag{6}$$

where the function $L_p^{\ell}(\cdot)$ is the associated Laguerre polynomial, and w is the second moment radius of the Gaussian envelope. The constant factor $C_{\ell p}$ is a normalization constant, such that $\int_{\mathbf{R}_2} |\mathrm{LG}_{\ell p}(\mathbf{r})|^2 d^2 r = 1$. In Fig. 2(a), various LG intensities are shown. The intensity profile has a region of null intensity centered at the origin and a radius that increases with the topological charge, $|\ell|$. We also see that the modes have concentric rings that are controlled by the radial index p.

Furthermore, OAM modes ($\mathrm{LG}_{\ell,p=0}$) have been shown to have an analogous representation on the Bloch sphere, similar to polarization states in Fig. 1(b).[59] We illustrate our OAM Bloch sphere in Fig. 2(b), where the poles of the sphere contain the $|\pm\ell\rangle = |\mathrm{LG}_{\pm\ell,p=0}\rangle$ modes, and the equally weighted superpositions are contained at the equator. While this is only shown for $\ell = \pm 1$, multiple spheres can be constructed using arbitrary ℓ values. Furthermore, our illustration in Fig. 2(c) shows that the radial modes, in combination with the OAM modes, can be used to construct arbitrary two dimensional spheres. Infinitely many such spheres can be constructed from the LG modes. As with the polarization qubits, given any two OAM modes, numerous experiments have emerged where the OAM qubits are used as a computational basis for processing quantum information with further advances made to harness them for high dimensional encoding schemes for single photons,[36] entangled two photon states,[60] and three photon states[33] showing their significance in quantum science.

Significantly, numerous applications of high dimensional quantum structured light make use of the LG basis in its high dimensional form, where states of the form

$$|\psi\rangle = \sum_{\ell p} c_{\ell p} |\mathrm{LG}_{\ell p}\rangle, \tag{7}$$

having the coefficients $c_{\ell,p}$, can be tailored for a given application. For example, in quantum key distribution, such superpositions can be optimized to achieve unparalleled security,[35,36,39,61] transmit quantum states through fiber,[38] or tailor novel projective measurements for state characterization.[25–27,62]

Next, we explore two photon states and introduce the concept of entanglement.

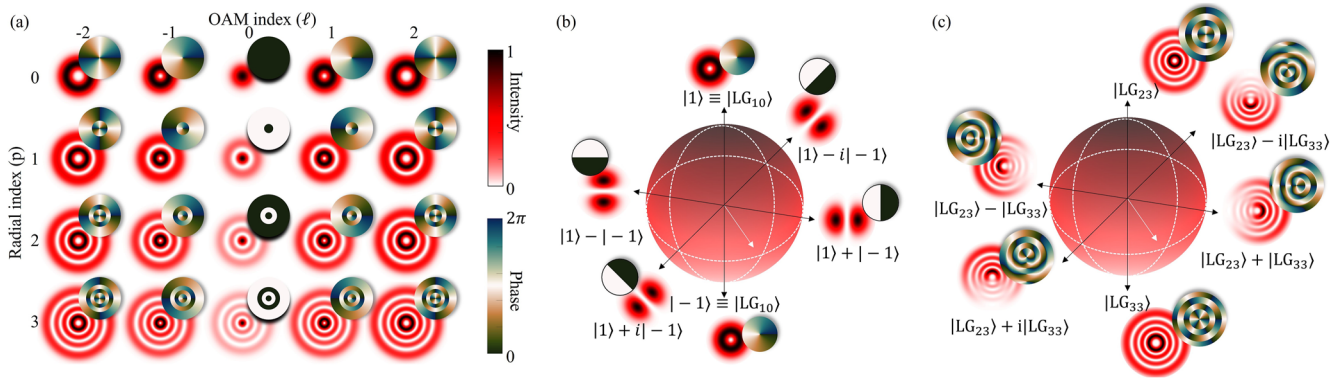


FIG. 2. Laguerre–Gaussian basis modes. Intensity profiles for the spatial distributions described by $\mathrm{LG}_{\ell,p}$ modes with indices $\ell = [-2, 2]$ and $p = [0, 3]$ with the phase profiles given as insets in the top-right corner of each mode. An example of the two dimensional state space that can be created using the LG mode basis for (b) $\ell = \pm 1$ and $p = 0$ (c) $\ell = 2, 3$ and $p = 3$.

11 June 2026 13:34:37

© Author(s) 2023

C. Entangled structured light

So far, our modes of structured light have been discussed in the context of single photons. A quantum system may entail more than a single photon, and in some instances, the state of one single photon may depend on that of another (entanglement). In order to elucidate this, we describe how to write the state of more than one photon and what it means in cases where there is entanglement present.

Consider two photons that are spatially separated. Here, the two particle state requires the use of tensor product states, where the basis states occupy a combined Hilbert space ($\mathcal{H}_{AB}$). For instance, we can consider a system comprised of two OAM qubits. The basis on which we can describe the photons is readily formed from the tensor product of the individual bases. We can chose the basis, $\mathcal{M} = \{|\ell_1\rangle, |\ell_2\rangle\}$. Therefore, the two photon basis now becomes $\mathcal{M}_{AB} = \mathcal{M}_A \otimes \mathcal{M}_B = \{|\ell_1\rangle|\ell_1\rangle, |\ell_1\rangle|\ell_2\rangle, |\ell_2\rangle|\ell_1\rangle, |\ell_2\rangle|\ell_2\rangle\}$. If each individual particle were in a separate arbitrary superposition, where the coefficients are non-zero, the state of the composite system is

$$\begin{aligned}|\psi\rangle_{AB} &= |\psi\rangle_A \otimes |\psi\rangle_B \\ &= (a_1|\ell_1\rangle_A + a_2|\ell_2\rangle_A) \otimes (b_1|\ell_1\rangle_B + b_2|\ell_2\rangle_B) \\ &= a_1b_1|\ell_1\rangle_A|\ell_1\rangle_B + a_1b_2|\ell_1\rangle_A|\ell_2\rangle_B \\ &\quad + a_2b_1|\ell_2\rangle_A|\ell_1\rangle_B + a_2b_2|\ell_2\rangle_A|\ell_2\rangle_B, \end{aligned} \tag{8}$$

resulting in a superposition of two photon states that can be expanded in the composite basis $\mathcal{M}_{AB}$.

As shown in Eq. (8), the composite state can be factorized and thus written as a product or tensor state of the individual particles. Interesting properties arise when this is no longer true. For example, we can consider the state

$$|\psi\rangle_{AB} = \frac{1}{\sqrt{2}}(|\ell_1\rangle_A|\ell_2\rangle_B + |\ell_2\rangle_A|\ell_1\rangle_B). \tag{9}$$

Here, it is clearly not possible to factor the state of either particle, and so it is said to be *non-separable*.

The implications of this are that one can no longer describe either photon individually (in each basis alone) but rather requires both at the same time. Accordingly, if $|\ell_1\rangle$ was measured on photon A, photon B would then be in the state $|\ell_2\rangle$, and if $|\ell_2\rangle$ was measured on photon A, photon B would then be in the state $|\ell_1\rangle$. This is always true despite any arbitrary distance of separation. This prompted Einstein to question the reality,[63] calling this "spooky action at a distance," which has since been termed *quantum entanglement*.[64] Consequently, this property is a direct consequence of the inability to factorize the state into its subsystems. As such, composite states for which one is not able to write as a product state, i.e., $|\psi\rangle_{AB} \neq |\psi\rangle_A \otimes |\psi\rangle_B$, can be called entangled.

To generalize the description of entangled photons beyond $d = 2$, we need to add more linearly independent terms to Eq. (9) such that the state remains non-separable. Such states can be readily generated from spontaneous parametric down conversion (SPDC) by harnessing energy and momentum conservation in nonlinear crystals where a high energy photon (pump) impinges on the crystal interface, thereafter producing two daughter photons. We will explore SPDC in more detail in later sections, but for now, we use it to guide our discussion about high dimensional entanglement. Because momentum is conserved by the SPDC process, so is OAM. The OAM content of the twin photons adds up to that of the OAM of the pump photon, ℓ_p. As a result, the high-dimensional entangled state can be written as

$$|\Psi_{AB}\rangle = \sum_{\ell=-L}^{L} c_\ell |\ell\rangle_A |\ell_p - \ell\rangle_B, \tag{10}$$

where there are $d = 2L - 1 > 2$ states with non-zero normalized probability amplitudes, c_ℓ, for each state $|\ell\rangle_A|\ell_p - \ell\rangle_B$, and ℓ_p is the OAM of the pump photon. The collection of states, $|\ell\rangle_A|\ell_p - \ell\rangle_B$, is called a Schmidt basis. Because the decomposition in Eq. (10) contains $d > 2$ terms that are linearly independent and non-separable, the state exhibits high dimensional entanglement where the dimensions of the entanglement should be determined by the number of Schmidt basis states that have non-zero coefficients and maintain the non-separability of the state.

While the decomposition we have shown for the SPDC structured photons assumes a pure coherent superposition of Schmidt basis modes, in general, the states can contain some degree of mixture. In that case, we cannot express the states as linear combinations of basis states but rather as weighted sums of matrix operators. For example, it can be shown that the SPDC state, under some conditions, can be expressed as an isotropic Werner-like state,

$$\rho_{AB} = p|\Psi_{AB}\rangle\langle\Psi_{AB}| + \frac{1-p}{d^2}\mathbb{I}_{d^2}, \tag{11}$$

where $\frac{1}{d^2+1} < p \leq 1$ scales the probability of obtaining the pure state $|\Psi\rangle_{AB}$, d^2 is the dimensions of the composite Hilbert space of the two photons, and $\mathbb{I}_{d^2}$ is the d^2 dimensional identity operator defined over the two photon subspace. We obtain a pure state for $p = 1$ so that $\rho_{AB} = |\Psi_{AB}\rangle\langle\Psi_{AB}|$, while we have a completely mixed state for $p = 0$ so that $\rho_{AB} = \frac{1}{d^2}\mathbb{I}_{d^2}$. Example density matrices are shown in Figs. 3(a)–3(c) for $p = 1$ in dimensions $d = 2$, 3, and 5. To show the impact of introducing the mixture into the state, we set $p = 0.4$ and show the same density matrices in Figs. 3(d)–3(f). In the case of $p = 0$, the state is a maximally mixed state and cannot be written as a separable outer product of pure states. In this case, we have a statistical mixture (or ensemble) of purestates that have equal probability. This can correspond to an incoherent source that produces classical two photon correlations. Moreover, the state is entangled when $p > \frac{1}{d+1}$.[65] This inequality sets the boundary between separable and entangled states. Here, the boundary decreases with increasing dimensions, demonstrating that entanglement can be preserved if the two photons occupy a sufficiently large Hilbert space in the presence of noise. As such, having many entangled structured patterns is, therefore, crucial to achieve this.

So far, we see that the potential benefits of using high dimensional quantum structured light are coming to the fore. Next, we introduce measures that quantify the dimensions, information capacity, and purity of our quantum states.

11 June 2026 13:34:37

© Author(s) 2023

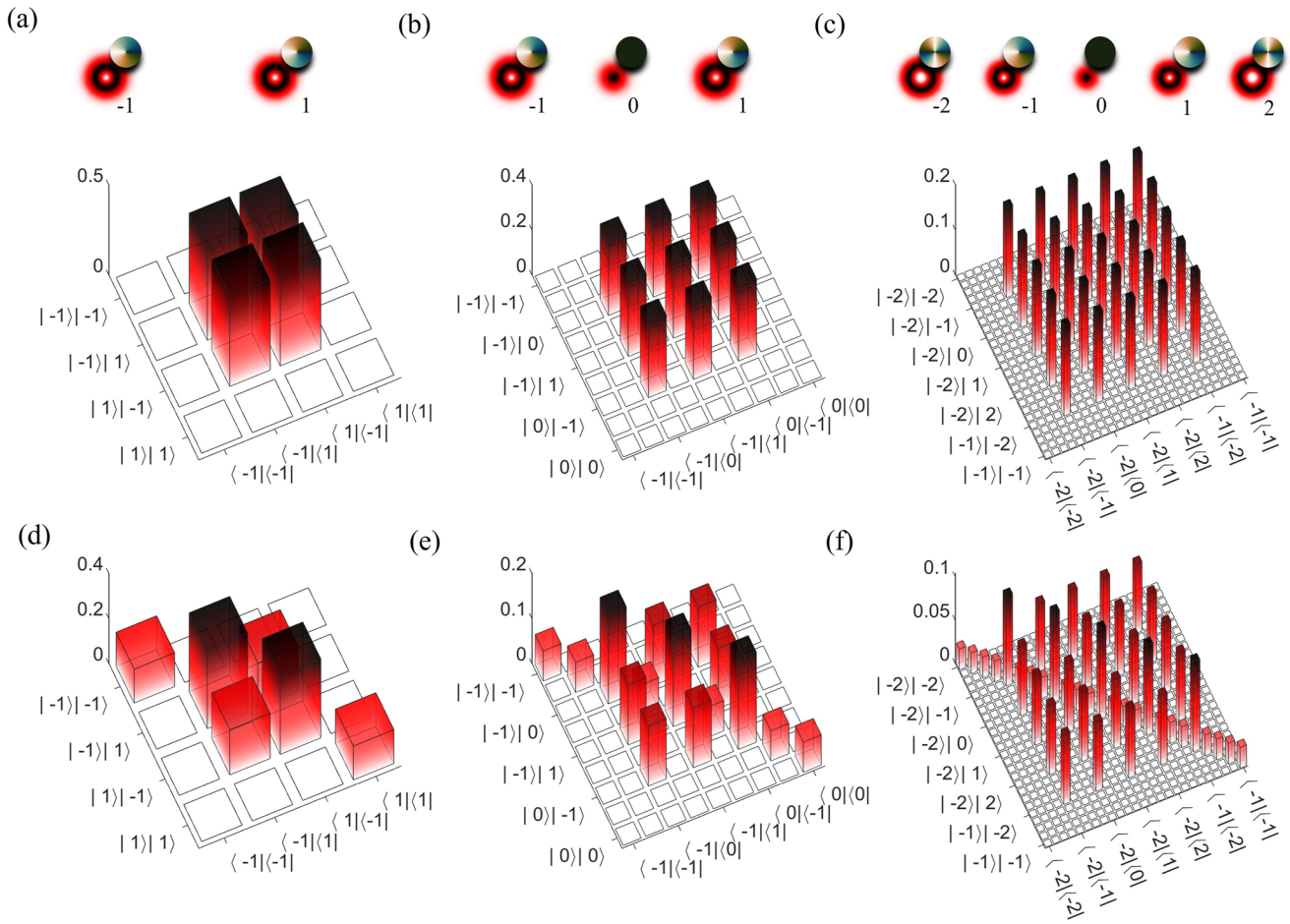


FIG. 3. Density matrices of pure and mixed high dimensional entangled states. Exemplary density matrices of photons entangled in high dimensions for (a) $d = 2$, (b) $d = 3$, and (c) $d = 5$. The orbital angular momentum basis modes for each state are shown above each density matrix. Isotropic mixed states with $p = 0.4$ for the same entangled states in (d) $d = 2$, (e) $d = 3$, and (f) $d = 5$.

III. KEY EQUATIONS FOR HIGH DIMENSIONAL STATES

Here, we outline some of the key equations that are used to qualitatively and quantitatively characterize high dimensional quantum states, ranging from the amount of information that can be packed into quantum states to the quality of the quantum states that are produced.

A. Information capacity

Suppose Alice and Bob wish to share information using a simple prepare and measure protocol by encoding photons with high dimensional structured modes. Each state, on its chosen basis, is associated with a message (symbol). Here, Alice prepares states on this basis, and Bob performs measurements on the same basis. We aim to quantify the amount of information that can be transmitted between the two parties.

The said bases state that Alice and Bob's use can be composed of the sets $\{|k\rangle\}, \{|j\rangle\} \subset \{|i\rangle\}$, respectively, where i indices the spatial modes. How well the photons can be measured and detected may be computed from the average fidelity, where the fidelity of each state is given by

$$f_{kj} = \left(\mathrm{Tr}\left(\sqrt{\sqrt{\rho_A^k}\rho_B^j\sqrt{\rho_A^k}}\right)\right)^2, \tag{12}$$

and $\rho_{A(B)}^{k,j}$ are the density matrices corresponding to Alice and Bob's states, respectively. For pure states, the fidelity can be computed from the inner product between the states that the operators map onto, i.e., from $f_{kj} = \left|\langle\Phi_{Bob}^k|\hat{U}|\Phi_{Alice}^j\rangle\right|^2$, where $\hat{U}$ is the channel operator. We show the scattering probability matrix in Fig. 4(a) for the case where the channel does not change the transmitted states. The matrix resembles an identity matrix indicating that all prepared states can be identified and that the channel does not induce modal coupling (crosstalk) between the chosen basis states. In this case, the average fidelity is 1. Given that these modes can be successfully

11 June 2026 13:34:37

© Author(s) 2023

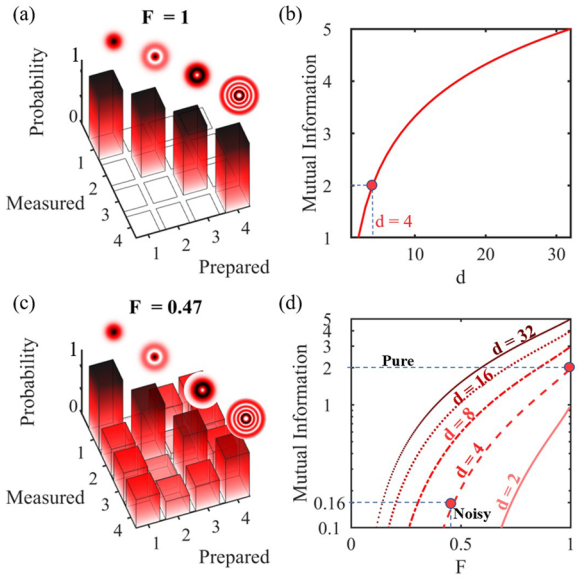


FIG. 4. Information capacity. (a) The scattering probability matrix for a $d = 4$ dimensional basis of spatial modes (shown as insets) above the diagonal. The matrix resembles an identity matrix indicating that all prepared states can be identified. The average fidelity is $F = 1$. (b) The mutual information (capacity) as a function of dimensions (d) in units of bits per photon. (c) Scattering probabilities for a given system that has high crosstalk (noisy). The fidelity for this case is $F = 0.47$. (d) Mutual information vs average fidelity for selected dimensions. Because errors can reduce channel fidelity, the information capacity of the quantum channel will also be affected.

transferred between Alice and Bob, how much information can be transferred through the channel?

Mutual information is a measure that is commonly employed to quantify the amount of information that can be transmitted between Alice and Bob. For a perfect channel, this is given by $I_{AB} = \log_2(d)$. In Fig. 4(b), we show the channel capacity as a function of the d dimensions. Provided that the channel is perfect, we can pack more information into the photons by using more spatial modes. For qubits ($d = 2$), the mutual information is restricted to 1 bit per photon and can be doubled by using $d = 4$ dimensional encoding. As the encoding dimensions are increased, the mutual information also increases.

However, if there are imperfections in the channels, i.e., varying refractive indices, mode dependent dispersion, etc., then there will be errors introduced in the detection signal, therefore reducing the state fidelity. This can introduce errors into the detection signals, as shown in Fig. 4(c), where the channel average fidelity is $F = 0.47$. Consequently, this means that the amount of information per photon (mutual information) will be reduced. Given that the fidelity of the channel is known, the mutual information can be quantified as[66]

$$I_{AB} = \log_2(d) + F\log(F) + (1-F)\log\left(\frac{1-F}{d-1}\right). \tag{13}$$

In Fig. 4(c), we show the mutual information as a function of average fidelity for several dimensions. For the noisy $d = 4$ example, having low fidelity, the mutual information is $I_{AB} = 0.16$ and only obtains high mutual information when $F = 1$. However, the same fidelity yields a larger information capacity for higher dimensions. It is clear that by increasing dimensions, higher information capacities can be maintained under noisy conditions.

B. Dimensionality

Subsection III A highlights an important point: to overcome noise, it makes more sense to use higher dimensional basis states. Moreover, it has been proven that even higher dimensional quantum entangled structured photons can be robust against noise.[62] For this reason, it is imperative to have a consistent way of characterizing the dimensions of a quantum system.

For single photon channels, it should be easy to see that the dimensionality is set by the number of modes that can be transmitted through the channel and detected successfully while maintaining high mutual information. Further restrictions on d can be set by the apertures of the system as well as the angular spectrum and resolution of the generation and detection techniques;[67] this means that modes requiring high spatial resolution will incur noise, so fewer modes can be used.

For the two photon case, we return to our decomposition of the OAM entangled photons in Eq. (10), where the coefficient for each Schmidt basis state is given by c_ℓ. The dimensions, d, of this state can be characterized using the Schmidt number witness,[68] which can be estimated from projections with two mutually unbiased bases.[28] For an entangled state with $c_\ell = \frac{1}{\sqrt{d}}$, the Schmidt number is exactly d. This has a significant implication in high-dimensional entangled systems, as this quantifies the "amount" of entanglement in these systems.

Generalized to systems that are not necessarily maximally entangled, this number can instead be approximated by[69,70]

$$K = \frac{1}{\sum_\ell |c_\ell|^4}, \tag{14}$$

where $K = 1$ dictates a separable system and $K > 1$ indicates an entangled one, assuming the coefficients are normalized. K thus provides an effective number of the contributing modes to the entangled state and thus refers to the *dimensionality* of the system (see Sec. 2 of Ref. 71 for an in-depth discussion).

C. Linear entropy

While higher dimensional states are resilient to noise, some protocols strictly require that the states be completely pure or, equivalently, have a low degree of mixture. Therefore, it is imperative to characterize the purity of the states. The purity can be obtained from $\gamma = 1 - S_L$, where S_L is the linear entropy and can be expressed as

$$S_L = 1 - \mathrm{Tr}\,(\rho^2), \tag{15}$$

where ρ is the density matrix of the state. For maximally mixed states, the purity is $\gamma = 1/d$, while for pure states, it obtains a maximal value of $\gamma = 1$.

11 June 2026 13:34:37

© Author(s) 2023

The purity of the state can also be used as an indicator of the entanglement in a quantum system. For example, we find that the purity for the isotropic Werner-like state in Eq. (11) is given by

$$\gamma_{iso} = p^2 + \frac{(1-p)^2}{d^2}. \tag{16}$$

In higher dimensions, the purity $\gamma_{iso} \approx p^2$ because the second term becomes insignificant, and thus the purity is only dependent on p. For this reason, the factor p is associated with purity and has been used as a control parameter for probing the robustness of entanglement to noise[62,72] in the temporal, pixel, and OAM degrees of freedom of photons.

IV. CREATION AND DETECTION

In this part of the tutorial, we introduce the reader to techniques that are commonly used to produce, detect, and characterize high dimensional quantum structured light in the laboratory. We focus on the spatial degree of freedom of photons that are generated from SPDC. We subsequently discuss basic procedures for aligning a simple quantum experiment with SPDC photons and executing spatial projective measurements. We end the section by discussing methods for optimizing the generation and measurement steps.

A. Photon pair generation with spontaneous parametric down conversion

1. Spontaneous parametric down conversion from nonlinear crystals

One of the most commonly used approaches for generating quantum structured light uses crystals with a second-order susceptibility via three-wave mixing through a process called spontaneous parametric down-conversion (SPDC), and so we will use this as our source throughout this tutorial (for other possibilities, see recent reviews[73,74]). Examples of crystals that enable this process are beta-barium borate (BBO), lithium niobate (LN), potassium dihydrogen phosphate (KDP), and potassium titanyl phosphate (KTP).

Figure 5(a) shows a cartoon description of the SPDC process where a pump (p) beam of angular frequency, ω_p, interacts with a non-linear crystal, resulting in the generation of two daughter photons of ω_s and ω_i, respectively. Due to the conservation of energy, the angular frequencies of said signal (s) and idler (i) are governed by the relation $\omega_p = \omega_s + \omega_i$. This relation is shown in the energy level diagram in Fig. 5(b). Accordingly, the entangled biphotons need not have the same energy $(\omega_s = \omega_i)$, termed *degenerate* SPDC, but can be *non-degenerate* $(\omega_s \neq \omega_i)$.

Linear momentum is also conserved in the SPDC process; the momentum of the produced photons should add to that of

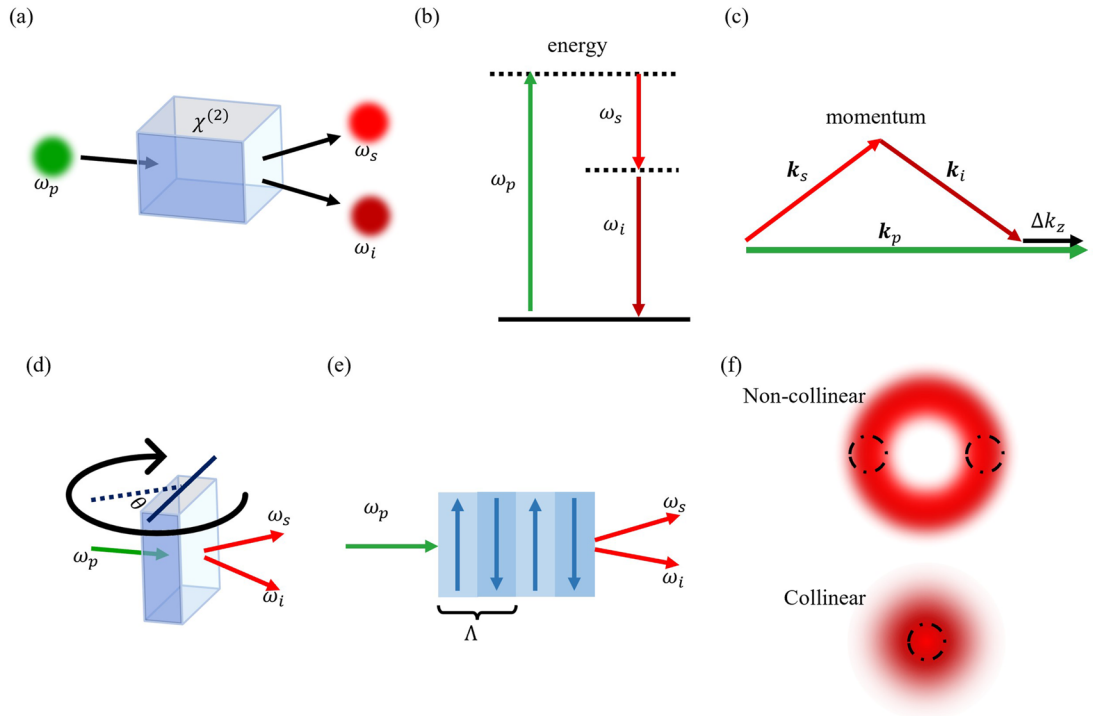


FIG. 5. Spontaneous parametric down-conversion. (a) Generation of SPDC photons from nonlinear crystals (NC) that are characterized by a second order nonlinear susceptibility tensor, $\chi^{(2)}$. In this process, a single photon with a frequency, ω_p, is absorbed by the crystal, and twin photons with frequencies, ω_s and ω_i, are produced. (b) Energy diagram for the three photons involved in SPDC, showing energy conservation. (c) Momentum conservation in the SPDC process. The momentum vectors of the emitted *s* and *i* photons must add up to those of the pump photon. The phase mismatch occurs in the longitudinal direction. The emission cones can be altered by changing the phase matching conditions. This can be achieved via (d) angle tuning in bulk crystals and (e) temperature tuning in periodically poled (PP-) crystals. (f) Far-field intensity profiles of SPDC photons showing non-collinear and collinear geometries where the entangled photons are found in the regions highlighted with dashed lines.

11 June 2026 13:34:37

© Author(s) 2023

the pump, resulting in $\mathbf{k}_p = \mathbf{k}_s + \mathbf{k}_i$, shown pictorially in Fig. 5(c), expressed using the wave vectors, $\mathbf{k}$, of the respective pump, signal, and idler photons. If energy and momentum conservation are met, one has perfect phase matching. On the contrary, phase mismatch occurs and is proportional to Δk_z, in the longitudinal momentum components, as illustrated in Fig. 5(c). In order to alter the phase-matching conditions, most bulk crystals require angle tuning, as shown in Fig. 5(d), where the angle of incidence of the pump mode with respect to the crystal is varied. Alternatively, one can use periodically poled crystals [shown in Fig. 5(e)] with engineered domain switching of a period of Λ.[75,76] For these crystals, the phase matching conditions can be altered by changing the temperature of the crystal.

There are two types of phase-matching geometries that can be identified based on the matching of linear momentum. In Fig. 5(f), on the top panel, the output field propagates off-axis with respect to the pump, but with equal and opposite trajectories on either side; this is known as non-collinear SPDC. The emitted photons, in this case, are anti-correlated in transverse momentum and, therefore, the entangled photons are located on any two opposite ends of the SPDC ring. For collinear SPDC, shown in the bottom panel of Fig. 5(f), the output field wave-vectors are also anti-correlated, except when $k_s = k_i = 0$.

Due to the polarization sensitivity and phase-matching conditions, there are different phase-matching regimes that can be engineered. This results in different polarization pairings with active research considering exotic fabrications and crystal pairings, allowing one to engineer unique geometries and output states. A good review covering this can be found in Ref. 77. For this tutorial, we will consider the generic cases commonly available and summarized in Table I.

The distinction between the different types relies on the relative polarizations with respect to the crystal's ordinary (o) and extraordinary (e) axes. The examples shown in Table I are special cases but can, in general, be summarized as follows: in type 0, the signal and idler photons carry the same polarization as the pump, whereas in type I, their polarization is orthogonal to that of the pump; for type II, however, the signal and idler photons are orthogonally polarized with respect to each other, leading to polarization entanglement. We note that these characteristics are all determined by the nonlinear electric tensor of the crystals.

2. Spatial mode entanglement from SPDC

In the SPDC process, photon pairs can be entangled in their energy-time,[78,79] path,[80] and transverse spatial degrees of freedom[24,49,52,81–83] (see Ref. 84). In this tutorial, we focus on *discrete* spatial modes and thus consider the entanglement generated therein.

TABLE I. Phase matching types. Summary of various phase-matching regimes for second order non-linear interactions that differ for input and output field polarization with respect to parallel orientation to the crystal's ordinary (o) or extraordinary (e) axes.

Type	Pump pol.	Signal pol.	Idler pol.
0	o	o	o
I	e	o	o
II	e	o	e

It is useful to consider the general expression of the SPDC state in terms of wavefunctions for the generated photons on a linear momentum basis. One method to derive this evolves the quantum state by using the non-linear phenomenological Hamiltonian.[85–87] For brevity, we will use the main result, which is the two photon state,

$$|\psi_{s,i}\rangle = \int f(\mathbf{q}_s, \mathbf{q}_i)|\mathbf{q}_s\rangle|\mathbf{q}_i\rangle \, d^2q_s \, d^2q_i, \tag{17}$$

expressed in the transverse momentum coordinates, $\mathbf{q}_s$ ($\mathbf{q}_i$), where $f(\mathbf{q}_s, \mathbf{q}_i)$ is the two-photon joint probability amplitude of the pair of photons, s and i, respectively. Assuming that the pump beam impinging on the crystal has a Gaussian profile in the far-field, the joint probability amplitude function is given by[77,88]

$$f(\mathbf{q}_s, \mathbf{q}_i) = \mathcal{N} \underbrace{U(\mathbf{q}_s + \mathbf{q}_i)}_{\text{pump}} \underbrace{\text{sinc}\left(\frac{L\Delta k_z}{2}\right)}_{\text{phase-matching}}, \tag{18}$$

and is a product between the pump mode, $U(\cdot)$, expressed in the momentum coordinates, $\mathbf{q}_p = \mathbf{q}_s + \mathbf{q}_i$, and the phase matching function, $\text{sinc}\left(\frac{L\Delta k_z}{2}\right)$, that is determined by the crystal length, L, in the longitudinal direction and the longitudinal wave-vector mismatch, Δk_z. The factor $\mathcal{N}$ is a normalization constant. The pump beam of a Gaussian profile can have an angular spectrum, $U(\mathbf{q}_s + \mathbf{q}_i) \propto \exp\left(\frac{-w_p^2|q_s+q_i|}{4}\right)$, where the w_p is the waist size in the near-field.

Furthermore, the longitudinal wave-vector mismatch mainly affects the spectral properties of the generated SPDC photons and is given by $\Delta k_z = k_{p,z} - k_{s,z} - k_{i,z}$, depending mainly on the relative difference between the longitudinal components of the wave vectors of the pump photon and emitted pairs. Accordingly, if the emission angles of the SPDC photons (i.e., the angles between $\mathbf{k}_{s,i}$ and $\mathbf{k}_p$) are sufficiently small, then the longitudinal wave-vector mismatch can be approximated by[89]

$$\Delta k_z = -\frac{|\mathbf{q}_s - \mathbf{q}_i|^2}{2k_p}. \tag{19}$$

Under these assumptions, we can express the constants in the argument of the resulting phase matching function, as $\frac{Lw_p^2}{8z_R}$, where $z_R = \frac{1}{2}k_p w_p^2$ is the Rayleigh length of the pump beam. From here on, we assume that we can use the thin crystal limit, $L \ll z_R$, so that the phase matching function evaluates to one. We can now approximate the joint probability mode function (equivalently, the two photon wave-function) with the pump profile, i.e., $f(\mathbf{q}_s, \mathbf{q}_i) \approx U(\mathbf{q}_s + \mathbf{q}_i)$. Now, our aim is to express the two photon states given any complete transverse spatial basis. Suppose we have a discrete Schmidt basis, $|j\rangle_s|k\rangle_i$, one can express our two photon states in Eq. (20) as an entangled two photon state,

$$|\psi_{s,i}\rangle = \sum_{jk} c_{jk}|j\rangle_s|k\rangle_i, \tag{20}$$

11 June 2026 13:34:37

© Author(s) 2023

where the coefficients are given by[30]

$$c_{jk} = \int f(\mathbf{q}_s, \mathbf{q}_i) M_j^*(\mathbf{q}_s) M_k^*(\mathbf{q}_i) d^2 q_s d^2 q_i, \tag{21}$$

and the mode functions $M_{j(k)}(\mathbf{q})$ are eigenfunctions that map onto the eigen-states $|j(k)\rangle$ expressed in the transverse momentum basis. Noting that the joint probability amplitude is approximated by the pump field (preferably a paraxial optical field), it is possible to map the integral to the spatial basis $|\mathbf{r}\rangle_{si}$, where it can be evaluated in the near field by Fourier transforming Eq. (21). Accordingly, the overlap integral becomes

$$c_{jk} = \mathcal{N} \int u(\mathbf{r}) m_j^*(\mathbf{r}) m_k^*(\mathbf{r}) d^2 r. \tag{22}$$

Here $u(\cdot)$ is the pump mode in the near field, while $m_{j,k}(\cdot)$ are the Fourier transforms of the modes $M_{j,k}(\cdot)$. Examples of suitable bases are the discrete pixel modes,[52] Hermite–Gaussian, Laguerre–Gaussian, and Bessel–Gaussian modes. In all cases, different parameters such as the transverse correlation length, point spread function of the experimental setup, and angular spectrum of the pump mode can have an impact on the bandwidth of the measured spectrum as well as the correlations. We show an example using the LG basis formed from modes with the radial index set to $p = 0$, i.e., $|\ell\rangle \equiv LG_{\ell_p,p=0}\rangle$. Suppose that the pump photon carries OAM, $u(\mathbf{r}) = LG_{\ell_p,p=0}(\mathbf{r}) \propto \exp(i\ell_p\phi)$. By evaluating the overlap integral in the cylindrical coordinates, one finds that the azimuthal integral induces the restriction that the coefficients are nonzero when $\ell_p = \ell_s - \ell_i$ showing OAM conversation in the SPDC process. As such, one arrives at the state in Eq. (10), repeated here as

$$|\Psi_{si}\rangle = \sum_{\ell_s=-\infty}^{\infty} c_\ell |\ell_s\rangle_s |\ell_p - \ell_s\rangle_i. \tag{23}$$

In Subsections IV B–IV F, we show how one can prepare and measure these states in the lab and discuss some of the intricacies involved in detecting them.

B. Alignment and back-projection

Typically, quantum optical setups can be aligned both forwards and backward (backprojection) in order to ensure both entangled photons sent through the system travel the desired path and coincide well with the detection system. Accordingly, we will first look at typical forward alignment strategies for different types of SPDC, which are illustrated in Fig. 6, before seeing how back-alignment works and, ultimately, how one may view the system for simulation.

The alignment of the SPDC depends both on the type of trajectory of the entangled photon pair one wishes to measure (collinear or non-collinear) as well as the distinguishing properties between them. The simplest configuration lies with collinear SPDC. As the linear momentum of the biphotons lies in the same direction as the pump, one may use the pump laser as a guide throughout the optical setup. Separation of the biphotons into the desired arms of the system can then be achieved by passing them through a 50:50 beamsplitter when they hold the same polarization and wavelength, as shown in the top illustration of Fig. 6. Alternatively, if the SPDC is non-degenerate, as in the second illustration in Fig. 6, one may employ a

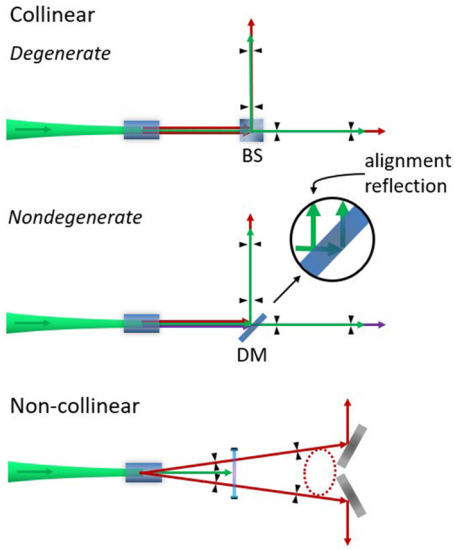


FIG. 6. Generic SPDC alignment strategies. Typical strategies for alignment of quantum systems with collinear and non-collinear SPDC sources and how they may differ for the degenerate and non-degenerate cases. Irises (black triangles) are typically placed in the beam paths for each arm in order to mark the path of the photons.

dichroic mirror (DM) to separate the wavelengths. In this case, the side coated for the reflected wavelength should be the incident face. When considering the pump beam as a guide, two parallel beams are traditionally reflected as a result of incidence on the front and back sides of the optic, as illustrated in the inset. If orientated correctly, the first reflection of the pump beam should indicate the path of the reflected photons. Depending on the cutoff wavelength between the reflected and transmitted light, the pump beam will be brighter in either transmission or reflection. For cases where the pump is not bright enough to see both the transmission and reflected intensities through the DM, another wavelength in the complementary wavelength band may be aligned with the pump beam beforehand, or one may consider relying on back alignment alone.

For non-collinear SPDC, the alignment varies appreciably as the biphotons no longer travel in the direction of the pump beam but rather in opposite directions to either side. This corresponds to selecting the photons on opposite ends of the cone shown in Fig. 5(f), which we see illustrated in the horizontal plane of the last illustration of Fig. 6. The pump may no longer act as a guide in this case. This results in the need to see the SPDC cone produced with a sensitive CCD and align through two apertures in each arm to opposite transverse sides of the cone for planes with an appreciable distance between them. These apertures then allow one to use back alignment in order to align the rest of the optical elements from these points.

For back alignment, one must consider the optical system in its entirety. For instance, considering the typical system in Fig. 7(a), after traversing the desired optical elements [such as the lenses and spatial light modulators (SLMs)], the biphotons are each focused into single mode fibers (SMF), which relay them to sensitive detectors like avalanche photodiodes (APD). Back alignment then

11 June 2026 13:34:37

© Author(s) 2023

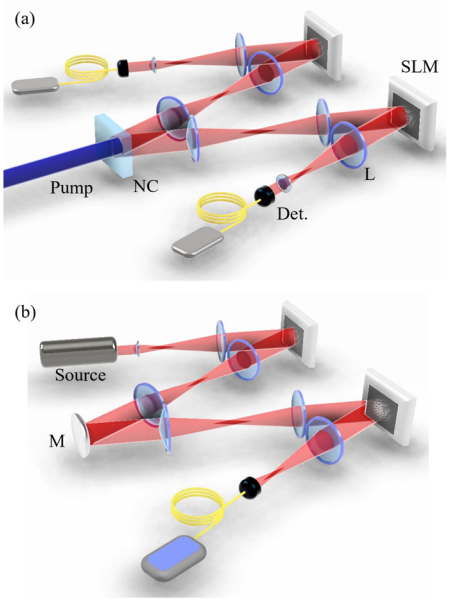


FIG. 7. Klyshko model for a quantum system. Demonstration of the Klyshko model for quantum systems where the non-linear crystal (NC) in the optical system (a) can be seen as a mirror (M) in the model (b). Experimentally, the setups are almost identical. In the quantum setup (a), a pump beam is incident on an NC, which produces our SPDC state consisting of entangled photon pairs, which are then spatially separated into the two arms of the experiment. The SPDC state is imaged onto the SLMs with lenses (L) and measured using single photon detectors (Det). In the Klyshko back-projection model, one of the detectors is replaced by a source, and a single beam is sent through the setup by replacing the NC with a mirror.

considers this system in reverse. One can envision that if the photons can travel to the detector in the forward direction, light traveling in the opposite direction from the same point in the detector must travel the same path. As such, an additional laser is used where the light is sent back through the detection end of the fiber (replacing the detectors in the figure) such that it traverses the elements backward toward the crystal face. By using this backpropagating light, one may then align the couplers and optical elements as desired. Here, one may be aided by using the same wavelength as the SPDC to ensure the optical operations observed in back alignment correspond well and are not shifted due to the difference in wavelength.

When the forward alignment overlaps well with the back alignment, one should see the signal at the detector, allowing one to further improve the setup and take measurements. For the non-collinear geometry discussed earlier, forward alignment ends at the initial apertures. The alignment of the backpropagating laser through the initial aperture then sets the path such that alignment of the optics is performed with this laser as a guide instead of the pump. Fine tuning of the phase matching may then also be achieved by aligning the detection SMF back through the apertures used for the pump and checking that the maximal counts lies at the correct crystal parameters, be it temperature or angle.

An additional method exists that allows one to experimentally simulate and probe a quantum optical system using classical light. Here, when looking at the setup in a retrodictive manner, the quantum system at any point in time may simply be described by evolving the measured states backward in time.[90] Based on a rigorous formulation, it was shown by Kyshko in 1988 that one may employ back-propagation to generate a classical analog that predicts the measured quantum correlations produced from the optical system being traversed by the biphotons. Known as the Klyshko advanced wave model, the nonlinear crystal is replaced with a mirror, and in one of the detection arms, the detector is replaced with a laser. This formulation is illustrated in Fig. 7(b). As can be seen, the light then passes through the system, bounces off a mirror positioned where the crystal was, and traverses the other arm in the forward direction before being detected in place of the correlated SPDC photon. The corresponding intensity measurements then reflect the coincidences that would be seen when detecting the biphotons in the equivalent quantum setup. For example, the measurements yield the conditional probability of detecting a photon in one arm, given that another photon is detected in the other arm.

Furthermore, the effect of the pump beam on the system can also be modeled by simply adjusting the properties of the mirror substituting for it. For instance, when the pump beam is not a plane wave in the crystal, the phase curvature is equivalent to the mirror being curved, or when the pump is angled, it equates to the mirror being tilted at the related angle.[91–93]

It may be noted that, in addition to the rigorous theoretical formulation, it has been experimentally verified, showing excellent agreement in comparison to the quantum outcomes.[94,95] Consequently, this not only provides a good way to numerically model the system but also serves as a good probe in order to determine and correct the physical parameters that affect the desired system.

C. Coincidences

Detection of the entangled photons in a quantum experiment is traditionally achieved by distinguishing time correlations in the signals received by the detectors. As each of the entangled photons is "birthed" at the same time in the crystal, they should arrive at their respective detectors at exactly the same time (within the uncertainty principle) or after a set delay related to traveling different distances before reaching the detectors. This yields a way to distinguish them from other non-correlated detection events (photons that are not entangled) or noise, with a pair being detected in the appropriate interval being called a coincidence.

Practically, these can be detected using event timers that log the time of arrival for each photon signal and looking at the difference in the time delay between each photon detected in arm 1 and every photon detected in arm 2, or vice versa. Subsequently, these entangled photons are identified by taking a histogram of the detected photons where all the respective time differences (Δt) between the signals form values in discretized timebins (e.g., 40 ps) from each of the arms, as illustrated in Fig. 8. Due to the aforementioned time correlation, the entangled photons will be found to have the same time difference, and thus the counts or signal in that time bin of the histogram will increase, such as in the second time bin of the histogram. Conversely, stray or uncorrelated light that does not have a set correlation will be spread randomly across all the other bins and thus not have any specific signal buildup. This then gives a degree of

11 June 2026 13:34:37

© Author(s) 2023

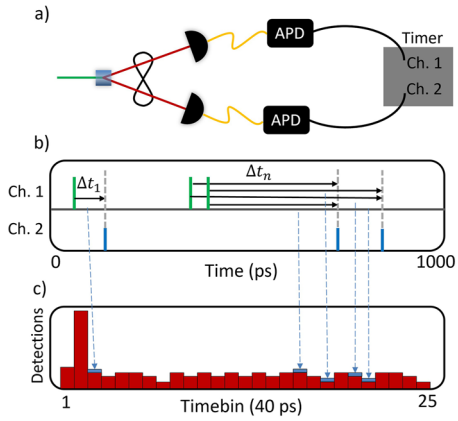


FIG. 8. Coincidence detection. A typical biphoton quantum setup utilizes two detectors (APDs in this case) to detect individual photon events, and a timer observes such events over a certain time period. Correlations are then drawn between events in both channels according to delay time, Δt_n. (b) For a series of events detected by channels 1 and 2 shown in the 1000 ps time window, events are (c) time-binned according to relative time delays between events in each channel. For example, if an event is detected at time t_1 by channel 1, the time tagger compares this event to all other detected events in channel 2 in the same time window and orders events in timebins corresponding to the relative time delays between t_1 and all other detected events in channel 2. This is performed for all detected events in channel 1. Once this process is completed, one observes a peak around the expected delay time between correlated photon pairs from the SPDC process.

noise that depends on the ratio of entangled photons being detected to stray or uncorrelated light. It may be noted that there is a degree of uncertainty in the processing and propagation times of devices like the event timer and APD. As a result, this time delay correlation will also "spill over" or spread into adjacent time delay bins of the histogram if the timebins are made on the order of the jitter in the detectors and instruments.

D. Noise

It should be noted that there are several factors that may lead to noise and other uncertainties in quantum experiments, such as those besides the jitter in the instruments. First, we can consider the statistical nature of the biphotons. Here, their generation in SPDC is spontaneous, meaning each pair event is independent of the next, resulting in the generation times being governed by Poissonian statistics. More specifically, one may quantify the probability of the emission times of these pair generation events in terms of time bins relative to some fixed reference. Here, the probability of finding the k number of photon generations in a time bin, t, is given by a Poisson distribution and can be described by

$$P(k) = \frac{N^k e^{-N}}{k!}, \tag{24}$$

with N being the average number of pairs per timebin. As a result, the variance in this distribution is given by the mean, resulting in the standard deviation $\sigma_{P(k)} = \sqrt{N}$. This means the uncertainties in the coincidences measured (which is given by N) have a fundamental uncertainty of $\sqrt{N}$.

One may also work out the probability of erroneously detecting a coincidence due to two uncorrelated photons arriving at both detectors at the same time. These are referred to as accidentals (N_{Acc}) and may be estimated based on the timebin window used (Δt) and how high the counts are in both the signal (C_{Ch1}) and idler (C_{Ch2}) arms that are used to determine the coincidences,

$$N_{Acc} = C_{Ch1} \times C_{Ch2} \times \Delta t. \tag{25}$$

Consequently, larger signals in each arm used to obtain coincidences yield larger numbers of accidentals. A common measure that determines the signal-to-noise ratio in photon correlations is the quantum contrast, $Q = N_{Coin}/N_{Acc}$. Accordingly, a large coincidence detection window allows a greater probability for including uncorrelated light into the coincidence values and, therefore, to increase the quantum contrast, narrow gating times (1 ns) are usually preferred so that the accidental counts are reduced.

Another notable source of noise in the production of entangled photon pairs by pumping a crystal is the generation of additional pairs within the same coincidence window.[96–98] This results in impurity in the detected coincidences, as they form a statistical mixture rather than a pure source to utilize.[99] As a result, the event of generating multiple bi-photons serves to reduce the fidelity of the entanglement. Several works have been published in an active effort to solve this;[100–102] however, this involves generally complex configurations. The straightforward approach to mitigating the additional bi-photon generation events is a reduction in the intensity at which the crystal is pumped. While this reduces the efficiency at which the desired single bi-photons are produced, a much larger reduction in the multiple bi-photon probabilities serves to increase the fidelity. Further, the probability of having multiple photon pairs scales with the photon generation rate, μ. As such, for a given photon generation rate, the quantum contrast (signal-to-noise ratio) is determined by[72]

$$Q = 1 + \frac{\mu(1+\mu)}{(\beta+\mu)^2}, \tag{26}$$

where β is the ratio between the probability of detecting background photons (from ambient light or noise in the detectors) and the collection efficiency. A preferred photon generation rate is $\mu \ll 1$, as this reduces the generation of multiple pairs and increases the quantum contrast. On the other hand, $\beta \ll 1$ is also preferred. This can be achieved by ensuring that the collection and transmission efficiency of the apparatus used is high (near unity if possible), that the detectors have a high quantum efficiency and low dark count rates, and that the experiment is shielded from ambient light. This can significantly improve the fidelity of measurements in the experiment since noise contributions will be minimized.

As such, the average quantum contrast that is required to witness entanglement in k dimensions, given a d dimensional space is[72]

$$Q > \frac{d-1(d+k-1)}{d-k+1}. \tag{27}$$

11 June 2026 13:34:37

© Author(s) 2023

Here, d can be determined from the spiral bandwidth, while the determination of k requires a suitable entanglement witness.[28]

E. Detection and measurement of quantum structured light

1. Detection using projective measurements

High-dimensional states require a reliable method of detection where projections into some orthogonal basis are needed. If we consider the SPDC state given by Eq. (23), then a detection scheme is required that can distinguish between different OAM states. In fact, what we need is a coupled detection system that only accepts a single OAM state, $|\ell_{\text{Det}}\rangle$. For the example of OAM used in this tutorial, we use what is known as a spatial light modulator (SLM) coupled with an SMF. It is worth noting that this detection scheme works just as well for any chosen spatial basis, such as the Hermite–Gaussian, Ince–Gaussian, and pixel mode bases, to name but a few and, therefore, extends past OAM, making it an ideal scheme to be used to generate and detect spatial modes of single photons and measure correlations between entangled photons of high-dimensional quantum states.

The detection of spatial modes with SLMs borrows from methods that are commonly used for creating arbitrary light fields in beam shaping.[103] In beam shaping an incoming light field, usually, the fundamental Gaussian mode ($|0\rangle \equiv |\text{LG}_{0,0}\rangle$) is modulated in phase and amplitude using an SLM. As for the detection, the reciprocal nature of light is employed, where one is able to "reverse" the modulation of a particular field back to the fundamental Gaussian state, which is subsequently coupled to a single mode fiber and a photon counting module.[104,105] This approach flattens the field. The concept is illustrated in Fig. 9(a), where the fundamental mode is converted into a desired spatial pattern, $\Phi(\mathbf{r})$, and can be detected in reverse. Consequently, the fiber and the SLM form an optical correlation measurement that is analogous to performing an inner product measurement of the form $|\langle\Phi|\Psi\rangle|^2$ for some input field $\Psi(\mathbf{r})$ and some target (detection) mode $\Phi(\mathbf{r})$.[105] Furthermore, to maximize coupling efficiency, the creation and detection beam sizes need to be comparable. As outlined, two elements are at play: (i) the detection mode that is encoded as a hologram ($H\Phi(\mathbf{r})$), and (ii) the probability of the demodulated mode coupling into the single mode fiber. In this and the proceeding sections, we place emphasis on this coupled detection scheme, focusing on the different optical inner-product measurements that overlap the state $|\Psi\rangle$ with the state $|\Phi\rangle$ using SLMs and fibers. Later, we extend this to entangled photons.

Spatial light modulators typically come in two forms. One is a phase-only modulator, and the other is an amplitude-only modulator. With a few clever tricks, both of these devices can be used to manipulate or modulate the amplitude as well as the phase profiles of your input photons. In this tutorial, we will focus on phase-only modulation devices. For more information on using amplitude-only devices, see Ref. 106.

We can consider the action of the SLM on the input state, $|\Psi\rangle$, to be given by a phase modulation function $H(\Phi(\tilde{r}))$, commonly called the hologram. As will be seen, by incorporating a grating function, one is able to encode the amplitude in addition to the phase of the optical field with phase only modulation.[107] Accordingly,

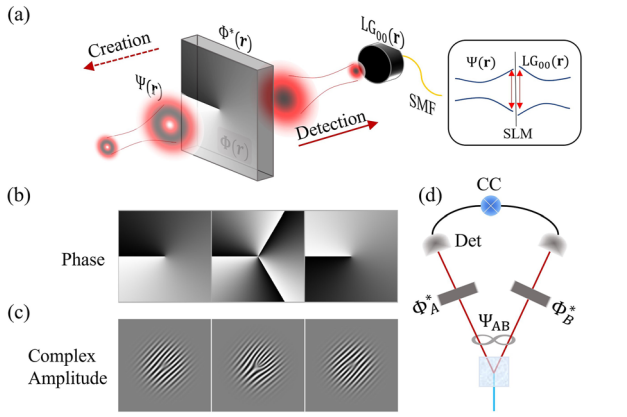


FIG. 9. Detection scheme for high dimensional states. (a) The detection scheme for an input field $\Psi(\mathbf{r})$ impinging on an SLM encoded with a hologram $\Phi^*(\mathbf{r})$. The SMF then accepts only the $LG_{0,0}$ component of the output field. Reciprocally, we see the usual SLM modulation scheme where the SMF now acts as our source producing the mode $LG_{0,0}$, which is incident on the SLM encoded with $\Phi(\mathbf{r})$, thereby producing the desired mode (or, depending on the encoding scheme, a superposition of modes is created with the desired mode being among them). (b) Examples of encoded phase holograms (no grating) with encoded hologram functions taking the form $H(\Phi(\mathbf{r})) = \exp(i\ell\phi)$ for $\ell = 1, 3, -1$. (c) Examples of complex-amplitude holograms (grating included) with encoded hologram functions taking the form $H(\Phi(\mathbf{r})) = |LG_{\ell,0}|\sin(\arg(LG_{\ell,0}) + \Lambda_{grating})$ for $\ell = 1, 3, -1$. (d) Schematic of the detection scheme for a biphoton state $|\Psi\rangle_{AB}$.

this means that the hologram has a phase transmittance function, $\Phi^*(\mathbf{r}) \sim \exp(iH(\Phi(\tilde{r})))$.[107]

The hologram function in general can be seen as a mapping of the form

$$H(\Phi(\tilde{r})) : |\Psi\rangle \rightarrow \eta|0\rangle + \sum_{(\ell,p)\neq(0,0)} \alpha_{\ell,p}|\text{LG}_{\ell,p}\rangle, \tag{28}$$

where the first term is the desired fundamental mode that will be coupled to the SMF, and the rest of the terms are unwanted modes and diffraction orders. Here, the SLM and fiber act as a match filter: if the incoming mode and the SLM hologram result in a fundamental mode in the first order, then the mode on the SLM must have been the complex conjugate of the input mode. For example, consider the case where the input photon is a vortex mode, $\Psi(\mathbf{r}) = G(\mathbf{r})\exp(i\ell\phi)$, and the SLM encodes the mode $\Phi^*(\mathbf{r}) = \exp(-im\phi)$, where $G(\mathbf{r})$ is the fundamental Gaussian mode. After the SLM, the photon will have the field profile $\Psi(\mathbf{r}) \times \Phi(\mathbf{r})$. Therefore, the field profile of the photon will be that of the fundamental mode of the fiber if and only if $m = \ell$. This means that the first term in Eq. (28) is non-zero for $m = \ell$, while the other unwanted terms are filtered by the fiber.

The other modes in Eq. (28) can also be attributed to artifacts of the modulation technique used on the SLM. Ultimately, regardless of the technique used, modes besides the fundamental mode are filtered out when passing through an SMF. The probability of obtaining the fundamental mode is given by $\eta \propto |\langle\Phi|\Psi\rangle|^2$. How can we encode the holograms as a function that achieves this mapping?

11 June 2026 13:34:37

© Author(s) 2023

In general, one can define the hologram phase modulation that encodes $\Phi^*(\mathbf{r})$,[108]

$$H(\Phi(\mathbf{r})) = f(\Phi^*(\mathbf{r})) \times h\big(\arg \Phi^*(\mathbf{r})\big), \tag{29}$$

where $f(\cdot)$ is the relation chosen to describe how the efficiency changes with grating depth, while $h(\cdot)$ encodes the phase, $\arg(\Phi^*(\mathbf{r}))$. By setting $f(\cdot) = 1$ and $h = \mathrm{mod}\left[\arg(\Phi^*(\mathbf{r})) + \Lambda_{grating}, 2\pi\right]$, we obtain a blazed phase grating that allows for phase-only detection, where the grating is controlled by the term $\Lambda_{grating}$. This technique is known as phase modulation and works by unraveling the phase without altering the amplitude. By loading this *phase-only* hologram on the SLM, one physically alters the phase of a photon by changing the orientation of liquid crystal (LC) molecules in the SLM pixels, as the orientation dictates the refractive index of the material seen by the field.[108] This change in orientation results from applying a voltage across a section or cell of such molecules as dictated by the phase values at each pixel. A collection of such pixels comprises the SLM screen, onto which we direct the photon we wish to detect. We show examples of such holograms in Fig. 9(b) with $\Lambda_{grating} = 0$ in order to emphasize the phase ramp. A more detailed explanation of this and the methods described here is well covered in Ref. 108. Here the grayscale image has 256 values, which refers to the number of voltage levels and, therefore, orientations of the LC molecules that the device can program for each LC cell or pixel. It thus follows that there are 256 levels that can be encoded onto the SLM, implying that the phases modulated in this example need to be quantized into 256 values.

Considering that we have control over the individual LCs of the SLM and that we can tailor the phase of arbitrary fields, the next step is to consider how we may use it to map the amplitude information, $f(\Phi(\mathbf{r}))$, if we wish to measure complete amplitude and phase. The simplest approach is to modulate the blaze grating with the field amplitude [see example holograms in Fig. 9(c)]. This approach might be efficient but may come at a loss of accuracy since the field amplitude does not map linearly with conversion efficiency. Alternative methods can be found in Refs. 107, 109, and 110. Furthermore, we direct the reader to Ref. 111 for a comparison of commonly used techniques. One relation for $f(\cdot)$ that can produce the best outcome was reported in Ref. 107, where the amplitude function is encoded as, $f(\Phi(\mathbf{r})) = J_1^{-1}(\Phi(\mathbf{r}))$. Here, $J_1^{-1}(\cdot)$ is the Bessel function of the first kind. The phase function is altered as $h = \sin\left(\arg(\Phi^*(\mathbf{r})) + \Lambda_{grating}\right)$.

With these phase modulation techniques, it is possible to prepare complex amplitude holograms that accurately encode (or reciprocally detect) the target mode $\Phi(\mathbf{r})$. Next, we unpack the final detection step, where the fiber is used as a tool to achieve the mapping in Eq. (28) in order to filter out the desired fundamental mode once the hologram has modulated the photon field.

2. Influence of optical fibers on the measurements

Following the modulation of the input field $\Psi(\mathbf{r})$ by an SLM encoded with $\Phi^*(\mathbf{r})$ and the subsequent coupling of the resulting field onto the SMF and photon counting module, photon counts that are proportional to the desired overlap probability are obtained, $|\eta|^2$. The corresponding overlap integral that determines the measured photon rates is governed by[105]

$$\eta = \int \Psi(\mathbf{r})\Phi^*(\mathbf{r}) e^{-\frac{r^2}{w^2}} d\mathbf{r}^2, \tag{30}$$

where the Gaussian factor is the fundamental mode that propagates in the fiber. If we consider taking the beam waists of the input field and the encoded hologram function to be much smaller than that of the fiber, w, then one can assume that any significant contribution from the integral in Eq. (30) comes from regions where $e^{-\frac{r^2}{w^2}} \approx 1$; therefore, the calculation becomes an inner product between the input field and encoded mode, $\eta = \langle \Phi(\mathbf{r}) | \Psi(\mathbf{r}) \rangle$.

The above-mentioned steps give us a recipe for detecting arbitrary single photon states. Now we consider two photon states. To see how the technique works, consider the biphoton state $|\Psi\rangle_{AB}$ described in the OAM basis by the SPDC state given in Eq. (10). Detection of the said state involves utilizing our coupled detection scheme on each individual photon, independently, as shown in Fig. 9(d). However, this follows rather simply from the single photon case, where we compute an inner product between encoded mode functions, $\Phi_A(\mathbf{r})$ for photon A and $\Phi_B(\mathbf{r})$ for photon B, and the field dictating the photon correlations. The overlap integral takes the form[105]

$$\begin{aligned} \eta_{AB} &= \langle \Phi_B(\mathbf{r}) | \langle \Phi_A(\mathbf{r}) | \Psi_{AB}(\mathbf{r}) \rangle \rangle, \\ &= \int \Psi_{AB}(\mathbf{r}) \Phi_A^*(\mathbf{r}) \Phi_B^*(\mathbf{r}) e^{-2\frac{r^2}{w^2}} d^2 r, \end{aligned} \tag{31}$$

where $\Psi_{AB}(\mathbf{r})$ is the two photon joint probability amplitude that is determined by the entanglement source, while the Gaussian factor includes the contribution of the fibers that are used to collect each photon. In general, it is important to optimize the crystal (phase matching) and experimental parameters (fibers, lenses, and apertures) for the desired detection basis and application. Several experiments have demonstrated the detection of high dimensions in the OAM and pixels basis.[32,52,112,113]

In Fig. 10(a), we show the detection of OAM modes from SPDC, where each photon is projected into OAM modes $\Phi_{A,B}(\mathbf{r}) \sim \exp(i\ell_{si}\phi)$ with corresponding charges of $\ell_{s,i}$ for photons A (signal) and B (idler), respectively. Figure 10(b) shows the corresponding spectrum for $\ell_s = -\ell_i$ taken from Fig. 10(a). This configuration produces a fixed number of modes ($\approx$21). The number of generated and detected modes can be affected by the source parameters (input mode and crystal parameters) and the quality of the detection system. Next, we show how the source and detection systems can be optimized to achieve such higher dimensional encoding.

3. Optimizing the measurement of quantum structured light

Limiting parameters affecting the extent of our spatial entanglement here may be reduced to two factors on the generation side: the pump size and crystal length. This may be seen by decomposing the SPDC wavefunction [Eq. (17)] into the LG basis for $p = 0$, and the waist size is scaled with respect to that of the crystal and pump, $\beta = w_p \sqrt[4]{\frac{L}{2z_R}}$, in order to determine the coefficients, c_ℓ, in Eq. (23). It may be noted that further decomposition into the radial terms,

11 June 2026 13:34:37

© Author(s) 2023

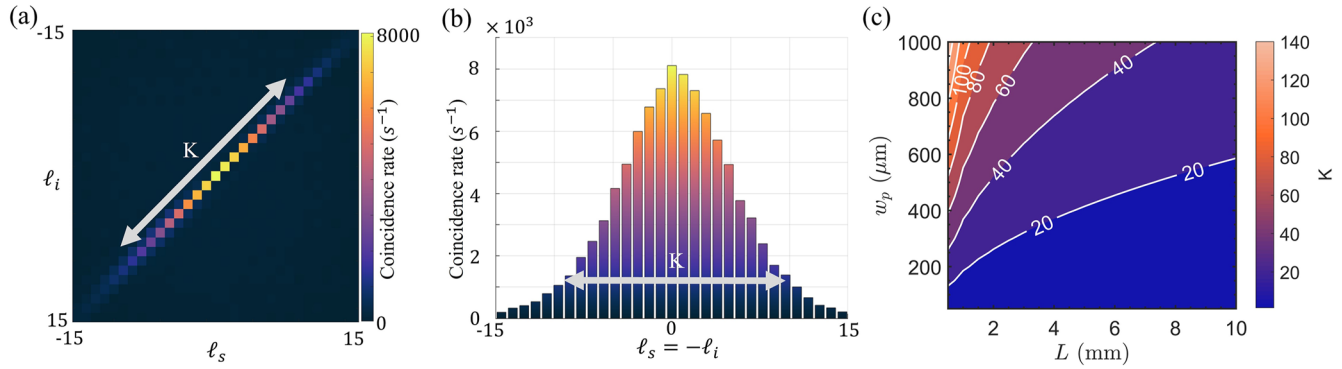


FIG. 10. SPDC generational OAM bandwidth. Example of measured (a) SPDC OAM coincidence rate (counts per second) for different OAM projections on the signal (ℓ_s) and idler (ℓ_i) photons, showing anti-correlations in OAM. (b) Coincidences taken for $\ell_s = -\ell_i$. From this plot, the spiral bandwidth (dimensionality), $K = 21$, was measured. (c) Spiral bandwidth optimization as a function of the pump beam waist size w_p and the non-linear crystal length L computed from K_{eff} in Eq. (34).

p, of the LG modes is possible,[30,114] but this is not covered here. Subsequent decomposition yields the analytical expression,[114]

$$c_\ell = \frac{4\alpha}{(1+\alpha)^2}\left|\frac{\alpha-1}{\alpha+1}\right|^{|\ell|}, \tag{32}$$

with $\alpha = w_p\sqrt{\frac{L}{k_p}}$ for pump wavenumber, k_p. The probability ($|c_\ell|^2$) of having the SPDC biphotons in the state $|\ell_s\rangle_s|-\ell_i\rangle_i$ can be calculated for the pump size and crystal length to give a generational bandwidth. For the results shown in Fig. 10(b), the parameters are $L = 5$ mm, $\lambda = 532$ nm, and $w_p = 400$ μm. Using the Schmidt number, $K = \frac{[\sum_\ell |c_\ell|^2]^2}{\sum_\ell |c_\ell|^4}$, as defined in Eq. (14), the number of modes present and, therefore, the dimensionality can be indicated. Moreover, the Schmidt number quantifies the (spiral) bandwidth of the OAM spectrum shared by the two photons.[71] Here, this value is marked on the bandwidth plot where $K \approx 21$. Assuming a symmetric spectrum about $\ell = 0$, one may thus convert K to the range of OAM available ($-\ell_{\max}$ to $\ell_{\max}$) by $|\ell|_{\max} = \frac{K-1}{2}$. Consequently, the effect of the pump size and crystal length on the generated dimensions (dictated by K) in the biphotons can be seen. Figure 10(c) shows how this varies for the ranges $L = [0.5 : 10]$ mm and $w_p = [50 : 1000]$ μm. It follows here that a shorter crystal length and a larger pump beam size generate a larger number of modes in the SPDC being produced. Now we are left with optimizing the detection system.

While the phase flattening measurement techniques we established earlier work as a highly sensitive single photon detection system, the nature of the SMF results in an additional modal modulation with the Gaussian distribution describing the coupling of the flattened light into the fiber.[71,105] As a result, the measured bandwidth needs to account for the SPDC state and the overlap thereof with both of the chosen detection modes for either photon.

One may understand the play between the generation and detection parameters by considering the geometric picture as outlined in Ref. 71, where the overlaps in the near and far-field regimes are accounted for. From this, an upper bound on the generated spiral bandwidth is derived,

$$K_{gen} = 1 + 2\sqrt{\frac{\pi^2 w_p^2}{L\lambda}}, \tag{33}$$

given the pump waist, wavelength, and crystal length. This result can be obtained by computing Eq. (14) for the OAM basis, given the crystal and pump photon parameters. To incorporate the detection beam waists, further derivation results in a convolution of near and far-field bandwidths, where[71]

$$K_{eff} = \left(\sqrt{\left(1+4\gamma_{s,i}^2\right)^{-2} + \left(1+\frac{\pi^2 w_p^2}{\gamma_{s,i}^2 L\lambda}\right)^{-2}}\right)^{-1}, \tag{34}$$

which allows one to predict the effective dimensionality of the modes that one may detect, given a choice of the detection waist size $w_{s,i}$ backprojected to the crystal plane in the ratio $\gamma_{s,i} = \frac{w_p}{w_{s,i}}$.

In Fig. 11(a) we illustrate the effect on chosen detection size by showing the variation of K_{eff} with $w_{s,i}$ and w_p as shown for the example used in Fig. 10(a). Consequently, an optimal ratio exists, as highlighted by a dotted line in the contour map. Furthermore, such an optimal value changes with the crystal length, as shown by the shift of the maximal positions of K_{eff} in Fig. 11(b), where $L = 1$ mm instead. The ratio thus depends on L as well as the pump waist. Here, this can be seen in Ref. 71.

$$\gamma_{opt} \approx \sqrt[4]{\frac{\pi^2 w_p^2}{\lambda L}}, \tag{35}$$

which yields the optimal ratio for detection given the pump waist and crystal length.

F. Other special elements for generation and detection

Besides the modulation and projective measurement approaches that were discussed earlier, spatial modes can be created and measured using a variety of other techniques and tools. Here, we explore a few that are commonly used for quantum

11 June 2026 13:34:37

© Author(s) 2023

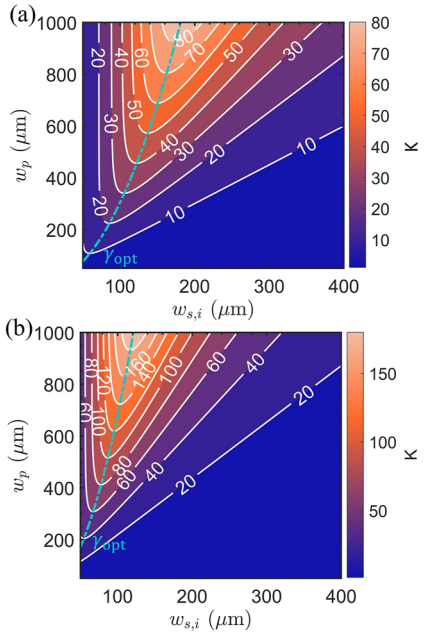


FIG. 11. SPDC measurable OAM bandwidth. Example of measurable bandwidth ($K \equiv K_{eff}$) as a function of the pump and detection beam sizes for a (a) L = 5 mm crystal and a (b) L = 1 mm crystal. The dotted line indicates the optimal ratio for maximum bandwidth between the detection and signal beam waists.

structured light. We focus on components that couple the polarization and spatial components of photons since they have been instrumental in demonstrating quantum walks,[115] quantum cryptography,[21] and creating hybrid entangled states.[116] Furthermore, we also explore the use of refractive elements for mode sorting since they show the capability of measuring high dimensional quantum structured light.[117–120]

1. Dynamic and geometric phase control of photons

In an effort to gain control over and manipulate the spatial structures of photons, significant efforts have been made toward developing additional elements in addition to the vanilla spatial light modulators. This, in an effort to allow specialized control in the manipulation and subsequent use of quantum light, further extends the toolbox for high dimensional applications. Here we consider three significant devices based on OAM, which, since their demonstration, have facilitated interesting applications for using structured quantum light and hold further potential.

Previously, the principles and implementation of a spatial light modulator could be seen to yield a versatile method for detecting (and generating) spatial structures on demand. A commonly used spatial light modulator is based on liquid crystal on silicon technology.[121] Here, each pixel of thickness Δt of the device is filled with liquid crystals that can be rotated by an applied voltage. The variation of the liquid crystal molecular orientations allowed one to impart a controlled dynamic phase, ϕ_d,

$$\phi_d = \frac{2\pi n \Delta t}{\lambda}, \tag{36}$$

through the altered refractive index, n, changing as a function of the liquid crystal orientation, a type of birefringence, and so only the phase of one polarization component is changed.

An alternative principle also lends itself to the generation of phases, but instead by using the "memory" of the transformations applied. Here, by altering parameters adiabatically in a closed-loop fashion, a geometric phase[122] may be induced, so-called as the amount of imparted phase is determined by half the solid area bounded by the transformations in the parameter space. Applied to light, one may use a change in polarization to induce such a relative phase in the electric field, as illustrated in Fig. 12(a), which is otherwise known as the Pancharatnam–Berry phase (after the authors), applying the concept to the classical[123,124] and quantum[125] light, respectively.

To see this effect, we may consider the polarization parameter space, which is illustrated on the polarization equivalent of the Bloch sphere in Fig. 12(b), known as a Poincaré sphere. Here, linear polarizations are placed along the equator and circular polarizations at the poles. The "closed loop" evolution of an input photon or light beam can then be followed by placing a series of waveplates, as illustrated in (a). When diagonally polarized light is passed through a half-waveplate (HWP) orientated at 22.5°, it becomes horizontally polarized. On the Poincare sphere (b), this is seen by the change in position from $|D\rangle$ to $|H\rangle$ through path A. Passing the light through a quarter-waveplate (QWP) at 45° then alters the state to $|R\rangle$, i.e., following path B and with another QWP at 90°, the $|R\rangle$ state is changed back to $|D\rangle$ through following path C and a closed loop has been formed on the Poincare sphere. The light at this stage is not just diagonally polarized but also has a supplementary phase of $\phi_G = e^{i\Omega/2}$, where Ω is the area enclosed by the evolution.

We may now consider applying this physical principle from the time (a) to the spatial[126] (c) domain. Here, instead of evolution

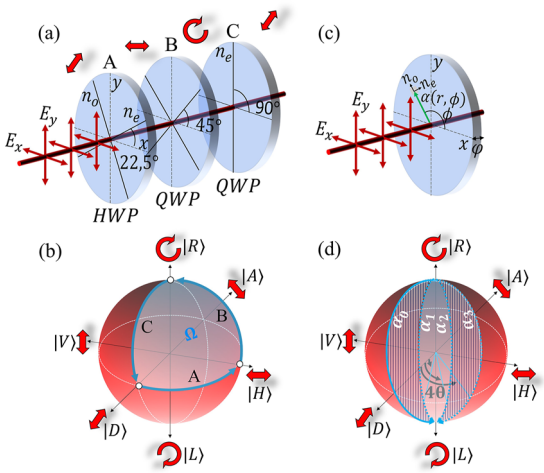


FIG. 12. The concept of geometric phase. (a) Illustration of a diagonally polarized state traversing a series of waveplates that take the state through a closed loop transformation, which is (b) depicted on the Poincaré sphere. (c) Depiction of an element with spatially varying optical indices of refraction that may be considered a series of HWPs with varying optical axes. (d) Illustration of associated paths taken by different rays of a light beam traversing an element with four arbitrary HWPs with varying fast axis rotational angles.

11 June 2026 13:34:37

© Author(s) 2023

through waveplates in time, we consider evolving small waveplate elements $[\alpha(r,\phi)]$ across the transverse spatial coordinates, (r,ϕ), of an optic as depicted in (c). Here, if a change in polarization occurs at points across the transverse spatial plane of the incoming beam, an associated spatially varying geometric phase is also generated. This is illustrated in (d), showing how geometric phase may be mapped between right-circularly polarized (RCP) waves traversing four arbitrary points [denoted $\alpha_0(r,\phi)$ to $\alpha_3(r,\phi)$] on an optic (c), which has effective HWP elements with different orientations at each transverse coordinate. With the polarization change occurring spatially, the "closed path" is formed by the difference in the path between the other elements, resulting in the geometric phase being both relative and spatially varying.[126,127] One may, therefore, engineer the relative optical axis orientations to generate any number of variable geometric phase acquisitions that may be used to manipulate the spatial mode of the overall beam.

The q-plate (QP) is one such device that does this[128] by patterning the optical axis orientation such that the relative phase changes azimuthally and thus creates an azimuthal phase across the entire beam.[128] The waves subsequently twist alongside each other in a helical fashion, resulting in OAM generation. This patterning of the optical axis is described by Eq. (37),[128]

$$\alpha(r,\phi) = q\phi + \alpha_o. \tag{37}$$

Here the QP is taken to be in the xy-plane, α_o is the angle formed by the optical axis from the x-axis, q is a constant defining the number of times the optical axis rotates in a path as it traverses once around the plate center, and α_o is the permanent offset of the optical axis from the element's x axis. A discontinuity occurring at $r = 0$ when $q \neq 0$ is evident due to the nature of the azimuthal coordinate, ϕ, being undefined at this point.

A simple description of the subsequent QP action can be performed in terms of a Jones matrix on the linear basis,[129]

$$QP = \cos\left(\frac{\varphi}{2}\right)\begin{bmatrix}1 & 0\\ 0 & 1\end{bmatrix} + i\,\sin\left(\frac{\varphi}{2}\right) \times \begin{bmatrix}\cos(2\alpha(r,\phi)) & \sin(2\alpha(r,\phi))\\ \sin(2\alpha(r,\phi)) & -\cos(2\alpha(r,\phi))\end{bmatrix}. \tag{38}$$

Here, ϕ refers to the efficiency of QP, which is tied to the retardance of the slow and fast axes in the element. The cosine term alongside the identity matrix indicates that this portion of the incident beam remains unaffected where no polarization or phase changes occur. The second matrix term refers to the action of the QP whereby an azimuthally-varying geometric phase is imparted as described by Eq. (37). It may thus be seen that when $\varphi = \pi$ (HWP retardance), the QP is 100% efficient, with the first matrix term falling away.[129,130] Q-plates meeting this condition are referred to as "tuned."

Consequently, the QP operation may be condensed into the following selection rules:[129]

$$\hat{QP}|l,R\rangle = \cos\left(\frac{\varphi}{2}\right)|l,R\rangle + \sin\left(\frac{\varphi}{2}\right)|l+2q,L\rangle, \tag{39a}$$

$$\hat{QP}|l,L\rangle = \cos\left(\frac{\varphi}{2}\right)|l,L\rangle + \sin\left(\frac{\varphi}{2}\right)|l-2q,R\rangle. \tag{39b}$$

This effective twisting of the light beam produced by the geometric phase has additional implications in the physical interpretation, whereby the CP polarization may also be seen in terms of spin angular momentum (SAM). Here, when RCP is incident on the QP, an OAM of $2q\hbar$ per photon is generated, and the flip in CP corresponds to a flip in SAM from $1\hbar$ per photon to $-1\hbar$. It is well known that the transference of SAM and OAM can occur between light and certain matter.[130] Here, SAM interaction occurs in optically anisotropic media such as birefringent material and OAM in transparent inhomogeneous, isotropic media.[128] The combination of a thin birefringent (liquid crystal) plate with an inhomogeneous optical axis in the QP subsequently results in the element coupling these two forms of angular momentum such that flipping in the SAM may be seen to generate OAM, making the QP a spin-to-orbital angular momentum converter (STOC) where the symmetry of the optical axis patterning effects the conversion values.[130]

QPs have been instrumental in realizing practical applications of quantum structured light that interface the spin and orbital components of photons for quantum communication in free-space,[21,131,132] underwater,[133] between satellites,[134] and through optical fiber,[135,136] for quantum memories,[132] computing,[115,137–139] quantum metrology,[140] and for engineering novel quantum entangled states such as entangled vectorial fields,[141] hybrid entangled,[116,142,143] and hyper-entangled[144,145] quantum channels. In most of these applications, the QP is used as the main component for encoding quantum information in quantum structured light.

While useful, the QP is limited by the physical principles governing geometric phase only, reducing the operation on opposite polarizations to yield conjugate OAM charges of each other only and requires the principle evolution to remain on a CP basis. An alternative approach uses the properties of meta-surfaces[146,147] instead of liquid crystals. Here, the desired phases are achieved by spatially engineering the characteristics of sub-wavelength structures, known as meta-atoms. This is usually achieved by altering the orientation and dimensions of the meta-atom structures. Metasurfaces can subsequently replicate the action of the QP[148–151] but can then be extended to have more control, enabling the controlled pairing of both geometric and propagation phases, such that arbitrary polarization states can be mapped to arbitrary increments of OAM[152,153] or even superpositions thereof.[150,154] For instance, one may engineer the interaction such that a generalized conversion of[152]

$$JP = e^{i\delta}\begin{bmatrix} e^{i\delta}(e^{im\phi}\cos^2\chi + e^{in\phi}\sin^2\chi) & \frac{\sin 2\chi}{2}(e^{im\phi} - e^{in\phi}) \\ \frac{\sin 2\chi}{2}(e^{im\phi} - e^{in\phi}) & e^{-i\delta}(e^{im\phi}\sin^2\chi + e^{in\phi}\cos^2\chi)\end{bmatrix}, \tag{40}$$

is possible for arbitrary linear polarization bases states, $|s^+\rangle = \left[\cos(\chi); e^{i\delta}\sin(\chi)\right]^T$ and $|s^-\rangle = \left[-\sin(\chi); e^{i\delta}\cos(\chi)\right]^T$. Here, ϕ remains the azimuthal angle, and n and m are integers, with χ and δ being parameters dictating the polarization states. It then follows that the operations

$$\hat{JP}|\ell,s^+\rangle = |\ell+m,(s^+)^*\rangle, \tag{41a}$$

11 June 2026 13:34:37

© Author(s) 2023

$$\hat{J}P|\ell, s^-\rangle = |\ell + n, (s^-)^*\rangle, \tag{41b}$$

take place where * specifies complex conjugate and $e^{im\phi} = |m\rangle$ ($e^{in\phi} = |n\rangle$) is the phase with m (n) OAM imparted to the polarization state $|s^+\rangle$ ($|s^-\rangle$).

These devices thus allow one to arbitrarily map between polarizations and orbital angular momentum, allowing one full control of the full angular momentum (J) domain and, as such, have been denoted J-Plates. Furthermore, the versatility of engineering the material properties allows one to extend past the OAM domain and map polarization to the pixels domain (images) such that one polarization excites an image like a cat and the other a dog,[155] or, conversely, different OAM states exciting different holographic images,[156,157] and the HWP dependence changed to that of a QWP[158] and structuring the total angular momentum as it propagates.[159] Good reviews tracking the burgeoning progress of these and other metasurface-based devices can be found in Refs. 146 and 160. With such capabilities, these metasurface devices have also found possibilities in quantum applications. A good review considering this is Ref. 161, where applications ranging from state creation to manipulation and weak measurements are considered.

2. Refractive mode sorters

Therefore, we have explored detection by the single generation of conjugate projections in order to detect OAM. Alternatively, the application of geometric transformation concepts such as coordinate transformations through the use of optical systems can exact a desired transformation in light.[162] This is the basic principle behind mode sorting and, therefore, detecting OAM. Here, the technique takes advantage of the circular geometry associated with OAM so that a geometrical mapping translates circular to rectangular geometry,[163] as illustrated in Fig. 13(a). The resultant phase distribution "unwrapping" causes OAM to be transformed into transverse momentum with a linear phase gradient,[120] as demonstrated in the (u, v) coordinate space of the figure.

Physically, this $(x, y) \rightarrow (u, v)$ transformation is achievable through the application of a phase distribution, described in Eq. (42),[163]

$$\varphi_1(x, y) = \frac{d}{\lambda f}\left[y \tan^{-1}\left(\frac{y}{x}\right) - x \ln\left(\frac{\sqrt{x^2 + y^2}}{b}\right) + x\right]. \tag{42}$$

Here d is the fixed unwrapped beam length, b affects the location in the (u, v) plane, λ is the wavelength, and f is the transforming lens focal length. Associated phase distortions in the "unwrapped" beam from optical path length variation then simply require correction by a second phase distribution, described in Eq. (43),[118,163]

$$\varphi_2(u, v) = \frac{db}{\lambda f} e^{\frac{-2\pi u}{d}} \cos\left(\frac{2\pi v}{d}\right). \tag{43}$$

The resultant phase distribution "unwrapping" causes the OAM to become transverse momentum with a now linear phase gradient of $e^{il \tan^{-1}(\frac{y}{x})} = e^{il\frac{2\pi v}{d}}$ across the beam length.[118,119] As the

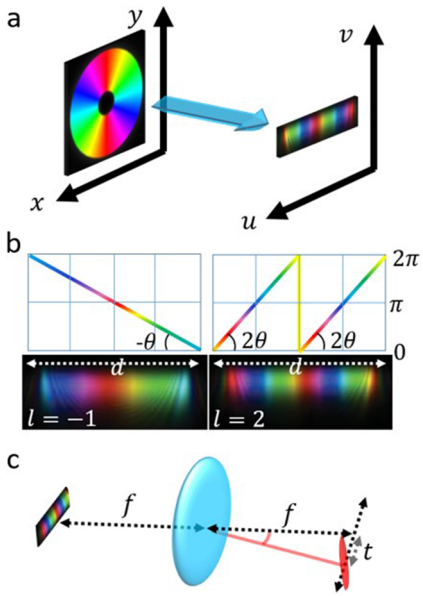


FIG. 13. Mode sorting with geometrical phase transformation. The (a) illustration of a conformal mapping that "unwraps" an OAM = 2 mode to a transverse phase gradient and the (b) color map illustration of the phase gradient resulting from the OAM geometric transformation for $l = -1$ (left) and $l = 2$ (right). (c) Depiction of the sorting action performed by a Fourier transforming lens after the phase correction element.

"unwrapped" mode contains a phase gradient limited to the length, d, all OAM modes result in a transverse phase gradient that is integer multiples of each other, as shown in Fig. 13(b).

Physically distinguishing the unraveled gradient then requires a phase-to-position mapping. Here, the Fourier transforming operation of a lens comes into play such that each unwrapped beam forms a diffraction-limited elongated spot at the Fourier plane.[120] Furthermore, the phase gradient dictates the transverse position of the spot (t) here. It thus follows that after a lens, the mode sorter maps OAM to a particular transverse position[163] according to

$$t = \frac{\lambda f l}{d}, \tag{44}$$

and as illustrated in Fig. 13(c).

Moreover, the intensity of the spot indicates the "amount" of any OAM mode present. The mode sorter technique employed with refractive elements allows for the efficient detection of a large range of OAM modes and the associated weightings, enabling the detection of low intensity sources in comparison to other techniques such as SLM projections. For instance, sorting as many as 50 states was demonstrated.[119]

It may be noted that, as a result of the transformative action, such devices are more sensitive to alignment than devices such as SLMs or QPs. They do, however, offer the advantage of deterministic detection, as the transformation always sends the photons to a detectable state. This is in contrast to single-outcome projective measurements such as those performed by the SLM, where the pho-

11 June 2026 13:34:37

© Author(s) 2023

tons that do not collapse into the mode the SLM is interrogating for are discarded, making the detection probabilistic. Accordingly, this detection has been used from detecting vector vortex states deterministically[117] to high-dimensional quantum cryptography,[36] efficient detection for a classical quantum walk resonator,[139] and interfacing between the path and OAM entanglement.[164]

Finally, we note that there is a wide range of specialized optics and extensions thereof, such as g-plates, proceeding from liquid crystal patterning like QPs to allow for topological quantum simulations[165] and linear photonic gears.[166] Mode sorters have been extended to include radial orders[167] and other spatial modes such as Hermite–Gaussian modes[168] and have taken on more complex forms with multiple conversion planes[169] even extending into fibers.[170] Metasurfaces, furthermore, have a very wide reach from multi-wavelength lenses[171–173] to nonlinear engineering.[174–176] Here, we selected a few special optical elements that have made a basic impact on structured quantum light.

V. HIGH DIMENSIONAL STATE CHARACTERIZATION

We have introduced a source for creating quantum structured light (i.e., SPDC) and also presented several measurement apparatuses and detection techniques. Next, we focus on a few examples of typical characterization techniques, particularly those that are used for verifying two dimensional and higher dimensional quantum entanglement, and also discuss a method for reconstructing quantum states. The photons analyzed in this section were also produced from SPDC (see Sec. IV A 2) and are entangled in their OAM degrees of freedom. Because the pump photons used here had a topological charge of $\ell = 0$, according to Eq. (23), the photon pairs are prepared in the state,

$$|\Psi_{AB}\rangle = \sum_{\ell} c_{\ell} |\ell\rangle_A |-\ell\rangle_A, \tag{45}$$

where c_ℓ are normalized coefficients. The task here is to use the techniques we will discuss to characterize such states.

A. 2D Bell curves and Bell violations

In most quantum entanglement experiments, it is common practice to demonstrate a violation of the Clauser-Horne-Shimony-Holt (CHSH) Bell inequality.[177] The violation of the inequality confirms non-locality in quantum experiments. Following the initial demonstration with the polarization states of photons,[44] today the Bell-inequality violation is used in a myriad of experiments as a characterization tool. Here we show how it can be performed on an OAM basis. We direct the reader to Refs. 24 and 23 for further reading.

As shown in Fig. 14(a), spatially separated measurements are performed on entangled photons A and B that are generated from a nonlinear crystal (NC). The photons share an entangled state given by $\frac{1}{\sqrt{2}}(|\ell\rangle_A|-\ell\rangle_B + |-\ell\rangle_A|\ell\rangle_B)$ for integers ℓ, defined in the OAM basis. Photons A and B are projected onto superposition states of OAM with equal but opposite charges,[178]

$$|\theta_{A(B)}\rangle = \frac{1}{\sqrt{2}}\left(|\ell\rangle + e^{i\ell\theta_{A(B)}}|-\ell\rangle\right), \tag{46}$$

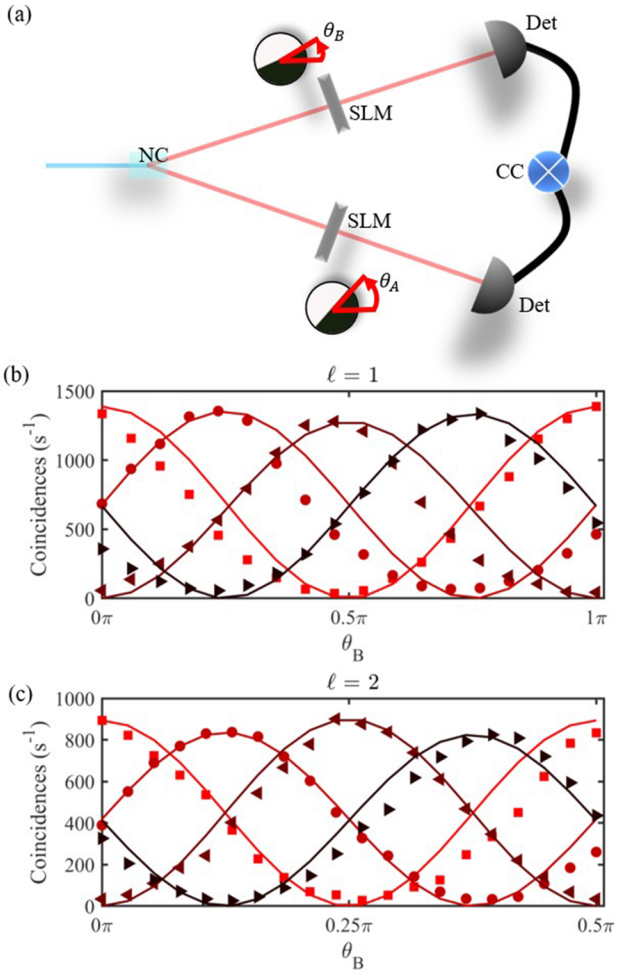


FIG. 14. Bell-inequality violation. (a) An experiment for demonstrating the Bell inequality violation using structured light. Here, SPDC photons are generated from nonlinear crystal (NC) and propagated to spatial light modulators (SLM), where spatial projections onto the states $|\theta_{A(B)}\rangle$ are performed. $\theta_{A(B)}$ corresponds to the physical rotation of the encoded hologram. Correlation measurements between photons A and B for the subspaces (b) $\ell = 1$ and (c) $\ell = 2$. Using these correlations, the Bell parameter can be evaluated.

where $\theta_{A(B)}$ controls the relative phases between the states in the superposition. Physically, the parameters $\theta_{A(B)}$ correspond to physical rotations of the phase patterns [see insets for Fig. 14(a)]. Detection probabilities are shown in Figs. 14(b) and 14(c) for $\ell = \pm 1, 2$, respectively. In each plot, the coincidence measurements between photons A and B are shown for $\theta_A = \{0, \frac{\pi}{2\ell}, \frac{\pi}{\ell}, \frac{3\pi}{2\ell}\}$, mapping the projections of photon A, while for photon B they are varied between 0 and $\frac{\pi}{\ell}$, where the probabilities are proportional to $\cos^2(\ell(\theta_A - \theta_B))$. Subsequently, the CHSH-Bell parameter S can be computed from[178]

$$S = \left|E(\theta_A, \theta_B) - E(\theta_A, \theta'_B) + E(\theta'_A, \theta_B) + E(\theta'_A, \theta'_B)\right|, \tag{47}$$

with $E(\theta_A, \theta_B)$ calculated from the coincidence events,

11 June 2026 13:34:37

© Author(s) 2023

$$E(\theta_A,\theta_B) = \frac{\xi(\theta_A,\theta_B) - \xi'(\theta_A,\theta_B)}{\xi(\theta_A,\theta_B) + \xi'(\theta_A,\theta_B)},$$
$$\xi(\theta_A,\theta_B) = C(\theta_A,\theta_B) + C\left(\theta_A + \frac{\pi}{2}, \theta_B + \frac{\pi}{2}\right), \quad (48)$$
$$\xi'(\theta_A,\theta_B) = C\left(\theta_A + \frac{\pi}{2}, \theta_B\right) + C\left(\theta_A, \theta_B + \frac{\pi}{2}\right).$$

Here, $C(\theta_A,\theta_B)$ represents measured coincidence counts. The Bell parameter can be characterized as $S \le 2$ for separable states (satisfying local hidden variable theories) and $2 < S \le 2\sqrt{2}$ for nonlocal entangled states. The upper bound of the Bell parameter, $S = 2\sqrt{2}$, is called the Tsirelson bound,[179] which is achieved only for maximally entangled Bell states. For the two measurements in Figs. 14(b) and 14(c), we obtained Bell parameters of $S_1 = 2.66 \pm 0.08$ and $S_2 = 2.80 \pm 0.01$ violating the Bell inequality and confirming entanglement in the $\ell = \pm 1$ and $\ell = \pm 2$ subspaces of our generated SPDC photons.

While our demonstration above shows that the Bell-inequality test can be used to confirm entanglement in multiple subspaces of a high dimensional entangled state, it does not confirm the entanglement between all the subspaces. In order to confirm that a higher dimensional state possesses entanglement over all the dimensions, generalized Bell inequalities have to be employed. One such version was introduced by Collins *et al.*,[180] sometimes called the CGLMP inequality, and has been instrumental in demonstrating high dimensional Bell violations ranging from OAM qutrits[181,182] and reaching up to 12 dimensions[25] of entangled OAM states. Furthermore, an intriguing aspect of the CGLMP inequality is that higher dimensional states can obtain violations above the Tsirelson bound.

B. Quantum state tomography

The concept of tomography relies on the idea of projecting a quantum state onto observable basis states and measuring the probability that the particle is in the state. One then works backward in order to determine what state would result in the outcomes measured. Tutorial references covering this topic may be found in Refs. 23 and 183 with a more brief overview tailored to this work detailed here. The concept is illustrated in Fig. 15(a). Here the projective measurements equate to using a light source to project the shadow of the object of interest onto a plane such as those normal to the x-, y-, and z-axes shown in the top panel of Fig. 15(a). The shapes and dimensions of the projected profiles then allow one to

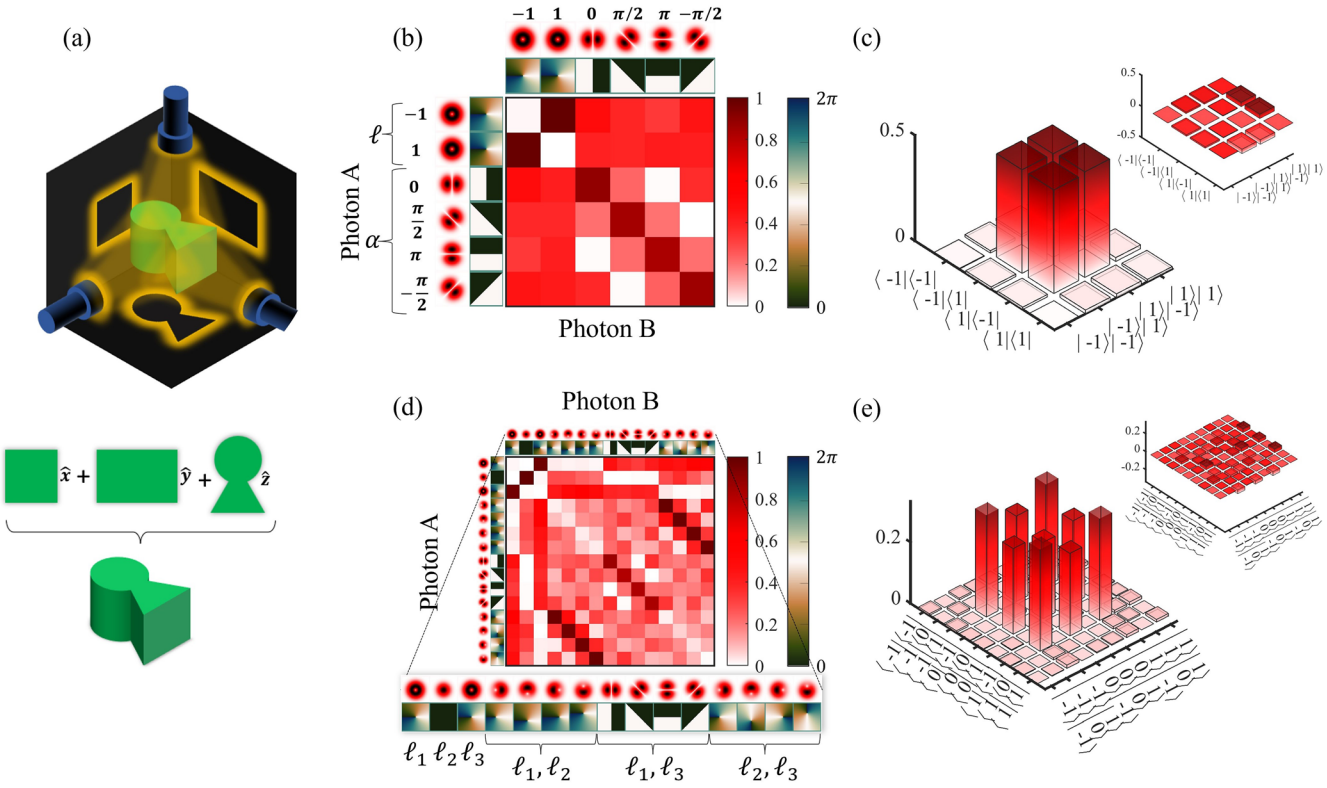


FIG. 15. State reconstruction. (a) Concept of quantum state tomography, where projections are made into states ("planes") that reveal the composition of the state ("shape"). The projections can be subsequently combined to reproduce the state. Qubit state ($d = 2$), (b) tomographic projections onto the $\ell = \pm 1$ subspace, and corresponding (c) reconstructed state. For two particle qubits, up to 36 measurements are performed. In higher dimensions, more projections are needed. (d) Tomography of a $d = 3$ entangled state where the projections are performed on smaller qubit spaces at a time. (e) Corresponding reconstructed density matrix for the qutrit entangled state.

11 June 2026 13:34:37

© Author(s) 2023

reconstruct what the object was as indicated in the bottom panel of Fig. 15(a). It should be noted that here only 3 projective measurements were used, which assumes a fairly simple and symmetric object. For more complex objects or measurements that introduce uncertainties, a larger number of projections onto different sets of planes can allow for a more accurate reconstruction.

Quantum mechanically, we can carry out this reconstructive concept by performing various operations in order to manipulate the state and thus characterize it. To do so, we apply a variety of projections on many copies of the quantum system, and with the subsequent measurements, information on the quantum state being interrogated is built up, analogous to the projections of the object shown in Fig. 15(a). The question now arises: what are the optimal projections necessary in order to accurately determine the quantum state?

Several types of approaches to such tomographic measurements have been put forward that allow one to extract the information needed to reconstruct the state. Here, these range from generalized Bell tests[25,181,182] to using mutually unbiased bases[26,28,184] or incorporating self-guided approaches,[185,186] with each approach having certain merits. One may also ask, how many measurements are enough to accurately reconstruct the state using the chosen method? The answer to this lies in the uncertainties in the measurements being made. Initially, one may consider the projections in the concept figure. Here, only three projective measurements are actually necessary in order to find the object. These would then form a tomographically complete set. If there is any uncertainty or "blurriness" in the projection, the actual size and perhaps the fine structural details of the outlines may be in question. To improve this, one may consider making additional projections on the object where the planes are rotated to some degree. While these projections may not provide additional information, they will allow the reconstructed object to be checked against them and adjusted as necessary. This results in the "blurriness" or uncertainty being reduced. This then forms an overcomplete set of measurements but allows a greater degree of accuracy in the reconstruction.[187,188]

Before we begin, it is important to highlight that we first have to assume a decomposition of the density matrix. For two dimensions, we assume that the state density matrix is given by[26]

$$\rho = \sum_{m,n=0}^{3} b_{mn}\sigma_{A,m} \otimes \sigma_{B,n}, \tag{49}$$

where $\sigma_0 = \mathbb{I}_2$ is the identity matrix and $b_{00} = 1/4$, and the other coefficients $b_{m,n>0}$, weight the tensor products between the Pauli matrices, $\sigma_{A(B),m>0}$, given by

$$\sigma_1 = \begin{pmatrix} 0 & 1 \\ 1 & 0 \end{pmatrix}, \tag{50}$$

$$\sigma_2 = \begin{pmatrix} 0 & -i \\ i & 0 \end{pmatrix}, \tag{51}$$

$$\sigma_3 = \begin{pmatrix} 1 & 0 \\ 0 & -1 \end{pmatrix}, \tag{52}$$

that span the two-dimensional states pace of each photon. Therefore, the measurements we perform must return information about the coefficients that determine the state. Since each Pauli matrix can be decomposed into two projectors, $\sigma_m = P_m^+ - P_m^-$, we can construct our measurements by projecting onto these states, i.e., $P_m^\pm = |\lambda_m^\pm\rangle\langle\lambda_m^\pm|$, where $|\lambda_m^\pm\rangle$ are the corresponding states.

In the OAM basis, we can select the two states $|\ell_1\rangle$ and $|\ell_2\rangle$ as our standard basis, constituting the eigenstates of the σ_3 matrix. Next, we can construct their equally weighted superposition,[26]

$$|\alpha_{\ell_1\ell_2}\rangle = \frac{1}{\sqrt{2}}\left(|\ell_1\rangle + e^{i\alpha}|\ell_2\rangle\right), \tag{53}$$

with relative phases α. By selecting $\alpha = 0, \pi$, and $\alpha = \frac{\pm\pi}{2}$, we obtain eigenstates of the σ_1 and σ_2 operators, respectively. Therefore, we have a total of six projectors, $P_j \to |j\rangle \in \{|\ell_1\rangle, |\ell_2\rangle, |\alpha = 0\rangle, |\alpha = \pi\rangle, |\alpha = \pm\pi/2\rangle\}$, that form a tomographically complete set of measurements for each photon (see Ref. 23).

In Fig. 15(b), we show the measurements performed on two photons given the tomography measurement states above. Here, spatially separated measurements $A_{ij} = P_i^A \otimes P_j^B$ were performed, where $P_{i,j}^{A,B}$ are the local projections of photon A and photon B in our overcomplete basis. The detection probabilities of a system with a corresponding density matrix (ρ) are thus

$$M_{ij} = \mathrm{Tr}\left(A_{ij}\rho(A_{ij})^\dagger\right), \tag{54}$$

where $\mathrm{Tr}(\cdot)$ represents the trace operation. These measurements, M_{ij}, can then be used to reconstruct the density matrix. Two popular methods for achieving this are maximum likelihood[189–191] and Bayesian mean[192–194] estimation. In this work, we employed maximum likelihood, where the coefficients b_{mn} were determined by minimizing the square difference between the measured and theoretical probabilities.[195] Once successful, the real and imaginary parts can be obtained, as shown in Fig. 15(c). The imaginary part of the density matrix is placed as an inset.

The aforementioned method can be extended to higher dimensions ($d > 2$) by taking the higher dimensional state and projecting it onto smaller qubit spaces.[26] The localized measurements for each particle are then spread across combinations of two-dimensional subspaces within the d-dimensional system. This naturally results in far more measurements as each two-dimensional subspace combination in the d-dimensions of each particle needs to be measured along with all the different MUBs therein. In Fig. 15(d), we show the measurements for $|\ell_j\rangle \in \{|-1\rangle, |0\rangle, |1\rangle\}$ basis states, where projections are performed on the OAM eigenstates, as well as the corresponding superpositions, $|\alpha_{\ell_1\ell_2}\rangle$, with the $\ell_1 < \ell_2$. As such, the number of measurements scale as $(4\mathcal{C}_2^d + d)^2$ with d dimensions per particle for a two-particle system, where $\mathcal{C}_2^d$ is a binomial coefficient.

Unlike the qubit case, where we used the decomposition in Eq. (49), for qudits, we apply a generalized version of the density matrix for higher dimensions following:[26]

$$\rho = \sum_{m,n=0} t_{mn}\tau_{A,m} \otimes \tau_{B,n}, \tag{55}$$

where the coefficients t_{mn} are weighting factors for the generalized Gell–Mann matrices, τ_m, for $d > 2$. Here, τ_0 is the identity matrix,

11 June 2026 13:34:37

© Author(s) 2023

and $t_{00} = 1/d^2$, given that each photon is defined on a d-dimensional statespace. Given this decomposition, we can apply maximum likelihood using the tomography measurements. We show the reconstructed density matrix for the $d = 3$ entangled state in Fig. 15(e) using this model.

The techniques described earlier make use of measured detection probabilities to work out what state could have produced them. However, the measurements performed were not high dimensional and were instead constructed from simple two dimensional MUB subspaces. It is possible to use higher dimensional state projections that project onto the d-dimensional space of each photon.[196] Given our d-dimensional standard basis of OAM modes, i.e., $|\psi_j^0\rangle \in \{|\ell_j\rangle, \quad j = 0, 1..d-1\}$, it is possible to find d MUBs, forming an overcomplete set on the d-dimensional state space. The main limitation is that not all the MUBs can be found for arbitrary d, except when d is an odd prime number or an integer power of a prime.[197] Assuming that the d is an odd prime number, then the nth state from the mth MUB can be written as an equally weighted superposition following[197]

$$|\psi_n^m\rangle = \frac{1}{\sqrt{d}} \sum_{k=0}^{d-1} \omega^{kn} \omega^{mk(k-1)/2} |\ell_n\rangle, \tag{56}$$

where $m = 1, 2, \ldots, d-1$, $n = 0, 1, \ldots, d-1$, and $\omega = \exp(i2\pi/d)$. Once all (d + 1) bases are obtained then joint projections of photon A and B onto each of the basis states, including the standard basis $|\psi_j^0\rangle$, are performed, resulting in a total of $((d+1)d)^2$ because there are $d+1$ MUBs each containing up to d independent states. Finally, the measured results are then used to find the density matrix using maximum-likelihood just with the qubit state projections. In Ref. 184, it was reported that up to $2d+1$ measurements can be discarded, therefore leaving a total of d^4 measurements. For example, the authors show that for $d = 5$ dimensional entanglement, they only require $N = 625$ measurements, which is much lower than the $N = 2025$ measurements that are required for projections onto multiple 2 dimensional Hilbert spaces.

C. Fidelity and purity

To characterize the quality of the generated states, we can use some of the measures that were introduced in Sec. III. For example, we can characterize how similar the measured density matrix is to our desired one by using the state fidelity in Eq. (12), but rewritten here as $F = \left(\mathrm{Tr}\left(\sqrt{\sqrt{\rho_T}\rho\sqrt{\rho_T}}\right)\right)^2$, where ρ is the measured density matrix and ρ_T is the target density matrix. The fidelity evaluates to 0 for distinct (non-equivalent) density matrices and 1 for identical density matrices. Here, the density matrices we reconstructed were compared to maximally entangled states in the same dimensions, i.e., $|1\rangle|-1\rangle + |-1\rangle|1\rangle$ for $d = 2$ and $|1\rangle|-1\rangle + |0\rangle|0\rangle + |-1\rangle|1\rangle$ for $d = 3$, corresponding to the density matrices in Figs. 15(c) and 15(d), respectively. The fidelity was measured as $f = 0.98 \pm 0.01$ and $f = 0.92 \pm 0.01$ for our $d = 2$ and $d = 3$ dimensional states, respectively, showing that the reconstructed states are similar to the maximally entangled states we desired.

Furthermore, the degree of the mixture in the states can be quantified from Eq. (15) via the linear entropy (S_L) or Von Neumann entropy. Accordingly, the purity of the state can be computed from $1 - S_L$, producing values equal to $1/d$ for mixed states and 1 for pure states. For our measured density matrices in Figs. 15(c) and 15(d), the linear entropies are $S_L = 0.01 \pm 0.02$ and $S_L = 0.11 \pm 0.07$ for $d = 2$ and $d = 3$, respectively. The corresponding purities are thus $1 - S_L = 0.99 \pm 0.02$ and $1 - S_L = 0.89 \pm 0.07$, showing that the states are similar to maximally entangled states and possess a high level of purity.

D. Toward fast and efficient witness and quantum measures

In the techniques, we have presented so far, we chose the dimensions of the state we wanted to probe (in the case of the Bell measurement), or we needed to reconstruct the full density matrix (tomography) of the system in order to extract the purity or fidelity of the state. However, the state reconstruction can be a tedious process because the measurement complexity can scale to d^4 for quantum systems where each photon occupies d dimensions.

Recently, many alternative techniques have been developed to characterize high-dimensional quantum states, including approximating the density matrix via quantum state tomography techniques that incorporate self-guided approaches to state reconstruction,[185,186] or using a mutually unbiased basis to compute higher dimensional entanglement witnesses.[28] The witness's approach attempts to establish a lower bound on the fidelity of the quantum state by mapping the state onto a maximally entangled state with a Schmidt rank k. To see how the technique works, we first define the operational definition of the Schmidt rank,[28] where we find some positive integer k that satisfies

$$F(\rho, \Phi) \leq B_k(\Phi), \tag{57}$$

where ρ is a d dimensional density matrix for a two photon state, $|\Phi\rangle = \sum_{j=1}^{k} \gamma_j |j\rangle|j\rangle$, $F(\rho, \Phi) = \mathrm{Tr}(\rho * |\Phi\rangle\langle\Phi|)$ is the fidelity of the state with respect to a maximally entangled state and the parameter $B_k(\Phi) = \sum_j^k |\gamma_j|^2$. For a maximally entangled state, $B_k(\Phi) = k/d$. Therefore, one finds the lower bound of the Schmidt rank $k-1$ when $F(\rho, \Phi) > B_k(\Phi)$.[28,68] The authors in Ref. 28 demonstrated that one can obtain the Schmidt rank using at least two mutually unbiased bases and used it to characterize pixel entanglement in the above $d = 90$ dimensions.

In previous work,[131] we also introduced a method for characterizing the purity and dimensionality (effective dimensions and Schmidt rank) with $d/2$ measurements for noisy isotropic states in Eq. (11). The technique estimates the size of the Hilbert space of the photons (d) as well as the purity of the state p by performing a set of local projective measurements that return periodic detection probabilities with visibility that is dependent on the dimensions of the state. Because d and p are parameters that determine the isotropic state, the fidelity can also be estimated from p using

$$F_p = \frac{p(d^2-1)+1}{d^2}. \tag{58}$$

This means that for a state with an effective dimensionality of d, the Schmidt rank is given by $d_{ent} \approx dF_p$.[28] This procedure was used to characterize entanglement in a state defined in $d = 100$ dimensions.[27]

The benefit of having access to such measurement techniques is that key information needed for quantum information processing

11 June 2026 13:34:37

© Author(s) 2023

protocols, such as the information capacity of quantum states and the allowed error bounds in secure communication systems, can be estimated quickly without wasting resources and increasing measurement times.

VI. EXAMPLE APPLICATIONS

A. Quantum key distribution

1. High dimensional BB84 protocol

One of the emerging key applications of structured light is in the area of quantum key distribution (QKD). Protocols such as the BB84 (prepare and measure)[46] or the E91 (entanglement based)[198] protocols were designed to replace computationally difficult problems to maintain secrecy in communication channels. This is because the rise of quantum computing algorithms might compromise traditional key generation techniques that may rely on difficult problems such as factoring.[199] QKD is superior in that it is provably secure thanks to the uncertainty principle and no-cloning theorem,[200] making the QKD protocols robust against an eavesdropper that is armed with unlimited resources.

Here, we will mainly focus on the prepare measure protocol, where photons are encoded and transmitted by Alice and detected at the receiver by Bob. Following the implementation of these protocols with polarization qubits, it was later realized that polarized photons could only transport 1 bit of information and, therefore, more efforts were focused on generalizing the protocol to higher dimensions. Once the theoretical framework was in place,[66] adaptations of the protocol were implemented beyond qubit encoding using alternative degrees of freedom. Several experiments were reported[21,35,36,131] that made use of structured light patterns encoded with OAM. We will describe, in a tutorial style, how the prepare measure protocol is executed with quantum structured light.

Using the OAM basis, Alice and Bob can agree on a set of basis modes, $|\Psi_j\rangle \in \{|\ell_1\rangle, |\ell_2\rangle, \ldots, |\ell_d\rangle\}$, that have d independent states. Subsequently, they select a second set of basis modes $|\Phi_j\rangle$, that are mutually unbiased to the standard basis. The two bases must satisfy the relation $|\langle\Psi|\Phi\rangle|^2 = 1/d$. For a given d dimensional basis, there are at most $d+1$ mutually unbiased bases to choose from.[197]

For example, in three dimensions, we can use the basis modes $\{|\ell_1 = -1\rangle, |\ell_2 = 0\rangle, |\ell_3 = 1\rangle\}$. The corresponding mutually unbiased basis can be found in the equally weighted superposition states,

$$\left|\Phi_k\right\rangle = \frac{1}{\sqrt{d}} \sum_{j=1}^{d} a_{kj} \left|\Psi_j\right\rangle, \tag{59}$$

where weightings, a_{kj}, for each state can be found from the row vectors of the matrix

$$\begin{pmatrix} 1 & 1 & 1 \\ 1 & \omega & \omega^2 \\ 1 & \omega^2 & \omega \end{pmatrix}, \tag{60}$$

where $\omega = e^{i2\pi/d}$. There are two other matrices that can be used to form the MUB in $d = 3$ (see Ref. 35). We show the corresponding modes formed from our OAM superposition basis in Fig. 16(b) for the spatial basis of $\{|\Psi_j\rangle\}$ (top panel) and $\{|\Phi_j\rangle\}$ (bottom panel)

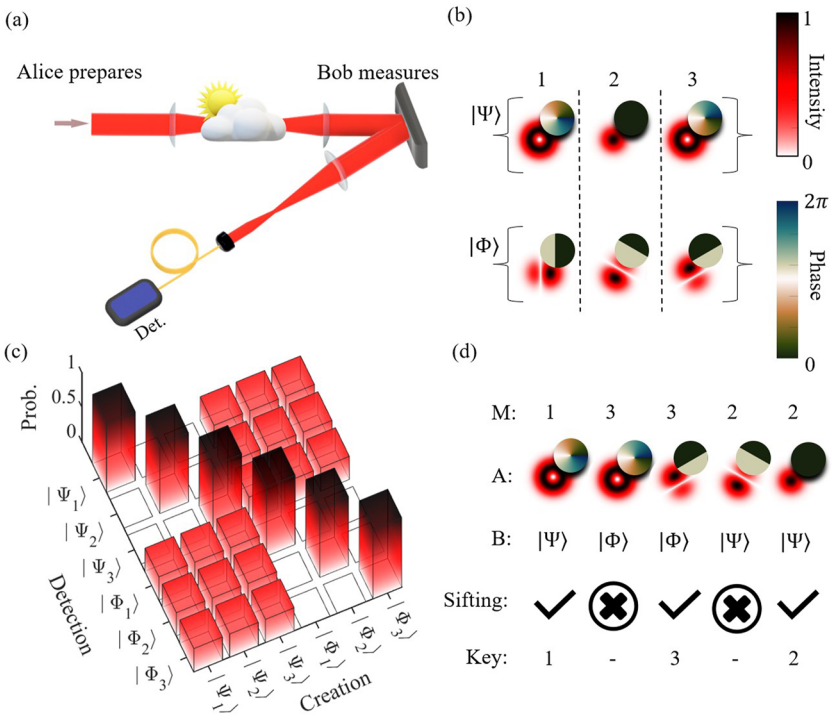


FIG. 16. Quantum key distribution with structured light. (a) Alice prepares a state on a randomly chosen basis, and Bob can measure the said state on a basis that he chooses randomly as well. (b) The states they choose must be selected from a pair of mutually unbiased bases $\{|\Psi\rangle_j\}$, $\{|\Phi\rangle_j\}$, which in this example, we have chosen to be comprised of orthogonal spatial states $|\Psi\rangle \in \{|-1\rangle, |0\rangle, |1\rangle\}$ and superposition states $|\Phi_k\rangle = \frac{1}{\sqrt{3}}\sum_{j=1}^{3} a_{kj}|\Psi_j\rangle$. (c) The overlap matrix shows orthogonality between states on each basis but the non-zero overlap between pairs of states taken from both bases. (d) The key generation scheme starts with Alice preparing a state on a randomly chosen basis and Bob performing a measurement on another randomly chosen basis. They then sift through all the measurements and discard all those in which the preparation and measurement bases were not correlated. The remaining measurements they keep as their key.

11 June 2026 13:34:37

© Author(s) 2023

modes and demonstrate in Fig. 16(c) that states within the same basis are orthogonal while the calculated overlap for states taken from mutually unbiased bases is non-zero, as expected. Figure 16(d) shows how a typical QKD experiment is performed. After Alice and Bob have agreed on the encoding basis (and its corresponding MUB), Alice encodes states that are randomly chosen from the $\{|\Psi_j\rangle\}$ and $\{|\Phi_j\rangle\}$ bases, while Bob randomly selects the basis to measure the received photon with. Each state that Alice has selected is mapped onto an alphabet, say $\{1, 2, 3\}$ that will encode the message (M). After all the photons have been measured by Bob, Alice announces the basis she prepared the photon on, while Bob announces whether he chose the same basis. They then discard the cases where the bases do not correlate and thereafter remain with the sifted key. The channel is still secure because the states themselves were not announced.

2. Security analysis

The key they remain with can be further characterized to test for eavesdropping and to perform error correction. First, they have to check whether the key has no imperfections. They proceed by measuring the quantum bit error rate (Q)[201] by exchanging a fraction of the transmitted key and checking whether they are identical. Depending on the action of the channel, $\hat{U}$, the bit error rates (Q) can be computed from the two measurement bases as[201]

$$Q_\Psi = 1 - \frac{1}{d}\sum_{i=1}^{d} |\langle \Psi_i^{\text{Bob}}|\hat{U}|\Psi_i^{\text{Alice}}\rangle|^2, \tag{61}$$

$$Q_\Phi = 1 - \frac{1}{d}\sum_{i=1}^{d} |\langle \Phi_i^{\text{Bob}}|\hat{U}|\Phi_i^{\text{Alice}}\rangle|^2, \tag{62}$$

each basis. The second term in each of the equations quantifies the fidelity of each measurement basis (as discussed in Sec. III A). Given the average error rate, $Q = 1/2(Q_\Psi + Q_\Phi)$, and the corresponding average fidelity $(F = 1 - Q)$, they can estimate the mutual information (I_{AB}) in the channel from Eq. (13). The highest achievable mutual information is given by $I_{AB}^{\max} = \log_2(d)$ for a d dimensional basis. While mutual information is a good measure for characterizing the channel, it is imperative to also estimate the amount of information that can be obtained by an eavesdropper. Assuming that the eavesdropper has a cloning machine that can make duplicates of the transmitted photons, then the amount of information that the eavesdropper can obtain is[66]

$$F_E(d, Q) = \frac{1}{d}\left(1 + (d-2)Q + 2\sqrt{(d-1)Q(1-Q)}\right), \tag{63}$$

which scales with $1/d$, showing that the eavesdropper introduces more errors into the key as the encoding dimensions are increased. Accordingly, the maximum cloning rate can be $(d-1)/d$. Using our formulas for mutual information, it can be shown that the mutual information shared between Alice and Eve,[66]

$$I_{AE}(d, Q) = \log_2(d) + (F_E - Q)\log_2\left(\frac{F_E - Q}{1-Q}\right) + (1 - F_E)\log_2\left(\frac{1 - F_E}{(d-1)(1-Q)}\right). \tag{64}$$

Because the cloning fidelity is limited to $(d-1)/d$, an eavesdropper extracts less amount of key bits for higher dimensional encoding ensuring optimal secrecy for larger encoding dimensions (d). Finally, given the error rates, Q, the lower bound on the secure key generation rate can be estimated from

$$R(d, Q) = \log_2(d) + 2(1-Q)\log_2(1-Q) + 2Q\log_2\left(\frac{Q}{d-1}\right), \tag{65}$$

which must be checked to ensure that the channel is secure and allows for forward error correction[202] by ensuring that $R(d, Q) > 0$. Figure 17 shows the secure key rate as a function of the error rates for dimensions $d = 2, 3, 4, 8$, and $d = 16$, demonstrating that QKD allows for higher key rates with increasing dimensions. Furthermore, we also see that QKD is tolerant to larger errors for higher dimensional bases; the key rate decays less rapidly for higher dimensional states than for lower ones. For example, for $d = 2$, we see that $R(2, Q) = 0$ for $Q \approx 0.11$, while for double the dimensions $(d = 4)$, $R(4, Q) = 0$ is only reached at a higher error rate of $Q = 0.19$. This tolerance appreciates with increasing dimensions, making higher dimensional encoding with structured light a good candidate for QKD due to the abundance of encoding dimensions. So far, successful demonstrations have been reported in transmission media such as optical fiber (d = 4[37,135]), free-space (d = 4,7[21,36]), and underwater channels.[133]

To realize the full potential of using higher dimensional QKD with spatial modes, several improvements are needed for current implementations. This includes having more efficient photon sources, efficient and fast modulation techniques for spatial mode encoding, and detection methods that are fast, deterministic, lossless, and resilient to perturbations in complex channels (see references focusing on turbulence[203] and optical fiber[204]). One main challenge is improving the measurement step due to increasing measurement complexity for higher dimensional modes. For example, because $2 \times d$ detectors are needed for d dimensional states, filter based techniques, i.e., measuring one mode at a time, are commonly used to reduce costs as well as avoid building complicated setups that require many optical elements. However, this reduces the performance by a factor of $1/d$. To overcome this limitation, spatial

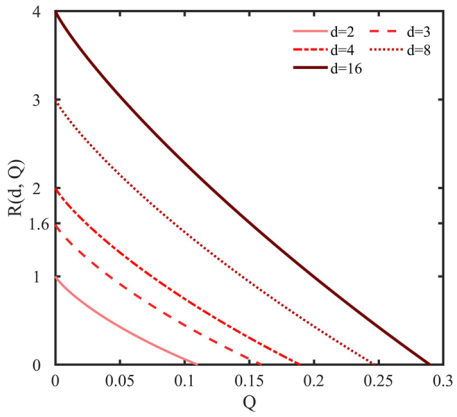


FIG. 17. Secure key rate. Secure key rates (bits per photon) for higher dimensional QKD as a function of the error rates (Q) for several d-dimensional encoding bases.

11 June 2026 13:34:37

© Author(s) 2023

mode sorting using two refractive optical elements[36,117,118,120,205] is being incorporated into the detection step (see the section on special optics, Sec. IV f). These techniques map the desired modes onto spots that can be easily measured with detector arrays. Recently, multi-plane light converters (MPLCs) applied to classical structured light detection[169] are showing promise with recent demonstrations extending to the quantum regime.[206]

B. Teleportation

A building block holding potential for developing quantum technology is quantum teleportation. Having received much attention since the seminal paper by Bennett *et al.*,[207] the protocol derives from the idea of transporting an entity between two distant points without it traveling or existing in the connecting distance. In this technique, the entities in question are states, which have been represented in many different systems from nuclear magnetic resonance[208] to atomic ensembles,[209–212] solid state systems,[213–216] and trapped atoms[217–221] along with photons, where degrees of freedom such as time,[222–224] path,[41,42] polarization,[47,225–230] or structured patterns[20] have been exploited.

Physically implementing teleportation has garnered much investigation due to the fundamental features governing it. We may understand this by looking at the general protocol. Using the previous convention of Alice and Bob, where Alice is the sender and Bob the receiver, Alice prepares a maximally entangled state with 2 photons, B and C, in Fig. 18. She then sends one (B) to Bob, creating a channel where quantum mechanical correlations now exist between them. In the ideal case of a 2-level discrete variable system, these maximally entangled qubits form one of the Bell pairs,[231] e.g.,

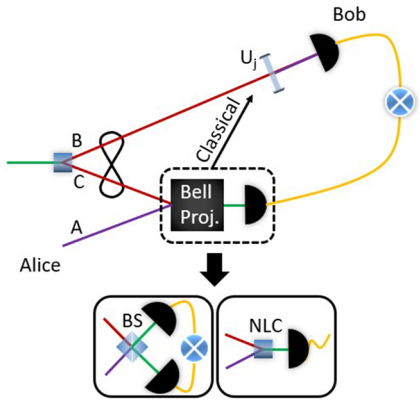


FIG. 18. Concept of spatial teleportation. Initially, a pair of entangled photons is shared between Alice (particle C) and Bob (particle B), establishing an entanglement channel. A third particle A containing an unknown or prepared state to be teleported is then mixed with Alice's particle. Alice then performs a measurement in an entanglement or "Bell" basis of A and C. This Bell projection collapses the entanglement between particles A and B while simultaneously entangling photons A and C as well as destroying the state of photon C. Alice then transmits classical information to Bob about the Bell measurement projection (j), allowing him to correct for any unitary rotation on the state being teleported (U_j) and realizing teleportation. Physical mixing of A and C may be realized through either a beam-splitter (BS) or a non-linear crystal (NC).

$$|\Phi^+\rangle_{CB} = \frac{1}{\sqrt{2}}(|0\rangle_C|0\rangle_B + |1\rangle_C|1\rangle_B). \tag{66}$$

A third photon A, with an unknown state $|\Psi\rangle_A$, possesses the information that needs to be transferred. Together, the three photons occupy the state

$$|\Omega\rangle_{ABC} = |\Psi\rangle_A \otimes |\Phi\rangle_{CB}. \tag{67}$$

By performing a joint quantum measurement or Bell detection[232–234] with photons A and C, photon B is projected onto the state

$$|\psi\rangle_B = P_j|\Psi\rangle_A, \tag{68}$$

imprinted with the unknown state of photon A but modified by the unitary P_j. Here, $P_j \in \{\sigma_0, \sigma_1, \sigma_2, \sigma_3\}$ is a Paulie operator [as defined in Eq. (52)].

Before the Bell measurement, photons A and C could be thought of as being in a superposition of every possible entangled combination. For each possible entangled state, Bob's photon has a form of the carrier's state, each with a unitary phase variation related to each entangled state that A and C might realize. A measurement of photons A and C on this basis then forces them to realize one of the entangled states. As a result, Bob has the teleported state within the unitary rotation resulting from the projective measurement. To retrieve the state, ρ, Alice then classically communicates the outcome of the Bell detection, j, to Bob such that the unitary correction, P_j, can be applied, and the state has thus been successfully teleported to Bob. The required classical communication then results in excluding the protocol from communication faster than the speed of light. Consequently, by mixing one of the entangled particles with that of a secondary entity carrying an unknown state and projecting them onto an entangled superposition, the unknown state can be conveyed without knowing or measuring it. As there is no direct observation of the state being sent, the superposition, as well as all the correlations, are maintained, preserving both the anonymity and any quantum nature.

As a result, teleportation can be exploited through a wide range of applications. For instance, it is an active component in the development of quantum information science,[231,235–237] with the conceptual scheme forming a fundamental step in formal quantum information theories, and its physical process forms a basic building block toward the development of many quantum technologies, allowing information exchange protected against eavesdropping.[238] Quantum technologies such as quantum repeaters,[239] measurement-based quantum computing[240] as well as quantum gate teleportation[241] derive from the quantum teleportation protocol, and it may be extended to the idea of a quantum network.[242]

Significant focus and progress have been given to extending the distance and fidelities[243] at which the protocols may be executed across both fiber[222,224,225,244,245] and free-space[229,230,246] with efforts extending to a low orbit satellite.[247] These advances bring forward the practicality of implementing large quantum networks, which can then form a quantum internet.[242,248,249] Only recently, however, has progress been made toward physically increasing the dimensionality of the states that can be sent using this protocol. This requires utilizing a basis of maximally entangled states and a unitary operator basis, $\{U_j\}$, whereby $\mathrm{tr}(U_i^\dagger U_j) = \delta_{i,j}d$,[250] so that the protocol can be extended beyond 2 dimensions and designed for any

11 June 2026 13:34:37

© Author(s) 2023

finite-dimensional Hilbert space of dimension, d. Here, the protocol remains similar to that of the 2-dimensional case, with P_j changed to U_j and d^2 possible outcomes to be communicated classically.

While theoretical protocols and proposals have been suggested,[250,251] this has proven difficult to implement physically, not from a lack of available properties to use as high dimensional states but rather from difficulty in mixing the carrier and entangled particle such that high-dimensional Bell projections can be made. Consequently, the limiting factor has been the black box in Fig. 18 to which two emerging solutions have been recently realized.

The first retains the traditional linear mixing tool where the two inputs are incident on different ports of a beam-splitter, and correlation measurements at the outputs allow one to select out a Bell state and thus render teleportation. Here, Refs. 41 and 42 exploit the path degree of freedom to realize three-dimensional teleportation, marking the first demonstrations to break the high-dimensional barrier. Previously, this was not achieved as linear optics is not able to distinguish $d > 2$ Bell states alone.[252] With the introduction of additional ancillary photons to the projection measurements, however, the degeneracy may be broken.[252,253] Refs. 41 and 42 subsequently constructed setups to achieve this with a scaling of $d - 2$ additional single photons and $\log_2(d) - 1$ additional pair, respectively. The demonstrations here remained in three dimensions, however, as this quickly becomes resource intensive and practically complex as d increases. It may be further noted that an intrinsic bound on efficiency exists with using a beam-splitter, as not all the Bell states may be detected and thus projected onto. Nevertheless, the schemes represent implementable high-dimensional teleportation of quantum states.

The second approach instead utilizes non-linear principles[87,254,255] to mix the carrier and channel photon. Here, instead of the linear element, a non-linear crystal is used in reverse.[43,256] Where before, one pump photon produced two entangled daughter photons, now two inputs (the carrier and channel photons) mix in the crystal such that an up-converted photon shares the properties and energy of the inputs. The upconverted photon thus forms a superposition of correlations that can be the projected onto the crystal by measurement and thus realize the necessary Bell projection. This can be understood using OAM as an example, with the projection of the upconverted photon onto the $\ell_{Bell} = 0$ state. From Eq. (23), we know that a pump photon of $\ell_p = 0$ generates $\ell_B = -\ell_C$. When using the process in reverse, the same conservation rules apply, such that projection onto $\ell_{Bell} = 0$ results in coincidences only when $\ell_A = -\ell_B = \ell_C$. It follows then that for the coincidences detected, Bob's photon must have the same state as A. Projection onto a different ℓ_{Bell} then only requires a unitary ℓ-related rotation on Bob's side, as was demonstrated in Ref. 256.

Here, the limitations in terms of dimensionality are only dependent on the capacity of the entanglement resource and the supported overlap resolution in the Bell projection crystal. To this end, the dimensions of the supported modes may be determined by[43]

$$K = \frac{\left[\int T^2(\mathbf{q}_A, \mathbf{q}_B)\mathrm{d}^2\mathbf{q}_A\mathrm{d}^2\mathbf{q}_B\right]^2}{\int\left[\int T(\mathbf{q}_A, \mathbf{q}_C)T(\mathbf{q}_C, \mathbf{q}_B)\mathrm{d}^2\mathbf{q}_C\right]^2\mathrm{d}^2\mathbf{q}_A\mathrm{d}^2\mathbf{q}_B}, \tag{69}$$

where

$$T(\mathbf{q}_A, \mathbf{q}_B) = \int \psi^*_{\mathrm{UC}}(\mathbf{q}_A, \mathbf{q}_C)\psi_{\mathrm{SPDC}}(\mathbf{q}_C, \mathbf{q}_B)\mathrm{d}^2\mathbf{q}_C, \tag{70}$$

and, as described in Sec. IV A 2, q_i represents the transverse wave vectors of photon i, ψ_{SPDC} is the SPDC wavefunction, and ψ_{UC} is the up-conversion wavefunction, which is the SPDC modeled reciprocally.

Accordingly, teleportation in dimensions significantly exceeding three was demonstrated.[43,256] Interestingly, this approach holds versatility in that the system supports spatial modes as a whole, such that various bases could be used, ranging from OAM states and arbitrary superpositions thereof[43] to pixels states[256] without adjustment. A point to note here, however, is that due to the low efficiencies associated with the non-linear process, the carrier is forced to be in a bright coherent state, such that enough single photons are present that the probability of upconvertion is large enough. As such, the nature of the carrier is classical until significant improvements in efficiency result, leading to this being called *stimulated* teleportation. A main consequence is that the teleportation technique is now limited in that correlations cannot be teleported, as this is a feature of quantum carriers.[257] Nonetheless, it has facilitated a significant development in that high-dimensional teleportation exceeds three dimensions several times over as well as offering on-demand teleportation across the spatial mode basis with potential toward quantum entangled states with technological development.

C. Quantum imaging

1. Ghost imaging protocol with structured pixel modes

It is known that the spatial correlations between signal and idler photon pairs produced by SPDC can be used within a quantum imaging system.[91,258–260] Image information is revealed by the correlations between the signal and idler photons and is not present in the detection of each individual photon. Fundamental to this approach to imaging, widely known as ghost imaging, is that the output plane of the NC in which the down-conversion process occurs is imaged such that each photon (signal and idler) is imaged onto the detector array and the object $[O(\mathbf{r})]$, respectively. The photons that interact with the object (idler) are collected by a "bucket detector," i.e., a detector with no spatial resolution. This can be a single mode or multi-mode fiber that is coupled to a single pixel detector. All that remains is to measure the spatial information of the idler photon.

Raster scanning was historically used to detect the signal photon, and the required spatial resolution for the signal photons was achieved by spatially scanning the transverse plane in the x-y direction by a scanning fiber.[91,261] Following the ghost imaging protocol, one workaround to a mechanical single-pixel scanning detector was the introduction of spatial projective patterned masks, such as turning on a single pixel on a photon modulating device such as an SLM. The use of a photon modulating device avoids the instability caused by a mechanical scanning fiber. The natural choice would be to construct a small detector scanning system by using single-pixel masks to accomplish single-pixel scanning. Employing a single

11 June 2026 13:34:37

© Author(s) 2023

pixel detector, however, considerably decreases the collection efficiency and results in an increase in the time required to reconstruct the image (extended integration times per mask are required),[53] i.e., the time spent on a single position on the transverse plane is considerably more to detect enough photons to establish a signal; if this is not performed, the image quality is compromised. Instead, 2-D patterned masks were developed that consist of pixels judiciously turned on and off and distributed across a grid of a pre-determined size (determined by the SLM screen size). Here, the signal photons are subsequently projected onto patterned masks, $P_k(\mathbf{r})$, where k indices the masks, i.e., $k = 1, 2, \ldots, N$. Given that the photons are produced by SPDC, the measured coincidence events for each kth projection can be estimated from

$$C_k = \left| \int \psi_{si}(\mathbf{r}) O(\mathbf{r}) P_k^*(\mathbf{r}) d^2 r \right|^2. \tag{71}$$

Here, $\psi_{si}(\mathbf{r})$, is the joint probability function of the signal and idler photons in the near field.

After completing the sequence of N measurements, the detection probabilities (C_k) are subsequently used to reconstruct the object. To achieve this, the second order coherence function is computed from[262]

$$\mathbf{I}(\mathbf{r}) = \frac{1}{N} \sum_{k=1}^{N} [C_k - \langle C_k \rangle_N] \mathbf{P}_k, \tag{72}$$

where $\langle \cdot \rangle_N$ is the ensemble average over the detection probabilities. Example reconstructions are shown in Fig. 19(b). The masks that are commonly used for the projections can be formed from *pixel* states that are discussed in Sec. II B. Here, we can describe the projection states as

$$|P_k\rangle = \sum_j p_{jk} |\mathbf{r}_j\rangle, \tag{73}$$

where $|\mathbf{r}_j\rangle$ maps onto a *pixel* mode located at $\mathbf{r}_j = (x_j, y_j)$, with the index j labeling the said *pixel* mode. Accordingly, the corresponding mask is $P_k(\mathbf{r}) = \langle \mathbf{r} | P_k \rangle$. There are several ways to choose the weightings p_{jk}. To construct these projections, one can choose between using (i) uncorrelated binary random masks or synthesising masks that are constructed from an (ii) orthogonal set of pixel modes.

For binary random masks, each pixel is randomly assigned a value of either 0 or 1. In this way, the masks contain randomly distributed binary pixels that are either turned on or off.[263] In the top panel of Fig. 19(b), we show examples of random patterned mask types used in a typical ghost image reconstruction. A drawback is that a large number of patterns are required ($2N^2$ or more, where $N \times N$ is the number of pixels in the image) to reconstruct an image that is noisy and, therefore, of poor quality.[264] Small improvements can be seen if half the pixels in each pattern are activated.[265]

In the bottom panel of Fig. 19(b), we show an alternative set of masks that can be formed from the family of Walsh–Hadamard basis masks that constitute an orthogonal basis.[266,267] Each element is generated from the Walsh–Hadamard matrix transform[268] of specific order N where the number of pixels making up the image is N^2. The Walsh–Hadamard transform is commonly used for recording spatial frequencies,[269] or for multiplexing the direction of the illumination of an object.[270,271] Walsh–Hadamard masks are generated by

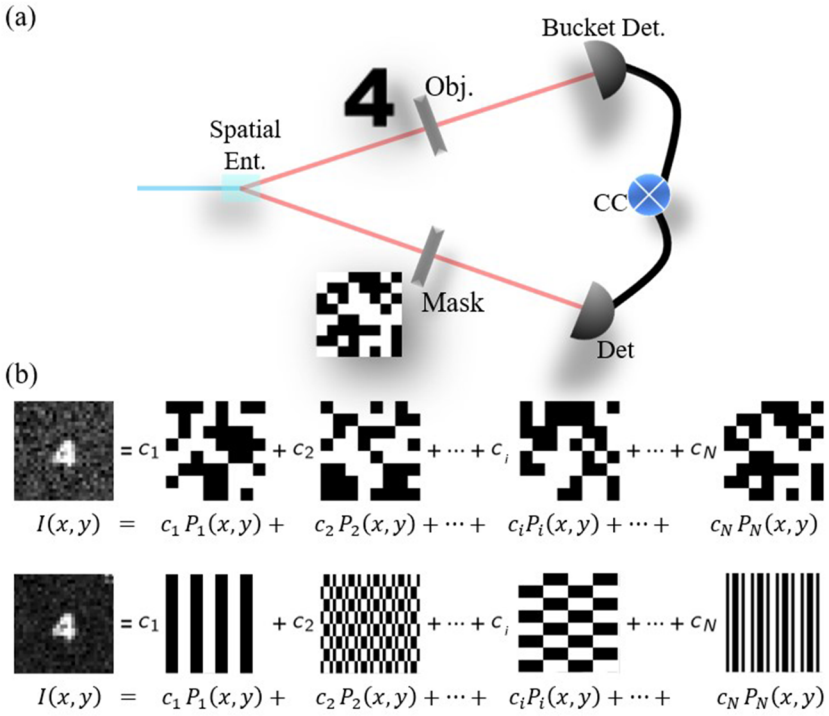


FIG. 19. Conceptualization of a quantum imaging. (a) One photon from a pair of spatially entangled photons interacts with an object and is collected by a detector without spatial resolution, while the photon that does not interact with the object is spatially resolved. When both photons are detected in coincidence, an image of the object is reconstructed. (b) The image $[I(x,y)]$ is reconstructed as a linear combination of each patterned mask $[P_i(x,y)]$, weighted by the detected coincidences (c_i). The top panel shows an example of image reconstruction by the random basis, while the bottom panel is an example of image reconstruction by the Hadamard basis.

11 June 2026 13:34:37

© Author(s) 2023

extracting the Walsh functions from the Walsh–Hadamard matrix of order N. The masks can be chosen so that

$$P_k(\mathbf{r}) \in \left\{ \frac{1}{\sqrt{2}} \left(W_n \otimes W_m^{\top} + \mathbb{I}_{N^2} \right)(x,y),\ m,n = 1,2,\ldots N \right\}. \quad (74)$$

Here $\otimes$ is the outer-product; the indices m and n label the corresponding columns of the Nth order Walsh–Hadamard transform that is used to construct the kth mask. The resulting outer-product is added to the N^2-dimensional identity matrix so that the normalized mask has pixels that scale from 0 to 1. Finally, the matrix is re-sampled to fit onto the SLM [defined in cartesian coordinates (x,y)]. The bottom panel of Fig. 19(b) shows an example of an image reconstruction with the Walsh–Hadamard mask type.

The mask resolution, independent of the type of mask chosen to spatially resolve the signal photons, will determine the resolution at which the object will be imaged. A higher resolution results in a larger number of basis elements and, therefore, an increased number of masks is needed to reconstruct the image. Increasing the resolution has direct consequences for the reconstruction time; the number of Walsh–Hadamard masks required to form a complete set scales as N^2. Specifically, for a complete or general image solution on the Walsh–Hadamard basis, N^2 masks are required. Although N^2 masks are required for a general image solution, it has been shown that it is possible to acquire image information up to 10× faster with the use of smart algorithms.[272,273]

Masks are generated as a pre-measurement step, i.e., they are generated prior to starting the experiment and stored in memory or in a local directory. Many programming languages can be used to generate the masks as they are defined earlier. Programming languages often come with native functions, allowing the user quick and easy mask generation. As an example, in the MATLAB programming language, by calling the function `Hadamard(N)`, a Hadamard matrix of order N is generated, where N defines the number of pixels in the mask. Similarly, to generate a random mask, one would use `rand(N,N)` in MATLAB.

2. Resolution limits for ghost imaging with SPDC photons

Importantly, one must assess the resolution limit of the quantum imaging system to determine the number of available effective pixels for image resolution. In a quantum imaging system, the resolution of the image (or the number of pixels the system is able to resolve) is limited by the point spread function (PSF) of the optics comprising the spatially resolving detector which is further reduced by the strength of the spatial correlations inherent in SPDC.[274] As aforementioned, the uniqueness of quantum imaging lies in choosing whether one measures the position or momentum correlations between the signal and idler photons in a single imaging setup. Here, we present the resolution limit calculation for the measurement of the momentum anti-correlations as measured in the far field. The strength of the momentum anti-correlations is set by the momentum uncertainty in the pump beam, which is controlled by the diameter of the pump mode field. Accordingly, the position correlation radius (as measured in the far field) between the signal and idler photons is given by[274]

$$\sigma_x \approx f \frac{2\lambda_p}{\pi w_p}, \quad (75)$$

where f is the effective focal length of the Fourier-transform lens, λ_p is the wavelength of the pump beam, and w_p is the waist of the pump beam. In Ref. 274, the authors postulate that irrespective of the resolving power of the optical system, this correlation sets the resolution limit, which cannot be exceeded by the quantum imaging system, while the size of the pump beam sets the resolution. The field of view (FOV) of the imaging system is set by the phase matching imposed by the length of the chosen NC,[274]

$$FOV_x \approx f\sqrt{\frac{\lambda_p}{L}}, \quad (76)$$

where L is the length of the chosen NC. It is, therefore, possible to infer that a limit on the number of resolution cells available for ghost imaging is generated by the SPDC,

$$V = \left(\frac{FOV_x}{\sigma_x} \right)^2 \approx \frac{\pi^2 w_p^2}{4L\lambda_p}. \quad (77)$$

This number corresponds to the limit of the number of effective pixels in the reconstructed ghost images that are resolved due to the properties of the SPDC. V is also the Schmidt number of the entanglement in the spatial basis.

3. Structured light in quantum imaging

The quantum imaging approaches we discussed in this tutorial used structured light modes in the form of patterned *pixels* encoded on SLMs as part of the measurements. Interestingly, spiral phases that are reminiscent of OAM modes, as well as binary phase steps reminiscent of HG modes, have also been incorporated to improve the performance of phase contrast images in quantum ghost imaging experiments with single pixel scanning.[22] Recently, it has also been demonstrated that the necessary information for phase retrieval is naturally embedded in the correlation measurements formed from traditional patterned pixels, as detailed earlier.[275]

While these projective approaches that make use of structured pixels are cost effective, quantum imaging with single photon sensitive cameras has recently taken center stage (see Refs. 276 and 277), making it easier to execute quantum imaging experiments. Recent approaches involve using quantum sources (mainly SPDC photons) to illuminate objects and measure the spatially and temporally modulated photons using single photon cameras.[278–280] In addition, these cameras have also been used for performing fundamental tests of quantum mechanics (spatial Bell-inequality tests,[281,282] spatial quantum interference[283]) and for characterizing quantum structured light (spatial-momentum entanglement witnessing,[284] OAM entanglement state tomography[285]). Entanglement sources beyond single degrees of freedom, i.e., hyper-entanglement being the simultaneous entanglement of multiple degrees of freedom (polarization-spatial, in this case), have been used for quantum holography.[286]

On the other hand, interaction free (see early papers on this topic[287–289]) imaging approaches are becoming prevalent, where single photon interference is used as the main tool for imaging transparent objects.[290] Alternatively, image formation can be achieved through quantum interference,[291] i.e., using the Hong–Ou–Mandel interference effect. While these techniques make use of linear optical elements to achieve the interference, the authors in Ref. 292

11 June 2026 13:34:37

© Author(s) 2023

used multiple nonlinear crystals, inducing coherence between pump and signal photons that share a common idler mode, allowing the transfer of information from signal to idler through SPDC[293,294] (see Ref. 295 for a detailed tutorial). Here, the degrees of freedom that are manipulated are the transverse spatial and wavelength/frequency of photons, demonstrating superb control of quantum information in an imaging experiment by exploiting nonlinear optics.

VII. CONCLUDING REMARKS

In this tutorial, we have outlined the basic theory behind realizing high-dimensional quantum states on the basis of spatial modes. We have explained with practical examples how to get started with the experiment, how to prepare and measure quantum states, and finally, how to use this as a resource in quantum information processing and imaging. Rather than a comprehensive monograph, it is a quick guide that serves as a useful starting point for both students and new researchers in the field. As such, we have used common "vanilla" forms of experiments as a means to convey the message, for example, using SPDC as the source of entangled photons and OAM as the basis for measurement. We stress that the state-of-the-art is far more versatile and encourage the interested reader to explore more widely for an advanced treatment beyond this tutorial.

AUTHOR DECLARATIONS

Conflict of Interest

The authors have no conflicts to disclose.

Author Contributions

Isaac Nape: Writing – original draft (lead); Writing – review & editing (lead). **Bereneice Sephton**: Writing – original draft (equal); Writing – review & editing (equal). **Pedro Ornelas**: Writing – original draft (equal); Writing – review & editing (supporting). **Chane Moodley**: Writing – original draft (supporting); Writing – review & editing (supporting). **Andrew Forbes**: Writing – original draft (lead); Writing – review & editing (equal).

DATA AVAILABILITY

The data that support the findings of this study are available from the corresponding author upon reasonable request.

REFERENCES

[1] A. Forbes, M. de Oliveira, and M. R. Dennis, "Structured light," Nat. Photonics **15**, 253–262 (2021).
[2] Y. Shen, "Rays, waves, SU (2) symmetry and geometry: Toolkits for structured light," J. Opt. **23**, 124004 (2021).
[3] M. Piccardo, V. Ginis, A. Forbes, S. Mahler, A. A. Friesem, N. Davidson, H. Ren, A. H. Dorrah, F. Capasso, F. T. Dullo *et al.*, "Roadmap on multimode light shaping," J. Opt. **24**, 013001 (2021).
[4] A. Chong, C. Wan, J. Chen, and Q. Zhan, "Generation of spatiotemporal optical vortices with controllable transverse orbital angular momentum," Nat. Photonics **14**, 350–354 (2020).
[5] C. Wan, Q. Cao, J. Chen, A. Chong, and Q. Zhan, "Toroidal vortices of light," Nat. Photonics **16**, 519 (2022).
[6] A. Zdagkas, C. McDonnell, J. Deng, Y. Shen, G. Li, T. Ellenbogen, N. Papasimakis, and N. I. Zheludev, "Observation of toroidal pulses of light," Nat. Photonics **16**, 523–528 (2022).
[7] C. He, Y. Shen, and A. Forbes, "Towards higher-dimensional structured light," Light: Sci. Appl. **11**, 205 (2022).
[8] Y. Shen, X. Wang, Z. Xie, C. Min, X. Fu, Q. Liu, M. Gong, and X. Yuan, "Optical vortices 30 years on: OAM manipulation from topological charge to multiple singularities," Light: Sci. Appl. **8**, 90 (2019).
[9] A. Forbes, "Structured light from lasers," Laser Photonics Rev. **13**, 1900140 (2019).
[10] M. J. Padgett, "Orbital angular momentum 25 years on," Opt. Express **25**, 11265–11274 (2017).
[11] S. Franke-Arnold, "30 years of orbital angular momentum of light," Nat. Rev. Phys. **4**, 361 (2022).
[12] L. Allen, M. W. Beijersbergen, R. J. C. Spreeuw, and J. P. Woerdman, "Orbital angular momentum of light and the transformation of Laguerre-Gaussian laser modes," Phys. Rev. A **45**, 8185 (1992).
[13] A. Forbes, S. Ramachandran, and Q. Zhan, "Photonic angular momentum: Progress and perspectives," Nanophotonics **11**, 625–631 (2022).
[14] A. Mair, A. Vaziri, G. Weihs, and A. Zeilinger, "Entanglement of the orbital angular momentum states of photons," Nature **412**, 313–316 (2001).
[15] M. Erhard, R. Fickler, M. Krenn, and A. Zeilinger, "Twisted photons: New quantum perspectives in high dimensions," Light: Sci. Appl. **7**, 17146 (2018).
[16] A. Forbes and I. Nape, "Quantum mechanics with patterns of light: Progress in high dimensional and multidimensional entanglement with structured light," AVS Quantum Sci. **1**, 011701 (2019).
[17] D. Cozzolino, B. Da Lio, D. Bacco, and L. K. Oxenløwe, "High-dimensional quantum communication: Benefits, progress, and future challenges," Adv. Quantum Technol. **2**, 1900038 (2019).
[18] M. McLaren, T. Mhlanga, M. J. Padgett, F. S. Roux, and A. Forbes, "Self-healing of quantum entanglement after an obstruction," Nat. Commun. **5**, 3248 (2014).
[19] E. Nagali, L. Sansoni, L. Marrucci, E. Santamato, and F. Sciarrino, "Experimental generation and characterization of single-photon hybrid ququarts based on polarization and orbital angular momentum encoding," Phys. Rev. A **81**, 052317 (2010).
[20] X.-L. Wang, X.-D. Cai, Z.-E. Su, M.-C. Chen, D. Wu, L. Li, N.-L. Liu, C.-Y. Lu, and J.-W. Pan, "Quantum teleportation of multiple degrees of freedom of a single photon," Nature **518**, 516–519 (2015).
[21] A. Sit, F. Bouchard, R. Fickler, J. Gagnon-Bischoff, H. Larocque, K. Heshami, D. Elser, C. Peuntinger, K. Günthner, B. Heim, C. Marquardt, G. Leuchs, R. W. Boyd, and E. Karimi, "High-dimensional intracity quantum cryptography with structured photons," Optica **4**, 1006 (2017).
[22] B. Jack, J. Leach, J. Romero, S. Franke-Arnold, M. Ritsch-Marte, S. M. Barnett, and M. J. Padgett, "Holographic ghost imaging and the violation of a Bell inequality," Phys. Rev. Lett. **103**, 083602 (2009).
[23] E. Toninelli, B. Ndagano, A. Vallés, B. Sephton, I. Nape, A. Ambrosio, F. Capasso, M. J. Padgett, and A. Forbes, "Concepts in quantum state tomography and classical implementation with intense light: A tutorial," Adv. Opt. Photonics **11**, 67–134 (2019).
[24] J. Leach, B. Jack, J. Romero, A. K. Jha, A. M. Yao, S. Franke-Arnold, D. G. Ireland, R. W. Boyd, S. M. Barnett, and M. J. Padgett, "Quantum correlations in optical angle–orbital angular momentum variables," Science **329**, 662–665 (2010).
[25] A. C. Dada, J. Leach, G. S. Buller, M. J. Padgett, and E. Andersson, "Experimental high-dimensional two-photon entanglement and violations of generalized Bell inequalities," Nat. Phys. **7**, 677–680 (2011).
[26] M. Agnew, J. Leach, M. McLaren, F. S. Roux, and R. W. Boyd, "Tomography of the quantum state of photons entangled in high dimensions," Phys. Rev. A **84**, 062101 (2011).
[27] I. Nape, V. Rodríguez-Fajardo, F. Zhu, H. C. Huang, J. Leach, and A. Forbes, "Measuring dimensionality and purity of high-dimensional entangled states," Nat. Commun. **12**, 5159 (2021).

11 June 2026 13:34:37

© Author(s) 2023

[28]J. Bavaresco, N. Herrera Valencia, C. Klöckl, M. Pivoluska, P. Erker, N. Friis, M. Malik, and M. Huber, "Measurements in two bases are sufficient for certifying high-dimensional entanglement," Nat. Phys. **14**, 1032–1037 (2018).
[29]Y. Zhang, F. S. Roux, T. Konrad, M. Agnew, J. Leach, and A. Forbes, "Engineering two-photon high-dimensional states through quantum interference," Sci. Adv. **2**, e1501165 (2016).
[30]F. M. Miatto, A. M. Yao, and S. M. Barnett, "Full characterization of the quantum spiral bandwidth of entangled biphotons," Phys. Rev. A **83**, 033816 (2011).
[31]G. Molina-Terriza, J. P. Torres, and L. Torner, "Management of the angular momentum of light: Preparation of photons in multidimensional vector states of angular momentum," Phys. Rev. Lett. **88**, 013601 (2001).
[32]M. Krenn, M. Huber, R. Fickler, R. Lapkiewicz, S. Ramelow, and A. Zeilinger, "Generation and confirmation of a (100 × 100)-dimensional entangled quantum system," Proc. Natl. Acad. Sci. U. S. A. **111**, 6243–6247 (2014).
[33]M. Erhard, M. Malik, M. Krenn, and A. Zeilinger, "Experimental Greenberger–Horne–Zeilinger entanglement beyond qubits," Nat. Photonics **12**, 759–764 (2018).
[34]M. Krenn, A. Hochrainer, M. Lahiri, and A. Zeilinger, "Entanglement by path identity," Phys. Rev. Lett. **118**, 080401 (2017).
[35]M. Mafu, A. Dudley, S. Goyal, D. Giovannini, M. McLaren, M. J. Padgett, T. Konrad, F. Petruccione, N. Lütkenhaus, and A. Forbes, "Higher-dimensional orbital-angular-momentum-based quantum key distribution with mutually unbiased bases," Phys. Rev. A **88**, 032305 (2013).
[36]M. Mirhosseini, O. S. Magaña-Loaiza, M. N. O'Sullivan, B. Rodenburg, M. Malik, M. P. J. Lavery, M. J. Padgett, D. J. Gauthier, and R. W. Boyd, "High-dimensional quantum cryptography with twisted light," New J. Phys. **17**, 033033 (2015).
[37]D. Cozzolino, D. Bacco, B. Da Lio, K. Ingerslev, Y. Ding, K. Dalgaard, P. Kristensen, M. Galili, K. Rottwitt, S. Ramachandran *et al.*, "Orbital angular momentum states enabling fiber-based high-dimensional quantum communication," Phys. Rev. Appl. **11**, 064058 (2019).
[38]H. Cao, S.-C. Gao, C. Zhang, J. Wang, D.-Y. He, B.-H. Liu, Z.-W. Zhou, Y.-J. Chen, Z.-H. Li, S.-Y. Yu *et al.*, "Distribution of high-dimensional orbital angular momentum entanglement over a 1 km few-mode fiber," Optica **7**, 232–237 (2020).
[39]J. Pinnell, I. Nape, M. de Oliveira, N. TabeBordbar, and A. Forbes, "Experimental demonstration of 11-dimensional 10-party quantum secret sharing," Laser Photonics Rev. **14**, 2000012 (2020).
[40]Y. Zhang, M. Agnew, T. Roger, F. S. Roux, T. Konrad, D. Faccio, J. Leach, and A. Forbes, "Simultaneous entanglement swapping of multiple orbital angular momentum states of light," Nat. Commun. **8**, 632 (2017).
[41]Y. H. Luo, H. S. Zhong, M. Erhard, X. L. Wang, L. C. Peng, M. Krenn, X. Jiang, L. Li, N. L. Liu, C. Y. Lu *et al.*, "Quantum teleportation in high dimensions," Phys. Rev. Lett. **123**, 070505 (2019).
[42]X.-M. Hu, C. Zhang, B.-H. Liu, Y. Cai, X.-J. Ye, Y. Guo, W.-B. Xing, C.-X. Huang, Y.-F. Huang, C.-F. Li *et al.*, "Experimental high-dimensional quantum teleportation," Phys. Rev. Lett. **125**, 230501 (2020).
[43]B. Sephton, A. Vallés, I. Nape, M. A. Cox, F. Steinlechner, T. Konrad, J. P. Torres, F. S. Roux, and A. Forbes, "Stimulated teleportation of high-dimensional information with a nonlinear spatial mode detector," arXiv:2111.13624 (2021).
[44]A. Aspect, P. Grangier, and G. Roger, "Experimental realization of Einstein-Podolsky-Rosen-Bohm gedanken experiment: A new violation of Bell's inequalities," Phys. Rev. Lett. **49**, 91 (1982).
[45]S. Walborn, M. T. Cunha, S. Pádua, and C. Monken, "Double-slit quantum eraser," Phys. Rev. A **65**, 033818 (2002).
[46]C. H. Bennett and G. Brassard, "Quantum cryptography: Public key distribution and coin tossing," in *Proceedings of the IEEE International Conference on Computers, Systems and Signal Processing* (IEEE, New York, 1984), Vol. 175, p. 8.
[47]D. Bouwmeester, J.-W. Pan, K. Mattle, M. Eibl, H. Weinfurter, and A. Zeilinger, "Experimental quantum teleportation," Nature **390**, 575–579 (1997).
[48]K. Mattle, H. Weinfurter, P. G. Kwiat, and A. Zeilinger, "Dense coding in experimental quantum communication," Phys. Rev. Lett. **76**, 4656 (1996).
[49]M. N. O'Sullivan-Hale, I. A. Khan, R. W. Boyd, and J. C. Howell, "Pixel entanglement: Experimental realization of optically entangled d = 3 and d = 6 qudits," Phys. Rev. Lett. **94**, 220501 (2005).
[50]I. Ali-Khan, C. J. Broadbent, and J. C. Howell, "Large-alphabet quantum key distribution using energy-time entangled bipartite states," Phys. Rev. Lett. **98**, 060503 (2007).
[51]D. Richart, Y. Fischer, and H. Weinfurter, "Experimental implementation of higher dimensional time–energy entanglement," Appl. Phys. B **106**, 543–550 (2012).
[52]N. Herrera Valencia, V. Srivastav, M. Pivoluska, M. Huber, N. Friis, W. McCutcheon, and M. Malik, "High-dimensional pixel entanglement: Efficient generation and certification," Quantum **4**, 376 (2020).
[53]V. Rodríguez-Fajardo, J. Pinnell, and A. Forbes, "Towards time-efficient ghost imaging," J. Mod. Opt. **67**, 1176–1183 (2020).
[54]M. McLaren, M. Agnew, J. Leach, F. S. Roux, M. J. Padgett, R. W. Boyd, and A. Forbes, "Entangled Bessel-Gaussian beams," Opt. Express **20**, 23589–23597 (2012).
[55]M. Krenn, R. Fickler, M. Huber, R. Lapkiewicz, W. Plick, S. Ramelow, and A. Zeilinger, "Entangled singularity patterns of photons in ince-gauss modes," Phys. Rev. A **87**, 012326 (2013).
[56]S. Walborn, S. Pádua, and C. Monken, "Conservation and entanglement of Hermite-Gaussian modes in parametric down-conversion," Phys. Rev. A **71**, 053812 (2005).
[57]O. Lib and Y. Bromberg, "Spatially entangled airy photons," Opt. Lett. **45**, 1399–1402 (2020).
[58]V. D. Salakhutdinov, E. R. Eliel, and W. Löffler, "Full-field quantum correlations of spatially entangled photons," Phys. Rev. Lett. **108**, 173604 (2012).
[59]M. J. Padgett and J. Courtial, "Poincaré-sphere equivalent for light beams containing orbital angular momentum," Opt. Lett. **24**, 430–432 (1999).
[60]J. Romero, D. Giovannini, S. Franke-Arnold, S. Barnett, and M. Padgett, "Increasing the dimension in high-dimensional two-photon orbital angular momentum entanglement," Phys. Rev. A **86**, 012334 (2012).
[61]F. Bouchard, K. Heshami, D. England, R. Fickler, R. W. Boyd, B.-G. Englert, L. L. Sánchez-Soto, and E. Karimi, "Experimental investigation of high-dimensional quantum key distribution protocols with twisted photons," Quantum **2**, 111 (2018).
[62]S. Ecker, F. Bouchard, L. Bulla, F. Brandt, O. Kohout, F. Steinlechner, R. Fickler, M. Malik, Y. Guryanova, R. Ursin *et al.*, "Overcoming noise in entanglement distribution," Phys. Rev. X **9**, 041042 (2019).
[63]A. Einstein, B. Podolsky, and N. Rosen, "Can quantum-mechanical description of physical reality be considered complete?," Phys. Rev. **47**, 777 (1935).
[64]J. S. Bell and J. S. Bell, *Speakable and Unspeakable in Quantum Mechanics: Collected Papers on Quantum Philosophy* (Cambridge University Press, 2004).
[65]M. Horodecki and P. Horodecki, "Reduction criterion of separability and limits for a class of distillation protocols," Phys. Rev. A **59**, 4206 (1999).
[66]N. J. Cerf, M. Bourennane, A. Karlsson, and N. Gisin, "Security of quantum key distribution using d-level systems," Phys. Rev. Lett. **88**, 127902 (2002).
[67]J. Pinnell, V. Rodríguez-Fajardo, and A. Forbes, "Probing the limits of orbital angular momentum generation and detection with spatial light modulators," J. Opt. **23**, 015602 (2020).
[68]B. M. Terhal and P. Horodecki, "Schmidt number for density matrices," Phys. Rev. A **61**, 040301 (2000).
[69]C. K. Law and J. H. Eberly, "Analysis and interpretation of high transverse entanglement in optical parametric down conversion," Phys. Rev. Lett. **92**, 127903 (2004).
[70]J. B. Pors, S. S. R. Oemrawsingh, A. Aiello, M. P. Van Exter, E. R. Eliel, J. Woerdman *et al.*, "Shannon dimensionality of quantum channels and its application to photon entanglement," Phys. Rev. Lett. **101**, 120502 (2008).
[71]F. Miatto, D. Giovannini, J. Romero, S. Franke-Arnold, S. Barnett, and M. Padgett, "Bounds and optimisation of orbital angular momentum bandwidths within parametric down-conversion systems," Eur. Phys. J. D **66**, 178 (2012).
[72]F. Zhu, M. Tyler, N. H. Valencia, M. Malik, and J. Leach, "Is high-dimensional photonic entanglement robust to noise?," AVS Quantum Sci. **3**, 011401 (2021).
[73]S. Slussarenko and G. J. Pryde, "Photonic quantum information processing: A concise review," Appl. Phys. Rev. **6**, 041303 (2019).
[74]F. Flamini, N. Spagnolo, and F. Sciarrino, "Photonic quantum information processing: A review," Rep. Prog. Phys. **82**, 016001 (2018).

11 June 2026 13:34:37

© Author(s) 2023

[75]F. Steinlechner, M. Gilaberte, M. Jofre, T. Scheidl, J. P. Torres, V. Pruneri, and R. Ursin, "Efficient heralding of polarization-entangled photons from type-0 and type-II spontaneous parametric downconversion in periodically poled $KTiOPO_4$," J. Opt. Soc. Am. B **31**, 2068–2076 (2014).
[76]M. M. Fejer, G. A. Magel, D. H. Jundt, and R. L. Byer, "Quasi-phase-matched second harmonic generation: Tuning and tolerances," IEEE J. Quantum Electron. **28**, 2631–2654 (1992).
[77]A. Anwar, C. Perumangatt, F. Steinlechner, T. Jennewein, and A. Ling, "Entangled photon-pair sources based on three-wave mixing in bulk crystals," Rev. Sci. Instrum. **92**, 041101 (2021).
[78]H. De Riedmatten, I. Marcikic, H. Zbinden, and N. Gisin, "Creating high dimensional entanglement using mode-locked lasers," Quantum Inf. Comput. **2**, 425–433 (2002).
[79]R. T. Thew, A. Acin, H. Zbinden, and N. Gisin, "Bell-type test of energy-time entangled qutrits," Phys. Rev. Lett. **93**, 010503 (2004).
[80]A. Rossi, G. Vallone, A. Chiuri, F. De Martini, and P. Mataloni, "Multipath entanglement of two photons," Phys. Rev. Lett. **102**, 153902 (2009).
[81]L. Neves, G. Lima, J. G. Aguirre Gómez, C. H. Monken, C. Saavedra, and S. Pádua, "Generation of entangled states of qudits using twin photons," Phys. Rev. Lett. **94**, 100501 (2005).
[82]G. Molina-Terriza, J. P. Torres, and L. Torner, "Twisted photons," Nat. Phys. **3**, 305–310 (2007).
[83]T. Yarnall, A. F. Abouraddy, B. E. A. Saleh, and M. C. Teich, "Experimental violation of Bell's inequality in spatial-parity space," Phys. Rev. Lett. **99**, 170408 (2007).
[84]M. Erhard, M. Krenn, and A. Zeilinger, "Advances in high-dimensional quantum entanglement," Nat. Rev. Phys. **2**, 365–381 (2020).
[85]L. Mandel and E. Wolf, *Optical Coherence and Quantum Optics* (Cambridge University Press, 1995).
[86]J. P. Torres, K. Banaszek, and I. A. Walmsley, "Engineering nonlinear optic sources of photonic entanglement," in *Progress in Optics* (Elsevier, 2011), Vol. **56**, pp. 227–331.
[87]S. P. Walborn, C. H. Monken, S. Pádua, and P. H. Souto Ribeiro, "Spatial correlations in parametric down-conversion," Phys. Rep. **495**, 87–139 (2010).
[88]B. E. Saleh, A. F. Abouraddy, A. V. Sergienko, and M. C. Teich, "Duality between partial coherence and partial entanglement," Phys. Rev. A **62**, 043816 (2000).
[89]F. M. Miatto, H. di Lorenzo Pires, S. M. Barnett, and M. P. van Exter, "Spatial schmidt modes generated in parametric down-conversion," Eur. Phys. J. D **66**, 263 (2012).
[90]D. N. Klyshko, "A simple method of preparing pure states of an optical field, of implementing the Einstein–Podolsky–Rosen experiment, and of demonstrating the complementarity principle," Sov. Phys. Usp. **31**, 74 (1988).
[91]T. B. Pittman, D. V. Strekalov, D. N. Klyshko, M. H. Rubin, A. V. Sergienko, and Y. H. Shih, "Two-photon geometric optics," Phys. Rev. A **53**, 2804 (1996).
[92]C. H. Monken, P. H. S. Ribeiro, and S. Pádua, "Transfer of angular spectrum and image formation in spontaneous parametric down-conversion," Phys. Rev. A **57**, 3123 (1998).
[93]S. Oemrawsingh, J. De Jong, X. Ma, A. Aiello, E. Eliel, J. Woerdman *et al.*, "High-dimensional mode analyzers for spatial quantum entanglement," Phys. Rev. A **73**, 032339 (2006).
[94]M. McLaren, J. Romero, M. J. Padgett, F. S. Roux, and A. Forbes, "Two-photon optics of Bessel-Gaussian modes," Phys. Rev. A **88**, 033818 (2013).
[95]R. S. Aspden, D. S. Tasca, A. Forbes, R. W. Boyd, and M. J. Padgett, "Experimental demonstration of Klyshko's advanced-wave picture using a coincidence-count based, camera-enabled imaging system," J. Mod. Opt. **61**, 547–551 (2014).
[96]H. Takesue and K. Shimizu, "Effects of multiple pairs on visibility measurements of entangled photons generated by spontaneous parametric processes," Opt. Commun. **283**, 276–287 (2010).
[97]J. Schneeloch, S. H. Knarr, D. F. Bogorin, M. L. Levangie, C. C. Tison, R. Frank, G. A. Howland, M. L. Fanto, and P. M. Alsing, "Introduction to the absolute brightness and number statistics in spontaneous parametric down-conversion," J. Opt. **21**, 043501 (2019).
[98]M. Takeoka, R.-B. Jin, and M. Sasaki, "Full analysis of multi-photon pair effects in spontaneous parametric down conversion based photonic quantum information processing," New J. Phys. **17**, 043030 (2015).
[99]F. Graffitti, P. Barrow, M. Proietti, D. Kundys, and A. Fedrizzi, "Independent high-purity photons created in domain-engineered crystals," Optica **5**, 514–517 (2018).
[100]T. Pittman, B. Jacobs, and J. Franson, "Single photons on pseudodemand from stored parametric down-conversion," Phys. Rev. A **66**, 042303 (2002).
[101]A. L. Migdall, D. Branning, and S. Castelletto, "Tailoring single-photon and multiphoton probabilities of a single-photon on-demand source," Phys. Rev. A **66**, 053805 (2002).
[102]F. Kaneda and P. G. Kwiat, "High-efficiency single-photon generation via large-scale active time multiplexing," Sci. Adv. **5**, eaaw8586 (2019).
[103]A. Forbes, A. Dudley, and M. McLaren, "Creation and detection of optical modes with spatial light modulators," Adv. Opt. Photonics **8**, 200–227 (2016).
[104]J. Pinnell, I. Nape, B. Sephton, M. A. Cox, V. Rodríguez-Fajardo, and A. Forbes, "Modal analysis of structured light with spatial light modulators: A practical tutorial," J. Opt. Soc. Am. A **37**, C146–C160 (2020).
[105]F. S. Roux and Y. Zhang, "Projective measurements in quantum and classical optical systems," Phys. Rev. A **90**, 033835 (2014).
[106]S. Scholes, R. Kara, J. Pinnell, V. Rodríguez-Fajardo, and A. Forbes, "Structured light with digital micromirror devices: A guide to best practice," Opt. Eng. **59**, 041202 (2019).
[107]V. Arrizón, U. Ruiz, R. Carrada, and L. A. González, "Pixelated phase computer holograms for the accurate encoding of scalar complex fields," J. Opt. Soc. Am. A **24**, 3500–3507 (2007).
[108]C. Rosales-Guzmán and A. Forbes, "How to shape light with spatial light modulators," Proc. SPIE **SL30**, 57 (2017).
[109]J. A. Davis, D. M. Cottrell, J. Campos, M. J. Yzuel, and I. Moreno, "Encoding amplitude information onto phase-only filters," Appl. Opt. **38**, 5004–5013 (1999).
[110]E. Bolduc, N. Bent, E. Santamato, E. Karimi, and R. W. Boyd, "Exact solution to simultaneous intensity and phase encryption with a single phase-only hologram," Opt. Lett. **38**, 3546–3549 (2013).
[111]T. W. Clark, R. F. Offer, S. Franke-Arnold, A. S. Arnold, and N. Radwell, "Comparison of beam generation techniques using a phase only spatial light modulator," Opt. Exp. **24**, 6249–6264 (2016).
[112]J. Svozilík, J. Peřina, Jr., and J. P. Torres, "High spatial entanglement via chirped quasi-phase-matched optical parametric down-conversion," Phys. Rev. A **86**, 052318 (2012).
[113]R. Fickler, R. Lapkiewicz, W. N. Plick, M. Krenn, C. Schaeff, S. Ramelow, and A. Zeilinger, "Quantum entanglement of high angular momenta," Science **338**, 640–643 (2012).
[114]S. Straupe, D. Ivanov, A. Kalinkin, I. Bobrov, and S. Kulik, "Angular schmidt modes in spontaneous parametric down-conversion," Phys. Rev. A **83**, 060302 (2011).
[115]F. Cardano, F. Massa, H. Qassim, E. Karimi, S. Slussarenko, D. Paparo, C. de Lisio, F. Sciarrino, E. Santamato, R. W. Boyd *et al.*, "Quantum walks and wavepacket dynamics on a lattice with twisted photons," Sci. Adv. **1**, e1500087 (2015).
[116]E. Nagali and F. Sciarrino, "Generation of hybrid polarization-orbital angular momentum entangled states," Opt. Express **18**, 18243–18248 (2010).
[117]B. Ndagano, I. Nape, B. Perez-Garcia, S. Scholes, R. I. Hernandez-Aranda, T. Konrad, M. P. J. Lavery, and A. Forbes, "A deterministic detector for vector vortex states," Sci. Rep. **7**, 013882 (2017).
[118]M. P. J. Lavery, D. J. Robertson, G. C. G. Berkhout, G. D. Love, M. J. Padgett, and J. Courtial, "Refractive elements for the measurement of the orbital angular momentum of a single photon," Opt. Express **20**, 2110–2115 (2012).
[119]M. P. J. Lavery, D. J. Robertson, A. Sponselli, J. Courtial, N. K. Steinhoff, G. A. Tyler, A. E. Wilner, and M. J. Padgett, "Efficient measurement of an optical orbital-angular-momentum spectrum comprising more than 50 states," New J. Phys. **15**, 013024 (2013).
[120]M. Mirhosseini, M. Malik, Z. Shi, and R. W. Boyd, "Efficient separation of the orbital angular momentum eigenstates of light," Nat. Commun. **4**, 2781 (2013).

11 June 2026 13:34:37

© Author(s) 2023

[121]G. Lazarev, P.-J. Chen, J. Strauss, N. Fontaine, and A. Forbes, "Beyond the display: Phase-only liquid crystal on silicon devices and their applications in photonics," Opt. Express **27**, 16206–16249 (2019).
[122]R. W. Batterman, "Falling cats, parallel parking, and polarized light," Stud. Hist. Philos. Sci., Part B **34**, 527–557 (2003).
[123]S. Pancharatnam, "Generalized theory of interference and its applications. Part 1. Coherent pencils," in *Proceedings of the Indian Academy of Sciences* (Indian Academy of Sciences, 1956), Vol. 44, pp. 247–262.
[124]S. Pancharatnam, "Generalized theory of interference and its applications. Part 2: Partially coherent pencils," in *Proceedings of the Indian Academy of Sciences* (Indian Academy of Sciences, 1956), Vol. 44, pp. 398–417.
[125]M. V. Berry, "Quantal phase factors accompanying adiabatic changes," Proc. R. Soc. London, Ser A **392**, 45–57 (1984).
[126]Z. Bomzon, V. Kleiner, and E. Hasman, "Pancharatnam–berry phase in space-variant polarization-state manipulations with subwavelength gratings," Opt. Lett. **26**, 1424–1426 (2001).
[127]Z. Bomzon, G. Biener, V. Kleiner, and E. Hasman, "Space-variant Pancharatnam–Berry phase optical elements with computer-generated subwavelength gratings," Opt. Lett. **27**, 1141–1143 (2002).
[128]L. Marrucci, C. Manzo, and D. Paparo, "Optical spin-to-orbital angular momentum conversion in inhomogeneous anisotropic media," Phys. Rev. Lett. **96**, 163905 (2006).
[129]L. Marrucci, E. Karimi, S. Slussarenko, B. Piccirillo, E. Santamato, E. Nagali, and F. Sciarrino, "Spin-to-orbital optical angular momentum conversion in liquid crystal "Q-plates": Classical and quantum applications," Mol. Cryst. Liq. Cryst. **561**, 48–56 (2012).
[130]B. Piccirillo, S. Slussarenko, L. Marrucci, and E. Santamato, "The orbital angular momentum of light: Genesis and evolution of the concept and of the associated photonic technology," La Rivista Del Nuovo Cimento **36**, 501–554 (2013).
[131]I. Nape, E. Otte, A. Vallés, C. Rosales-Guzmán, F. Cardano, C. Denz, and A. Forbes, "Self-healing high-dimensional quantum key distribution using hybrid spin-orbit Bessel states," Opt. Express **26**, 26946–26960 (2018).
[132]G. Vallone, V. D'Ambrosio, A. Sponselli, S. Slussarenko, L. Marrucci, F. Sciarrino, and P. Villoresi, "Free-space quantum key distribution by rotation-invariant twisted photons," Phys. Rev. Lett. **113**, 060503 (2014).
[133]F. Hufnagel, A. Sit, F. Bouchard, Y. Zhang, D. England, K. Heshami, B. J. Sussman, and E. Karimi, "Investigation of underwater quantum channels in a 30 meter flume tank using structured photons," New J. Phys. **22**, 093074 (2020).
[134]V. D'ambrosio, E. Nagali, S. P. Walborn, L. Aolita, S. Slussarenko, L. Marrucci, and F. Sciarrino, "Complete experimental toolbox for alignment-free quantum communication," Nat. Commun. **3**, 961 (2012).
[135]Q.-K. Wang, F.-X. Wang, J. Liu, W. Chen, Z.-F. Han, A. Forbes, and J. Wang, "High-dimensional quantum cryptography with hybrid orbital-angular-momentum states through 25 km of ring-core fiber: A proof-of-concept demonstration," Phys. Rev. Appl. **15**, 064034 (2021).
[136]A. Sit, R. Fickler, F. Alsaiari, F. Bouchard, H. Larocque, P. Gregg, L. Yan, R. W. Boyd, S. Ramachandran, and E. Karimi, "Quantum cryptography with structured photons through a vortex fiber," Opt. Lett. **43**, 4108–4111 (2018).
[137]E. Nagali, V. D'Ambrosio, F. Sciarrino, and A. Cabello, "Experimental observation of impossible-to-beat quantum advantage on a hybrid photonic system," Phys. Rev. Lett. **108**, 090501 (2012).
[138]F. Cardano, M. Maffei, F. Massa, B. Piccirillo, C. De Lisio, G. De Filippis, V. Cataudella, E. Santamato, and L. Marrucci, "Statistical moments of quantum-walk dynamics reveal topological quantum transitions," Nat. Commun. **7**, 011439 (2016).
[139]B. Sephton, A. Dudley, G. Ruffato, F. Romanato, L. Marrucci, M. Padgett, S. Goyal, F. Roux, T. Konrad, and A. Forbes, "A versatile quantum walk resonator with bright classical light," PLoS One **14**, e0214891 (2019).
[140]V. D'ambrosio, N. Spagnolo, L. Del Re, S. Slussarenko, Y. Li, L. C. Kwek, L. Marrucci, S. P. Walborn, L. Aolita, and F. Sciarrino, "Photonic polarization gears for ultra-sensitive angular measurements," Nat. Commun. **4**, 2432 (2013).
[141]V. D'Ambrosio, G. Carvacho, F. Graffitti, C. Vitelli, B. Piccirillo, L. Marrucci, and F. Sciarrino, "Entangled vector vortex beams," Phys. Rev. A **94**, 030304 (2016).
[142]E. Karimi, J. Leach, S. Slussarenko, B. Piccirillo, L. Marrucci, L. Chen, W. She, S. Franke-Arnold, M. J. Padgett, and E. Santamato, "Spin-orbit hybrid entanglement of photons and quantum contextuality," Phys. Rev. A **82**, 022115 (2010).
[143]J. Liu, I. Nape, Q. Wang, A. Vallés, J. Wang, and A. Forbes, "Multidimensional entanglement transport through single-mode fiber," Sci. Adv. **6**, eaay0837 (2020).
[144]F. Graffitti, V. D'Ambrosio, M. Proietti, J. Ho, B. Piccirillo, C. De Lisio, L. Marrucci, and A. Fedrizzi, "Hyperentanglement in structured quantum light," Phys. Rev. Res. **2**, 043350 (2020).
[145]X.-L. Wang, Y.-H. Luo, H.-L. Huang, M.-C. Chen, Z.-E. Su, C. Liu, C. Chen, W. Li, Y.-Q. Fang, X. Jiang *et al.*, "18-qubit entanglement with six photons' three degrees of freedom," Phys. Rev. Lett. **120**, 260502 (2018).
[146]H.-T. Chen, A. J. Taylor, and N. Yu, "A review of metasurfaces: Physics and applications," Rep. Prog. Phys. **79**, 076401 (2016).
[147]K. Wang, M. Chekhova, and Y. Kivshar, "Metasurfaces," Phys. Today **75**(8), 38 (2022).
[148]S. Kruk, B. Hopkins, I. I. Kravchenko, A. Miroshnichenko, D. N. Neshev, and Y. S. Kivshar, "Invited article: Broadband highly efficient dielectric metadevices for polarization control," Apl Photonics **1**, 030801 (2016).
[149]G. Li, M. Kang, S. Chen, S. Zhang, E. Y.-B. Pun, K. W. Cheah, and J. Li, "Spin-enabled plasmonic metasurfaces for manipulating orbital angular momentum of light," Nano Lett. **13**, 4148–4151 (2013).
[150]R. C. Devlin, A. Ambrosio, D. Wintz, S. L. Oscurato, A. Y. Zhu, M. Khorasaninejad, J. Oh, P. Maddalena, and F. Capasso, "Spin-to-orbital angular momentum conversion in dielectric metasurfaces," Opt. Express **25**, 377–393 (2017).
[151]F. Bouchard, I. De Leon, S. A. Schulz, J. Upham, E. Karimi, and R. W. Boyd, "Optical spin-to-orbital angular momentum conversion in ultra-thin metasurfaces with arbitrary topological charges," Appl. Phys. Lett. **105**, 101905 (2014).
[152]R. C. Devlin, A. Ambrosio, N. A. Rubin, J. P. B. Mueller, and F. Capasso, "Arbitrary spin-to–orbital angular momentum conversion of light," Science **358**, 896–901 (2017).
[153]S. Wang, F. Li, J. Deng, X. Ye, Z.-L. Deng, Y. Cao, B.-O. Guan, G. Li, and X. Li, "Diatomic metasurface based broadband J-plate for arbitrary spin-to-orbital conversion," J. Phys. D: Appl. Phys. **52**, 324002 (2019).
[154]B. Sephton, Y.-W. Huang, A. Ambrosio, C.-W. Qiu, A. Vallés, T. Omatsu, F. Capasso, and A. Forbes, "Purity and efficiency of hybrid orbital angular momentum-generating metasurfaces," J. Nanophotonics **14**, 016005 (2020).
[155]J. P. Balthasar Mueller, N. A. Rubin, R. C. Devlin, B. Groever, and F. Capasso, "Metasurface polarization optics: Independent phase control of arbitrary orthogonal states of polarization," Phys. Rev. Lett. **118**, 113901 (2017).
[156]H. Ren, G. Briere, X. Fang, P. Ni, R. Sawant, S. Héron, S. Chenot, S. Vézian, B. Damilano, V. Brändli *et al.*, "Metasurface orbital angular momentum holography," Nat. Commun. **10**, 2986 (2019).
[157]H. Ren, X. Fang, J. Jang, J. Bürger, J. Rho, and S. A. Maier, "Complex-amplitude metasurface-based orbital angular momentum holography in momentum space," Nat. Nanotechnol. **15**, 948–955 (2020).
[158]C. Chen, S. Gao, X. Xiao, X. Ye, S. Wu, W. Song, H. Li, S. Zhu, and T. Li, "Highly efficient metasurface quarter-wave plate with wave front engineering," Adv. Photonics Res. **2**, 2000154 (2021).
[159]A. H. Dorrah, N. A. Rubin, M. Tamagnone, A. Zaidi, and F. Capasso, "Structuring total angular momentum of light along the propagation direction with polarization-controlled meta-optics," Nat. Commun. **12**, 6249 (2021).
[160]H. Ahmed, H. Kim, Y. Zhang, Y. Intaravanne, J. Jang, J. Rho, S. Chen, and X. Chen, "Optical metasurfaces for generating and manipulating optical vortex beams," Nanophotonics **11**, 941–956 (2022).
[161]J. Liu, M. Shi, Z. Chen, S. Wang, Z. Wang, S. Zhu *et al.*, "Quantum photonics based on metasurfaces," Opto-Electron. Adv. **4**(09), 200092 (2021).
[162]O. Bryngdahl, "Geometrical transformations in optics," J. Opt. Soc. Am. **64**, 1092–1099 (1974).
[163]G. C. G. Berkhout, M. P. J. Lavery, J. Courtial, M. W. Beijersbergen, and M. J. Padgett, "Efficient sorting of orbital angular momentum states of light," Phys. Rev. Lett. **105**, 153601 (2010).
[164]R. Fickler, R. Lapkiewicz, M. Huber, M. P. Lavery, M. J. Padgett, and A. Zeilinger, "Interface between path and orbital angular momentum entanglement for high-dimensional photonic quantum information," Nat. Commun. **5**, 4502 (2014).

11 June 2026 13:34:37

© Author(s) 2023

[165]A. D'Errico, F. Cardano, M. Maffei, A. Dauphin, R. Barboza, C. Esposito, B. Piccirillo, M. Lewenstein, P. Massignan, and L. Marrucci, "Two-dimensional topological quantum walks in the momentum space of structured light," Optica **7**, 108–114 (2020).
[166]R. Barboza, A. Babazadeh, L. Marrucci, F. Cardano, C. de Lisio, and V. D'Ambrosio, "Ultra-sensitive measurement of transverse displacements with linear photonic gears," Nat. Commun. **13**, 1080 (2022).
[167]D. Fu, Y. Zhou, R. Qi, S. Oliver, Y. Wang, S. M. H. Rafsanjani, J. Zhao, M. Mirhosseini, Z. Shi, P. Zhang *et al.*, "Realization of a scalable Laguerre–Gaussian mode sorter based on a robust radial mode sorter," Opt. Express **26**, 33057–33065 (2018).
[168]Y. Zhou, J. Zhao, Z. Shi, S. M. Hashemi Rafsanjani, M. Mirhosseini, Z. Zhu, A. E. Willner, and R. W. Boyd, "Hermite–Gaussian mode sorter," Opt. Lett. **43**, 5263–5266 (2018).
[169]N. K. Fontaine, R. Ryf, H. Chen, D. T. Neilson, K. Kim, and J. Carpenter, "Laguerre-Gaussian mode sorter," Nat. Commun. **10**, 1865 (2019).
[170]H. Defienne and D. Faccio, "Arbitrary spatial mode sorting in a multimode fiber," Phys. Rev. A **101**, 063830 (2020).
[171]W. T. Chen, A. Y. Zhu, J. Sisler, Z. Bharwani, and F. Capasso, "A broadband achromatic polarization-insensitive metalens consisting of anisotropic nanostructures," Nat. Commun. **10**, 355 (2019).
[172]W. T. Chen, A. Y. Zhu, J. Sisler, Y.-W. Huang, K. M. A. Yousef, E. Lee, C.-W. Qiu, and F. Capasso, "Broadband achromatic metasurface-refractive optics," Nano Lett. **18**, 7801–7808 (2018).
[173]E. Arbabi, A. Arbabi, S. M. Kamali, Y. Horie, and A. Faraon, "Multiwavelength polarization-insensitive lenses based on dielectric metasurfaces with meta-molecules," Optica **3**, 628–633 (2016).
[174]A. Krasnok, M. Tymchenko, and A. Alù, "Nonlinear metasurfaces: A paradigm shift in nonlinear optics," Mater. Today **21**, 8–21 (2018).
[175]L. Wang, S. Kruk, K. Koshelev, I. Kravchenko, B. Luther-Davies, and Y. Kivshar, "Nonlinear wavefront control with all-dielectric metasurfaces," Nano Lett. **18**, 3978–3984 (2018).
[176]G. Li, S. Zhang, and T. Zentgraf, "Nonlinear photonic metasurfaces," Nat. Rev. Mater. **2**, 17010 (2017).
[177]J. F. Clauser, M. A. Horne, A. Shimony, and R. A. Holt, "Proposed experiment to test local hidden-variable theories," Phys. Rev. Lett. **23**, 880 (1969).
[178]J. Leach, B. Jack, J. Romero, M. Ritsch-Marte, R. W. Boyd, A. K. Jha, S. M. Barnett, S. Franke-Arnold, and M. J. Padgett, "Violation of a Bell inequality in two-dimensional orbital angular momentum state-spaces," Opt. Express **17**, 8287–8293 (2009).
[179]B. S. Cirel'son, "Quantum generalizations of Bell's inequality," Lett. Math. Phys. **4**, 93–100 (1980).
[180]D. Collins, N. Gisin, N. Linden, S. Massar, and S. Popescu, "Bell inequalities for arbitrarily high-dimensional systems," Phys. Rev. Lett. **88**, 040404 (2002).
[181]A. Vaziri, G. Weihs, and A. Zeilinger, "Experimental two-photon, three-dimensional entanglement for quantum communication," Phys. Rev. Lett. **89**, 240401 (2002).
[182]S. Gröblacher, T. Jennewein, A. Vaziri, G. Weihs, and A. Zeilinger, "Experimental quantum cryptography with qutrits," New J. Phys. **8**, 75 (2006).
[183]J. B. Altepeter, E. R. Jeffrey, and P. G. Kwiat, "Photonic state tomography," Adv. At., Mol., Opt. Phys. **52**, 105–159 (2005).
[184]D. Giovannini, J. Romero, J. Leach, A. Dudley, A. Forbes, and M. J. Padgett, "Characterization of high-dimensional entangled systems via mutually unbiased measurements," Phys. Rev. Lett. **110**, 143601 (2013).
[185]Z. Hou, J.-F. Tang, C. Ferrie, G.-Y. Xiang, C.-F. Li, and G.-C. Guo, "Experimental realization of self-guided quantum process tomography," Phys. Rev. A **101**, 022317 (2020).
[186]M. Rambach, M. Qaryan, M. Kewming, C. Ferrie, A. G. White, and J. Romero, "Robust and efficient high-dimensional quantum state tomography," Phys. Rev. Lett. **126**, 100402 (2021).
[187]J. B. Altepeter, E. R. Jeffrey, and P. G. Kwiat, "Phase-compensated ultra-bright source of entangled photons," Opt. Express **13**, 8951–8959 (2005).
[188]M. D. De Burgh, N. K. Langford, A. C. Doherty, and A. Gilchrist, "Choice of measurement sets in qubit tomography," Phys. Rev. A **78**, 052122 (2008).
[189]Z. Hradil, "Quantum-state estimation," Phys. Rev. A **55**, R1561 (1997).
[190]K. Banaszek, G. D'ariano, M. Paris, and M. Sacchi, "Maximum-likelihood estimation of the density matrix," Phys. Rev. A **61**, 010304 (1999).
[191]D. F. V. James, P. G. Kwiat, W. J. Munro, and A. G. White, "Measurement of qubits," Phys. Rev. A **64**, 052312 (2001).
[192]K. R. W. Jones, "Principles of quantum inference," Ann. Phys. **207**, 140–170 (1991).
[193]R. Blume-Kohout, "Optimal, reliable estimation of quantum states," New J. Phys. **12**, 043034 (2010).
[194]C. Granade, J. Combes, and D. G. Cory, "Practical Bayesian tomography," New J. Phys. **18**, 033024 (2016).
[195]B. Jack, J. Leach, H. Ritsch, S. M. Barnett, M. J. Padgett, and S. Franke-Arnold, "Precise quantum tomography of photon pairs with entangled orbital angular momentum," New J. Phys. **11**, 103024 (2009).
[196]W. K. Wootters and B. D. Fields, "Optimal state-determination by mutually unbiased measurements," Ann. Phys. **191**, 363–381 (1989).
[197]T. Durt, B.-G. Englert, I. Bengtsson, and K. Życzkowski, "On mutually unbiased bases," Int. J. Quantum Inf. **08**, 535–640 (2010).
[198]A. K. Ekert, "Quantum cryptography and Bell's theorem," in *Quantum Measurements in Optics* (Springer, 1992), pp. 413–418.
[199]P. W. Shor, "Polynomial-time algorithms for prime factorization and discrete logarithms on a quantum computer," SIAM Rev. **41**, 303–332 (1999).
[200]W. K. Wootters and W. H. Zurek, "The no-cloning theorem," Phys. Today **62**(2), 76–77 (2009).
[201]E. Otte, I. Nape, C. Rosales-Guzmán, C. Denz, A. Forbes, and B. Ndagano, "High-dimensional cryptography with spatial modes of light: Tutorial," J. Opt. Soc. Am. B **37**, A309–A323 (2020).
[202]N. J. Cerf, C. Adami, and P. G. Kwiat, "Optical simulation of quantum logic," Phys. Rev. A **57**, R1477 (1998).
[203]M. A. Cox, N. Mphuthi, I. Nape, N. Mashaba, L. Cheng, and A. Forbes, "Structured light in turbulence," IEEE J. Sel. Top. Quantum Electron. **27**, 1–21 (2020).
[204]J. Wang, Q. Wang, J. Liu, and D. Lyu, "Quantum orbital angular momentum in fibers: A review," AVS Quantum Sci. **4**, 031701 (2022).
[205]R. Fickler, F. Bouchard, E. Giese, V. Grillo, G. Leuchs, and E. Karimi, "Full-field mode sorter using two optimized phase transformations for high-dimensional quantum cryptography," J. Opt. **22**, 024001 (2020).
[206]O. Lib, K. Sulimany, and Y. Bromberg, "Processing entangled photons in high dimensions with a programmable light converter," Phys. Rev. Appl. **18**, 014063 (2022).
[207]C. H. Bennett, G. Brassard, C. Crépeau, R. Jozsa, A. Peres, and W. K. Wootters, "Teleporting an unknown quantum state via dual classical and einstein-podolsky-rosen channels," Phys. Rev. Lett. **70**, 1895 (1993).
[208]M. A. Nielsen, E. Knill, and R. Laflamme, "Complete quantum teleportation using nuclear magnetic resonance," Nature **396**, 52–55 (1998).
[209]J. F. Sherson, H. Krauter, R. K. Olsson, B. Julsgaard, K. Hammerer, I. Cirac, and E. S. Polzik, "Quantum teleportation between light and matter," Nature **443**, 557–560 (2006).
[210]H. Krauter, D. Salart, C. A. Muschik, J. M. Petersen, H. Shen, T. Fernholz, and E. S. Polzik, "Deterministic quantum teleportation between distant atomic objects," Nat. Phys. **9**, 400–404 (2013).
[211]Y.-A. Chen, S. Chen, Z.-S. Yuan, B. Zhao, C.-S. Chuu, J. Schmiedmayer, and J.-W. Pan, "Memory-built-in quantum teleportation with photonic and atomic qubits," Nat. Phys. **4**, 103–107 (2008).
[212]X.-H. Bao, X.-F. Xu, C.-M. Li, Z.-S. Yuan, C.-Y. Lu, and J.-W. Pan, "Quantum teleportation between remote atomic-ensemble quantum memories," Proc. Natl. Acad. Sci. U. S. A. **109**, 20347–20351 (2012).
[213]W. B. Gao, P. Fallahi, E. Togan, A. Delteil, Y. S. Chin, J. Miguel-Sanchez, and A. Imamoğlu, "Quantum teleportation from a propagating photon to a solid-state spin qubit," Nat. Commun. **4**, 2744 (2013).
[214]F. Bussières, C. Clausen, A. Tiranov, B. Korzh, V. B. Verma, S. W. Nam, F. Marsili, A. Ferrier, P. Goldner, H. Herrmann *et al.*, "Quantum teleportation from a telecom-wavelength photon to a solid-state quantum memory," Nat. Photonics **8**, 775–778 (2014).
[215]L. Steffen, Y. Salathe, M. Oppliger, P. Kurpiers, M. Baur, C. Lang, C. Eichler, G. Puebla-Hellmann, A. Fedorov, and A. Wallraff, "Deterministic quantum

11 June 2026 13:34:37

© Author(s) 2023

teleportation with feed-forward in a solid state system," Nature **500**, 319–322 (2013).
[216]W. Pfaff, B. J. Hensen, H. Bernien, S. B. van Dam, M. S. Blok, T. H. Taminiau, M. J. Tiggelman, R. N. Schouten, M. Markham, D. J. Twitchen *et al.*, "Unconditional quantum teleportation between distant solid-state quantum bits," Science **345**, 532–535 (2014).
[217]M. D. Barrett, J. Chiaverini, T. Schaetz, J. Britton, W. M. Itano, J. D. Jost, E. Knill, C. Langer, D. Leibfried, R. Ozeri *et al.*, "Deterministic quantum teleportation of atomic qubits," Nature **429**, 737–739 (2004).
[218]M. Riebe, H. Häffner, C. F. Roos, W. Hänsel, J. Benhelm, G. P. T. Lancaster, T. W. Körber, C. Becher, F. Schmidt-Kaler, D. F. V. James *et al.*, "Deterministic quantum teleportation with atoms," Nature **429**, 734–737 (2004).
[219]M. Riebe, M. Chwalla, J. Benhelm, H. Häffner, W. Hänsel, C. F. Roos, and R. Blatt, "Quantum teleportation with atoms: Quantum process tomography," New J. Phys. **9**, 211 (2007).
[220]S. Olmschenk, D. N. Matsukevich, P. Maunz, D. Hayes, L.-M. Duan, and C. Monroe, "Quantum teleportation between distant matter qubits," Science **323**, 486–489 (2009).
[221]C. Nölleke, A. Neuzner, A. Reiserer, C. Hahn, G. Rempe, and S. Ritter, "Efficient teleportation between remote single-atom quantum memories," Phys. Rev. Lett. **110**, 140403 (2013).
[222]I. Marcikic, H. De Riedmatten, W. Tittel, H. Zbinden, and N. Gisin, "Long-distance teleportation of qubits at telecommunication wavelengths," Nature **421**, 509–513 (2003).
[223]H. De Riedmatten, I. Marcikic, W. Tittel, H. Zbinden, D. Collins, and N. Gisin, "Long distance quantum teleportation in a quantum relay configuration," Phys. Rev. Lett. **92**, 047904 (2004).
[224]O. Landry, J. A. W. van Houwelingen, A. Beveratos, H. Zbinden, and N. Gisin, "Quantum teleportation over the Swisscom telecommunication network," J. Opt. Soc. Am. B **24**, 398–403 (2007).
[225]R. Ursin, T. Jennewein, M. Aspelmeyer, R. Kaltenbaek, M. Lindenthal, P. Walther, and A. Zeilinger, "Quantum teleportation across the Danube," Nature **430**, 849 (2004).
[226]D. Boschi, S. Branca, F. De Martini, L. Hardy, and S. Popescu, "Experimental realization of teleporting an unknown pure quantum state via dual classical and Einstein-Podolsky-Rosen channels," Phys. Rev. Lett. **80**, 1121 (1998).
[227]X.-M. Jin, J.-G. Ren, B. Yang, Z.-H. Yi, F. Zhou, X.-F. Xu, S.-K. Wang, D. Yang, Y.-F. Hu, S. Jiang *et al.*, "Experimental free-space quantum teleportation," Nat. Photonics **4**, 376–381 (2010).
[228]Y.-H. Kim, S. P. Kulik, and Y. Shih, "Quantum teleportation of a polarization state with a complete bell state measurement," Phys. Rev. Lett. **86**, 1370 (2001).
[229]J. Yin, J.-G. Ren, H. Lu, Y. Cao, H.-L. Yong, Y.-P. Wu, C. Liu, S.-K. Liao, F. Zhou, Y. Jiang *et al.*, "Quantum teleportation and entanglement distribution over 100-kilometre free-space channels," Nature **488**, 185–188 (2012).
[230]X.-S. Ma, T. Herbst, T. Scheidl, D. Wang, S. Kropatschek, W. Naylor, B. Wittmann, A. Mech, J. Kofler, E. Anisimova *et al.*, "Quantum teleportation over 143 kilometres using active feed-forward," Nature **489**, 269–273 (2012).
[231]M. A. Nielsen and I. Chuang, *Quantum Computation and Quantum Information* (American Association of Physics Teachers, 2002).
[232]H. Weinfurter, "Experimental Bell-state analysis," Europhys. Lett. **25**, 559 (1994).
[233]S. L. Braunstein and A. Mann, "Measurement of the Bell operator and quantum teleportation," Phys. Rev. A **51**, R1727 (1995).
[234]J. Calsamiglia and N. Lütkenhaus, "Maximum efficiency of a linear-optical bell-state analyzer," Appl. Phys. B **72**, 67–71 (2001).
[235]M. M. Wilde, *Quantum Information Theory* (Cambridge University Press, 2013).
[236]C. Weedbrook, S. Pirandola, R. García-Patrón, N. J. Cerf, T. C. Ralph, J. H. Shapiro, and S. Lloyd, "Gaussian quantum information," Rev. Mod. Phys. **84**, 621 (2012).
[237]S. L. Braunstein and P. Van Loock, "Quantum information with continuous variables," Rev. Mod. Phys. **77**, 513 (2005).
[238]N. Gisin, G. Ribordy, W. Tittel, and H. Zbinden, "Quantum cryptography," Rev. Mod. Phys. **74**, 145–195 (2002).
[239]H.-J. Briegel, W. Dür, J. I. Cirac, and P. Zoller, "Quantum repeaters: The role of imperfect local operations in quantum communication," Phys. Rev. Lett. **81**, 5932 (1998).
[240]R. Raussendorf and H. J. Briegel, "A one-way quantum computer," Phys. Rev. Lett. **86**, 5188 (2001).
[241]D. Gottesman and I. L. Chuang, "Demonstrating the viability of universal quantum computation using teleportation and single-qubit operations," Nature **402**, 390–393 (1999).
[242]H. J. Kimble, "The quantum internet," Nature **453**, 1023–1030 (2008).
[243]X.-X. Xia, Q.-C. Sun, Q. Zhang, and J.-W. Pan, "Long distance quantum teleportation," Quantum Sci. Technol. **3**, 014012 (2017).
[244]H. Takesue, S. D. Dyer, M. J. Stevens, V. Verma, R. P. Mirin, and S. W. Nam, "Quantum teleportation over 100 km of fiber using highly efficient superconducting nanowire single-photon detectors," Optica **2**, 832–835 (2015).
[245]R. Valivarthi, S. I. Davis, C. Peña, S. Xie, N. Lauk, L. Narváez, J. P. Allmaras, A. D. Beyer, Y. Gim, M. Hussein *et al.*, "Teleportation systems toward a quantum internet," PRX Quantum **1**, 020317 (2020).
[246]T. Herbst, T. Scheidl, M. Fink, J. Handsteiner, B. Wittmann, R. Ursin, and A. Zeilinger, "Teleportation of entanglement over 143 km," Proc. Natl. Acad. Sci. U. S. A. **112**, 14202–14205 (2015).
[247]J.-G. Ren, P. Xu, H.-L. Yong, L. Zhang, S.-K. Liao, J. Yin, W.-Y. Liu, W.-Q. Cai, M. Yang, L. Li *et al.*, "Ground-to-satellite quantum teleportation," Nature **549**, 70–73 (2017).
[248]C. Simon, "Towards a global quantum network," Nat. Photonics **11**, 678–680 (2017).
[249]S. Wehner, D. Elkouss, and R. Hanson, "Quantum internet: A vision for the road ahead," Science **362**, eaam9288 (2018).
[250]R. F. Werner, "All teleportation and dense coding schemes," J. Phys. A: Math. Gen. **34**, 7081 (2001).
[251]W. Son, J. Lee, M. Kim, and Y.-J. Park, "Conclusive teleportation of a d-dimensional unknown state," Phys. Rev. A **64**, 064304 (2001).
[252]J. Calsamiglia, "Generalized measurements by linear elements," Phys. Rev. A **65**, 030301 (2002).
[253]S. K. Goyal, P. E. Boukama-Dzoussi, S. Ghosh, F. S. Roux, and T. Konrad, "Qudit-teleportation for photons with linear optics," Sci. Rep. **4**, 4543 (2014).
[254]S. N. Molotkov, "Quantum teleportation of a single-photon wave packet," Phys. Lett. A **245**, 339–344 (1998).
[255]T. S. Humble, "Spectral and spread-spectral teleportation," Phys. Rev. A **81**, 062339 (2010).
[256]X. Qiu, H. Guo, and L. Chen, "Quantum teleportation of high-dimensional spatial modes: Towards an image teleporter," arXiv:2112.03764 (2021).
[257]S. M. Barnett, "On single-photon and classical interference," Phys. Scr. **97**, 114004 (2022).
[258]T. B. Pittman, Y. H. Shih, D. V. Strekalov, and A. V. Sergienko, "Optical imaging by means of two-photon quantum entanglement," Phys. Rev. A **52**, R3429 (1995).
[259]Y. Shih, "The physics of ghost imaging," Classical, Semi-Classical Quantum Noise **169**, 222 (2012); arXiv:0805.1166v5.
[260]A. F. Abouraddy, B. E. Saleh, A. V. Sergienko, and M. C. Teich, "Role of entanglement in two-photon imaging," Phys. Rev. Lett. **87**, 123602 (2001); arXiv:0108124 [quant-ph].
[261]A. F. Abouraddy, P. R. Stone, A. V. Sergienko, B. E. Saleh, and M. C. Teich, "Entangled-photon imaging of a pure phase object," Phys. Rev. Lett. **93**, 213903 (2004).
[262]S. S. Welsh, M. P. Edgar, R. Bowman, B. Sun, and M. J. Padgett, "Near video-rate linear Stokes imaging with single-pixel detectors," J. Opt. **17**, 025705 (2015).
[263]J. H. Shapiro, "Computational ghost imaging," Phys. Rev. A **78**, 061802 (2008) arXiv:0807.2614.
[264]G. M. Gibson, S. D. Johnson, and M. J. Padgett, "Single-pixel imaging 12 years on: A review," Opt. Express **28**, 28190–28208 (2020).
[265]F. Ferri, D. Magatti, L. A. Lugiato, and A. Gatti, "Differential ghost imaging," Phys. Rev. Lett. **104**, 253603 (2010).
[266]W. K. Pratt, J. Kane, and H. C. Andrews, "Hadamard transform image coding," Proc. IEEE **57**, 58–68 (1969).

11 June 2026 13:34:37

© Author(s) 2023

[267]M. F. Duarte, M. A. Davenport, D. Takhar, J. N. Laska, T. Sun, K. F. Kelly, and R. G. Baraniuk, "Single-pixel imaging via compressive sampling," IEEE Signal Process. Mag. **25**, 83–91 (2008).
[268]J. L. Walsh, "A closed set of normal orthogonal functions," Am. J. Math. **45**, 5–24 (1923).
[269]N. J. A. Sloane and M. Harwit, "Masks for Hadamard transform optics, and weighing designs," Appl. Opt. **15**, 107–114 (1976).
[270]Y. Y. Schechner, S. K. Nayar, and P. N. Belhumeur, "A theory of multiplexed illumination," in *ICCV* (2003), Vol. 3, pp. 808–815.
[271]Y. Y. Schechner, S. K. Nayar, and P. N. Belhumeur, "Multiplexing for optimal lighting," IEEE Trans. Pattern Anal. Mach. Intell. **29**, 1339–1354 (2007).
[272]C. Moodley, B. Sephton, V. R. Fajardo, and A. Forbes, "Deep learning early stopping for non - degenerate ghost imaging," Sci. Rep. **11**, 8561 (2021).
[273]C. Moodley, A. Ruget, J. Leach, and A. Forbes, "Time-efficient object recognition in quantum ghost imaging," Adv. Quantum Technol. **6**, 2200109 (2022).
[274]P.-A. Moreau, E. Toninelli, P. A. Morris, R. S. Aspden, T. Gregory, G. Spalding, R. W. Boyd, and M. J. Padgett, "Resolution limits of quantum ghost imaging," Opt. Express **26**, 7528–7536 (2018).
[275].B. Sephton, I. Nape, C. Moodley, J. Francis, and A. Forbes, "Revealing the embedded phase in single pixel quantum ghost imaging," Optica **10**, 286 (2023); arXiv:2206.03180.
[276]P A. Morris, R. S. Aspden, J. E. Bell, R. W. Boyd, and M. J. Padgett, "Imaging with a small number of photons," Nat. Commun. **6**, 5913 (2015).
[277]P.-A. Moreau, E. Toninelli, T. Gregory, and M. J. Padgett, "Imaging with quantum states of light," Nat. Rev. Phys. **1**, 367–380 (2019).
[278]R. S. Aspden, D. S. Tasca, R. W. Boyd, and M. J. Padgett, "EPR-based ghost imaging using a single-photon-sensitive camera," New J. Phys. **15**, 073032 (2013).
[279]H. Defienne, J. Zhao, E. Charbon, and D. Faccio, "Full-field quantum imaging with a single-photon avalanche diode camera," Phys. Rev. A **103**, 042608 (2021).
[280]H. Defienne, P. Cameron, B. Ndagano, A. Lyons, M. Reichert, J. Zhao, A. R. Harvey, E. Charbon, J. W. Fleischer, and D. Faccio, "Pixel super-resolution with spatially entangled photons," Nat. Commun. **13**, 3566 (2022).
[281]P. A. Moreau, E. Toninelli, T. Gregory, R. S. Aspden, P. A. Morris, and M. J. Padgett, "Imaging bell-type nonlocal behavior," Sci. Adv. **5**, eaaw2563 (2019).
[282]A. Nomerotski, D. Katramatos, P. Stankus, P. Svihra, G. Cui, S. Gera, M. Flament, and E. Figueroa, "Spatial and temporal characterization of polarization entanglement," Int. J. Quant. Inf. **18**, 1941027 (2020).
[283]F. Bouchard, A. Sit, Y. Zhang, R. Fickler, F. M. Miatto, Y. Yao, F. Sciarrino, and E. Karimi, "Two-photon interference: The Hong–Ou–Mandel effect," Rep. Prog. Phys. **84**, 012402 (2020).
[284]B. Ndagano, H. Defienne, A. Lyons, I. Starshynov, F. Villa, S. Tisa, and D. Faccio, "Imaging and certifying high-dimensional entanglement with a single-photon avalanche diode camera," npj Quantum Inf. **6**, 94 (2020).
[285]Y. Li, S. Y. Huang, M. Wang, C. Tu, X. L. Wang, Y. Li, H. T. Wang *et al.*, "Two-measurement tomography of high-dimensional orbital angular momentum entanglement," Phys. Rev. Lett. **130**, 050805 (2023).
[286]H. Defienne, B. Ndagano, A. Lyons, and D. Faccio, "Polarization entanglement-enabled quantum holography," Nat. Phys. **17**, 591–597 (2021).
[287]A. C. Elitzur and L. Vaidman, "Quantum mechanical interaction-free measurements," Found. Phys. **23**, 987–997 (1993).
[288]L. Vaidman, "The meaning of the interaction-free measurements," Found. Phys. **33**, 491–510 (2003).
[289]A. G. White, J. R. Mitchell, O. Nairz, and P. G. Kwiat, "'Interaction-free' imaging," Phys. Rev. A **58**, 605 (1998).
[290]Y. Zhang, A. Sit, F. Bouchard, H. Larocque, F. Grenapin, E. Cohen, A. C. Elitzur, J. L. Harden, R. W. Boyd, and E. Karimi, "Interaction-free ghost-imaging of structured objects," Opt. Express **27**, 2212–2224 (2019).
[291]B. Ndagano, H. Defienne, D. Branford, Y. D. Shah, A. Lyons, N. Westerberg, E. M. Gauger, and D. Faccio, "Quantum microscopy based on Hong–Ou–Mandel interference," Nat. Photonics **16**, 384 (2022).
[292]G. B. Lemos, V. Borish, G. D. Cole, S. Ramelow, R. Lapkiewicz, and A. Zeilinger, "Quantum imaging with undetected photons," Nature **512**, 409–412 (2014).
[293]M. Lahiri, R. Lapkiewicz, G. B. Lemos, and A. Zeilinger, "Theory of quantum imaging with undetected photons," Phys. Rev. A **92**, 013832 (2015).
[294]J. Fuenzalida, A. Hochrainer, G. B. Lemos, E. A. Ortega, R. Lapkiewicz, M. Lahiri, and A. Zeilinger, "Resolution of quantum imaging with undetected photons," Quantum **6**, 646 (2022).
[295]G. Barreto Lemos, M. Lahiri, S. Ramelow, R. Lapkiewicz, and W. N. Plick, "Quantum imaging and metrology with undetected photons: Tutorial," J. Opt. Soc. Am. B **39**, 2200–2228 (2022).

11 June 2026 13:34:37

© Author(s) 2023